

A Solar-Powered, Milligram Prototype Robot from a Three-Chip Process

by

Seth Edward-Austin Hollar

B.S. (Massachusetts Institute of Technology) 1996

M.S. (University of California, Berkeley) 2000

A dissertation submitted in partial satisfaction of the

requirements for the degree of

Doctor of Philosophy

in

Engineering - Mechanical Engineering

in the

GRADUATE DIVISION

of the

UNIVERSITY OF CALIFORNIA, BERKELEY

Committee in charge:

Professor Kristofer S. J. Pister, Co-chair

Professor Albert P. Pisano, Co-chair

Professor Roger T. Howe

Professor Richard M. White

Spring 2003

The dissertation of Seth Edward-Austin Hollar is approved:

Professor Kristofer S. J. Pister, Co-chair Date

Professor Albert P. Pisano, Co-chair Date

Professor Roger T. Howe Date

Professor Richard M. White Date

University of California, Berkeley

Spring 2003

A Solar-Powered, Milligram Prototype Robot from a Three-Chip Process

Copyright 2003

by

Seth Edward-Austin Hollar

Abstract

A Solar-Powered, Milligram Prototype Robot from a Three-Chip Process

by

Seth Edward-Austin Hollar

Doctor of Philosophy in Mechanical Engineering

University of California, Berkeley

Professor Kristofer S. J. Pister, Co-chair

Professor Albert P. Pisano, Co-chair

Commercial CMOS electronics and two in-house processes have been combined to establish a framework for making hybridized, milligram mobile robots. To demonstrate the capabilities of this framework, an 8.6 mm long, 10 mg, solar-powered prototype robot has been built. Dragging its tail end, the robot has demonstrated autonomous movement under its own weight and power, shuffling to the side a few millimeters and lifting its front end as much as 300 μm off the surface.

A simple 5-mask process, the Iolanthe process, was devised for the robot's frame, inchworm motors, and legs. The Iolanthe process combined bulk SOI micromachining with polysilicon surface micromachining to achieve high-force in-plane electrostatic motors with compliant out-of-plane structures. The enabling step of the process was planarization of the SOI device layer using thick glass planarization technology. Out-of-plane leg motion was demonstrated using electrostatic inchworm motors with polysilicon pin hinges. In addition to the one-DOF legs for the robot, a two-DOF leg and a bidirectional inchworm motor were also fabricated and tested. Inchworm motors demonstrated 400 μm of travel at speeds up to 6.8 mm/s. The two-DOF leg demonstrated angular

deflections over 90° , and the one-DOF leg output forces up to $60 \mu\text{N}$.

In the second process, high-voltage solar cell arrays were created to drive the electrostatic actuators of the inchworm motors. In order to generate the high voltages, individual solar cells were electrically isolated with isolation trenches on the SOI device layer. Solar cell arrays as small as 0.6 mm^2 generated over 30 V. NMOS and PMOS transistors with breakdown voltages ranging from 42 V to 100 V were also integrated into the process. With these devices, a 50 V solar-powered buffer was demonstrated in an area of $3.6 \times 1.8 \text{ mm}^2$.

The third and final chip of the robot was fabricated in a commercial CMOS foundry. The chip provided the logic signals to drive the legs in an open-loop walking gait.

Professor Kristofer S. J. Pister, Co-chair Date

Professor Albert P. Pisano, Co-chair Date

Table of Contents

Chapter 1. Introduction	1
1.1 History	4
1.2 Motors.....	4
1.3 Articulated Links	9
1.4 Microcontrollers, Sensors, and Communication	10
1.5 Solar Cells	11
1.5.1 Solar Cell Fundamentals.....	12
1.5.2 Single Cells.....	13
1.5.3 Stacked Cells	14
1.6 Microbatteries.....	16
1.7 Microrobot Applications	16
1.7.1 Tracking Scenario (Surveillance).....	17
1.7.2 Human Detection in Post Earthquake Rescue Missions.....	18
1.7.3 Construction Scenario	20
Chapter 2. Fabrication and Assembly	22
2.1 Microrobot Concept.....	22
2.2 Solar Cells, Transistors, and Isolation Trenches - Icarus Process	23
2.2.1 Icarus, the Solar Cells and the High-Voltage CMOS Process	24
2.2.1.1 Ion Implantations, Gates, and Drive-In	25
2.2.1.2 Isolation and Refill	30
2.2.1.3 Phosphorus Contamination and Transistor Rings	33
2.2.2 Solar Cells, CMOS, and MEMS.....	34
2.3 Planarized SOI and Polysilicon Micromachining - Iolanthe Process.....	37
2.3.1 Thick Glass Film Technology	38
2.3.2 Structure Release	45
2.3.3 Bubbles and Pb Diffusion.....	48
2.4 Three-Chip Hybrid Assembly	50
Chapter 3. Analysis.....	53
3.1 Walking Sequence	54
3.2 Robot Motor Design Approach	55
3.3 Inchworm Motor.....	58
3.3.1 Lateral Etching of Clutch and Drive Gaps	58
3.3.2 Lateral Etching of the Inchworm Teeth.....	62
3.3.3 Bidirectional Motion in Inchworm Motors	66
3.3.3.1 Reinforced Restoring Spring in Drive Actuator.....	66
3.3.3.2 Symmetric Bidirectional Inchworm Motor	69
3.3.4 Constraining Motion of Shuttle	71
3.4 Iolanthe Design Considerations.....	72
3.5 Out-of-plane Linkages and Legs	75
3.5.1 Hinge Design	75
3.5.2 One-DOF Leg.....	78
3.5.3 Two-DOF Leg	81

3.6	Solar Cells and Transistors from the Icarus Process	83
3.6.1	High-Voltage Transistors	83
3.6.2	High-Voltage Buffer	86
3.7	Sequencer	88
Chapter 4.	Results.....	92
4.1	Sequencer Performance	92
4.2	Solar Cells, Transistors, and Buffer Performance	93
4.2.1	Transistor Performance.....	94
4.2.2	High-Voltage Buffer Performance.....	96
4.3	Legs, Robot Motion, and Test Structures	97
4.3.1	Slider Friction and Hinge Strength Tests.....	98
4.3.2	One-DOF Leg Performance	101
4.3.3	Solar Powered Robot.....	105
4.3.4	Two-DOF Leg Performance	108
4.4	Other Structures from the Iolanthe Process.....	110
4.4.1	Bidirectional Inchworm Motor.....	110
4.4.2	Torsionally Hinged Devices	111
Chapter 5.	Conclusion and Future Work.....	113
5.1	Four-Legged Robot Concept	113
5.2	Integrated Robot Process.....	116

List of Figures

Fig. 1.	Image of the Autobots from the The Transformers TV show (1984).....	1
Fig. 2.	Monsieur robot by Seiko	3
Fig. 3.	1/4 cubic inch robot from Sandia National Laboratory.	3
Fig. 4.	Mock-up of a six legged microrobot	5
Fig. 5.	A tethered walking microrobot.....	5
Fig. 6.	Diagram of a gap closing actuator (GCA).....	6
Fig. 7.	Diagram of a GCA array.....	6
Fig. 8.	Single mask SOI inchworm motor	7
Fig. 9.	Close-up view of clutch and shuttle.....	7
Fig. 10.	Diagram of an inchworm cycle.....	8
Fig. 11.	Two-DOF legs without actuation.....	10
Fig. 12.	Legs with thermal actuation.....	10
Fig. 13.	Smart dust node	12
Fig. 14.	Die photo of solar cell arrays.....	15
Fig. 15.	SEM of isolation trench.....	15
Fig. 16.	Earthquake scenario.....	18
Fig. 17.	Mars exploration scenario.....	20
Fig. 18.	Computer modeled rendering of walking robot.....	22
Fig. 19.	Doping profiles for wells of transistors	26
Fig. 20.	Doping profiles for the source/drain regions of transistors	26
Fig. 21.	Icarus process flow	27
Fig. 22.	Surface contamination of dopants.	33
Fig. 23.	P+ ring on NMOS transistor.....	34
Fig. 24.	Process flow addendum for MEMS.....	35
Fig. 25.	Atmospheric firing vs. vacuum firing.....	38
Fig. 26.	Firing profile of glass.	39
Fig. 27.	Planarized SOI / two polysilicon layers process.....	41
Fig. 28.	Belljar furnace	44
Fig. 29.	Release station	46
Fig. 30.	SolidWorks drawings of release holder.	47
Fig. 31.	Poly-Si shell from exposed bubble.....	48
Fig. 32.	Lead diffusion into LPCVD LTO.	50
Fig. 33.	Robot assembly in three steps	51
Fig. 34.	Improved concept of robot.....	53
Fig. 35.	Leg sequence for walking robot.	55
Fig. 36.	Layout of backstop, shuttle, and clutch.....	60
Fig. 37.	SEM of actual backstop, shuttle, and clutch.....	60
Fig. 38.	Layout of drive and drive backstop	61
Fig. 39.	Tooth width vs. lateral etching.....	63
Fig. 40.	SEM of gear teeth.	65
Fig. 41.	Close-up drawing of gear teeth.....	65
Fig. 42.	Diagram of inchworm motor with shuttle	67
Fig. 43.	Reversing sequence of inchworm motor	68
Fig. 44.	Bidirectional inchworm mechanism	70
Fig. 45.	The inchworm motor shuttle and pawl	72
Fig. 46.	SEM of latch structure	73
Fig. 47.	Bubble deformation of Poly-Si.....	74
Fig. 48.	Polysilicon jumper bridges Wire 2.	75
Fig. 49.	SEM images and cross sections of hinges	76
Fig. 50.	Polysilicon hinges attached to SOI device layer.....	77

Fig. 51. Interdigitated SOI device layer fingers.....	77
Fig. 52. Schematic of one-DOF leg	78
Fig. 53. Angular deflection and vertical displacement of leg tip.....	79
Fig. 54. CAD drawing of single leg and inchworm motor of the robot.....	80
Fig. 55. CAD drawing of robot frame with both legs.....	80
Fig. 56. Two-DOF leg schematic.....	81
Fig. 57. CAD drawing of two-DOF leg	82
Fig. 58. Avant! Medici simulation of potential fields across HV devices.	84
Fig. 59. Simulated breakdown curve for HV CMOS using Medici.....	85
Fig. 60. Vertical DMOS transistor	86
Fig. 61. Schematic of high-voltage buffer	87
Fig. 62. Current-starved ring oscillator.....	89
Fig. 63. Logic to generate inchworm sequence	90
Fig. 64. Three-chip working robot.....	92
Fig. 65. Die photo of sequencer	93
Fig. 66. Sixty cell solar array	94
Fig. 67. Id vs. Vd for circular PFET transistor	95
Fig. 68. Drain leakage current for zero gate voltage.....	95
Fig. 69. Die photo of solar cell buffers	96
Fig. 70. Performance of voltage translator with a 48 V power supply	97
Fig. 71. Power consumption vs. frequency.....	98
Fig. 72. SEM of the sliding test structure.	99
Fig. 73. Force measurements taken from the sliding friction test structures	100
Fig. 74. SEM close-up of poly-Si scissor hinge on SOI beams.....	100
Fig. 75. SEM hinge test structure.....	100
Fig. 76. SEM of released legs, motors, and robot frame.....	101
Fig. 77. SEM: Shuttle, recoil spring, and preset structures.....	102
Fig. 78. SEM of robot leg in preset condition.....	103
Fig. 79. Kinematic diagram of robot leg and SEM of linkage structure.....	103
Fig. 80. Robot leg being driven by external controller	103
Fig. 81. Relative force vs. clutch and drive voltages for long leg.	104
Fig. 82. Video of shuffling robot.....	106
Fig. 83. Video of robot trajectory.....	107
Fig. 84. SEM of two-DOF leg	108
Fig. 85. SEM close-up of knee joint	108
Fig. 86. Area swept out by two-DOF leg.....	109
Fig. 87. Bidirectional motor.....	110
Fig. 88. SEM of torsional leg and inchworm motor.	111

ACKNOWLEDGEMENTS

I would like to thank my dissertation committee and my qualifying examination committee for their time, helpful guidance, and input: Professor Kristofer Pister, Professor Albert Pisano, Professor Roger Howe, Professor Richard White, Professor Richard Marcus, and Professor Bernhard Boser.

Furthermore, I would like to thank all of those who worked closely with me and contributed substantial insight and knowledge into the designs and creation of microrobots. Anita Flynn from MicroPropulsion, Inc. has shown an unwavering dedication to the field. Her go-out-and-get-them attitude has been indispensable in the often tenacious battle of creating walking microrobots. If anyone can be described as a one-man-army, that would have to be Chris Keller from MEMS Precision Instruments. His ability to construct equipment and provide reliable services and fundamental knowledge in the area of material processing is deeply appreciated. Richard Yeh, with whom I had the honor of working, helped lay the foundation on which this dissertation is based. Colby Bellew not only established solar power as a practical power source for microrobots, he also mentored me in the microlab. His methodical approach to processing taught me the importance of diligence and patience for the successful fabrication of devices.

Additional thanks goes to the Berkeley Microfabrication Facility. The microlab gave me the flexibility for novel processing and the sophisticated equipment required for my work. Special thanks goes to Robert Hamilton who helped in many ways from processing suggestions to designing vacuum furnaces. Furthermore, Joe Donnelly, Phillip Guillory, Jimmy Chang, and Katalin Voros all deserve further thanks for their time and efforts. James Wu from the Lawrence Berkeley National Laboratory helped with additional vac-

uum furnace testing. Dimitry Kousminov from Accurel Systems provided crucial material analysis services.

I am deeply indebted to the National Science Foundation for their three-year fellowship. The fellowship provided me with the necessary funds to pursue research in an independent manner. Additional funds were provided by BSAC sponsors and DARPA/ITO SDR.

I would like to thank all the graduate and undergraduate students in Professor Pister's group. Special thanks goes to Sarah Bergbreiter who provided direct assistance in the first years as a graduate student, as well as Matthew Last, Brian Leibowitz, Brett Warneke, and Piotr Prokop.

Lastly, I would like to thank my family: my parents, Bernie and Cynthia; my sisters, Jennifer and Mollie; Mollie's husband, Jim; and Dave, who is practically family, being my closest friend since the third grade. Most of all, my wife, Liz, has been a stalwart of support during my study. Not only has she shown the love and companionship of a true friend, she also contributed both drawings and helpful suggestions to this dissertation.

Chapter 1. Introduction



Fig. 1. Image of the Autobots from the The Transformers TV show (1984).

Robots capture the public imagination and are a symbol of the future. From the 1927 silent movie, *Metropolis*, to Brian Aldiss's story-turned-movie, *Artificial Intelligence*, robots have been characterized anthropomorphically in almost all traits: weak and powerful, jealous and generous, stoic and emotional. *Robotech*, *Blade Runner*, *The Transformers* (see Figure 1), *Star Wars*, *2001*, *The Matrix*, *Black Hole*, *Lost in Space*, *Star Trek* - the list goes on. While the abilities of robots created in the imagination seem boundless, robots in the real world achieve only a tiny fraction of the behavior attained by their imaginary brothers. Still, they perform tasks for us that we rarely notice: car manufacturing, IC manufacturing, aerial monitoring (The Predator drone), handling of nuclear material, and space exploring. Robots are even being commercialized for use in telerobotic surgeries [5, 27].

In an effort to contribute to the ever growing abilities of robots, we introduce a tiny member of the robot family in this dissertation. This robot representative is a millimeter-sized, self-mobile robot weighing a mere 10 mg, or about 1/100th the weight of a paper clip. Microrobots, as Dario defined them in 1992, are “a sort of ‘modified chip’ fabri-

cated by means of silicon micromachining technologies, and containing micromotors, sensors and processing circuitry” [10].

The idea of microrobots has been around for the last 15 years; some would say even longer, dating back to Feynman’s seminal paper, “There’s Plenty of Room at the Bottom” [15]. In 1987, the IEEE Robotics and Automation Society held the first Microrobots and Teleoperator Workshop, now called the MEMS conference. In 1989, Anita Flynn coined the term “Gnat Robots.” She discussed the value of having millimeter-sized, cheap, disposable robots and discussed their manufacturability [16]. *The Diamond Age* by Neil Stephenson, published in 1995, describes the future in which small robots are seamlessly integrated into people’s daily lives.

According to the 2002 Guinness World Records [22], the smallest autonomous robot was made by Seiko Epson in 1992. It measured 1 cm in height, weighed 1.6 grams, and was driven with wheels (Figure 2). Other small “wheeled” autonomous robots include K-Team’s commercial robot, Alice, and Sandia’s 1/4 cubic inch robot [1, 9] (Figure 3). These robots were manually assembled using a number of off-the-shelf components: transistors, gears, microprocessors, circuit boards, plastic molded frames, axles, IR sensors, etc.

My motivation for this dissertation is to build millimeter-scale robots with on-board power and intelligence through silicon micromachining. The promise of micromachining is that sensors, actuators, and electronics can all be fabricated on the same piece of silicon, side-stepping the costly effort of assembling one part at a time. MEMS, or microelectromechanical systems, utilize techniques from semiconductor processing but in addition to electronic devices, micro-sized mechanical devices are also fabricated. Over the past decade, electronics and MEMS have enjoyed the benefit of newer fabrication technol-



Fig. 2. Monsieur robot by Seiko. The robot measures 1 cm in height and weighs 1.6 grams.



Fig. 3. 1/4 cubic inch robot from Sandia National Laboratory. The robot weighs less than one ounce.

ologies, enabling even more functionality in smaller devices. With the recent advances in MEMS actuators and linkages, autonomous walking microrobots have become a real possibility.

In this dissertation, we discuss the design, fabrication, and testing of an autonomous, mobile microrobot from start to finish. Chapter One outlines the relevant research that supported the development of this microrobot. This chapter outlines the operation of the inchworm motor and provides a basic understanding of solar cells. Chapter Two discusses the two in-house fabrication processes used to manufacture the robot including the final assembly. With the processes already discussed, Chapter Three goes into the design of the robot and its subsystems: mechanical actuation, power, and control. Chapter Four presents the results including autonomous robot motion.

While we focus on a single type of autonomous low-power silicon robot, our intention is to lay the foundation for creating a whole class of autonomous microrobots based on the same fabrication and assembly schemes presented in this dissertation. For example, instead of a simple two-legged robot, one could imagine designing and fabricating an 8-legged arachnoid that spins silicon as its thread. Another possibility is designing a

grasshopper robot with powerful legs for jumping 10 cm in the air. However, before larger dreams can be realized, we start here with a simple statically-stable mobile robot with two one-degree-of-freedom (DOF) legs. Dragging its tail, the robot is designed to move forward via coordinated movement of its legs.

1.1 History

Microrobots have been a key interest since the beginning of micromachining. Clearly, the ability to integrate electronics with mechanical actuators made micromachining an attractive fabrication possibility. For the past decade, a number of researchers have worked towards the synthesis of an autonomous microrobot using a variety of locomotion schemes [3, 8, 18, 19, 29, 31, 45, 46]. Yeh *et al.* created microrobotic components such as rigid links, mechanical couplings, and electrostatic motors in a commercial micromachining foundry [55]. Using these components, an insect-like articulated microrobot with multiple DOF legs could be built (Figure 4). Shimoyama *et al.* suggested providing external actuation and power through vibratory or magnetic fields [54, 36]. Ebefors *et al.* created a tethered walking microrobot measuring $15 \times 5 \text{ mm}^2$ (Figure 5). The robot could carry 30 times its own weight and was actuated with heated polyimide joints [12]. Yasuda built a robot that was propelled by a vibrating floor. The links had different resonant frequencies, so the robot was controlled through selective frequency vibrations of the PZT floor [54].

1.2 Motors

One of the fundamental issues in microrobot design is creating power-efficient, large-deflection, and high-force actuators. At minimum, the microrobot must generate sufficient force to lift itself up. A number of actuators has been developed for use in MEMS and nanotechnology. The major actuator classes used in designing robots are elec-

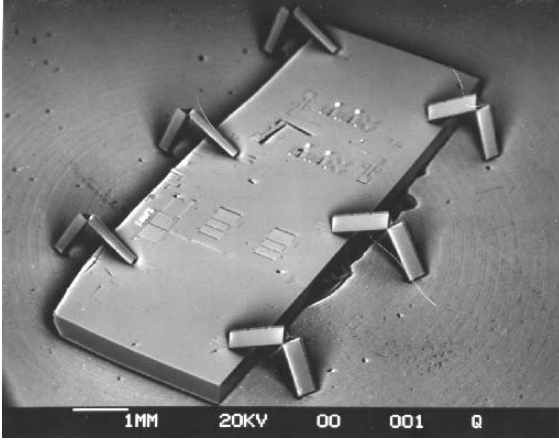


Fig. 4. Mock-up of a six legged microrobot. This robot from Yeh is fabricated using MUMPS. While it does not have integrated motors, it does have 6 two-DOF legs [55].



Fig. 5. A tethered walking microrobot. The robot could carry 30 times its own weight and was actuated with heated polyimide joints [12].

tromagnetics, electrostatics, thermal expansion, shape-memory alloys (SMA), and piezoelectrics. A survey of these actuators can be found in [13, 19, 51]. Thermal based actuators and SMAs rely on heating for actuation and generally have very low power efficiencies. Electromagnetics, while efficient on the macro-scale, require large magnetic fields that do not fit well in a small form factor. Piezoelectric actuators offer excellent force densities and high quality factors. Currently, however, an easy and convenient method of fabricating these devices in a micromachining process has proven difficult. By manually assembling the piezoelectric actuators, Yan *et al.* demonstrated flapping wings that generate lift for a micro-flying insect [52].

Force densities of electrostatic actuators are about an order of magnitude lower than those of piezoelectrics [13] but integrate very easily into standard silicon processing. For a parallel-plate gap-closing actuator (GCA) (see Figure 6), a good approximation of the force is:

$$F_e = \frac{1}{2} \epsilon_o \frac{tL}{g_f} V^2 \quad (1)$$

where

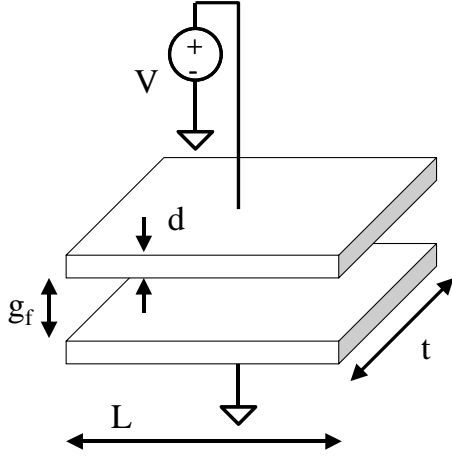


Fig. 6. Diagram of a gap closing actuator (GCA).

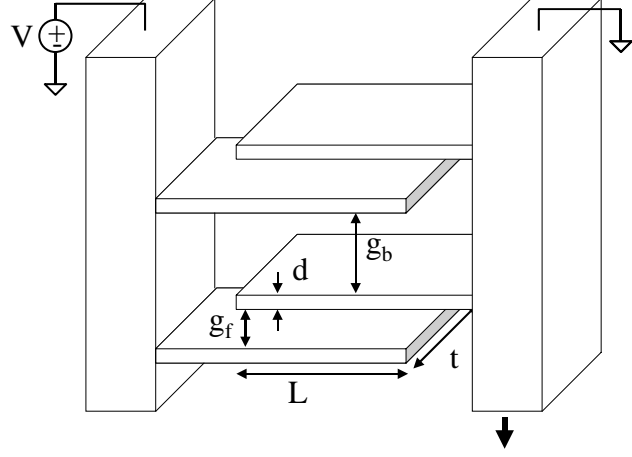


Fig. 7. Diagram of a GCA array. Here g_f represents the forward actuating gap and g_b is the backward attracting gap.

t is the width of the beams
 L is the length of the beams
 g_f is the forward gap between the beams
 V is the voltage between the beams
 ϵ_0 is the permittivity of air

To generate high force densities, the gap should be as small as possible and the voltage as large as possible. In MEMS technologies, large arrays of GCAs can be fabricated in parallel to generate millinewtons of force. A cross section of a GCA array can be found in Figure 7. The areal force density of the actuator is equal to the total force divided by the total area. In this conceptual case, a GCA array has an areal force density of:

$$\sigma_{GCA} = \frac{F}{A_{GCA}} = \frac{\epsilon_0 V^2 N t (g_f^{-2} - g_b^{-2})}{2(2d + g_f + g_b)} \quad (2)$$

where

N is the number of GCAs in the array
 g_b is the backward gap between two adjacent GCAs
 d is the thickness of the beams

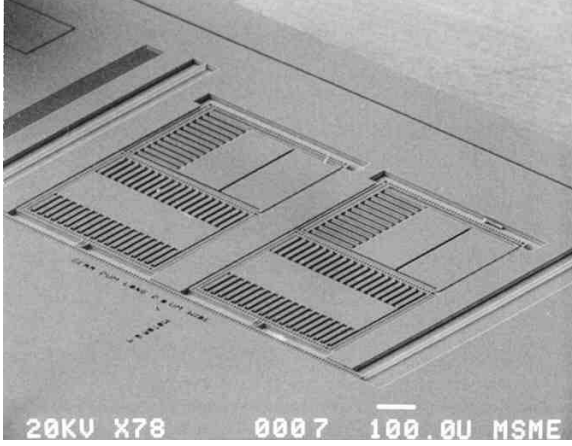


Fig. 8. Single mask SOI inchworm motor. Developed by Yeh *et al.* These actuators provide large force and displacement with high efficiency electrostatics.

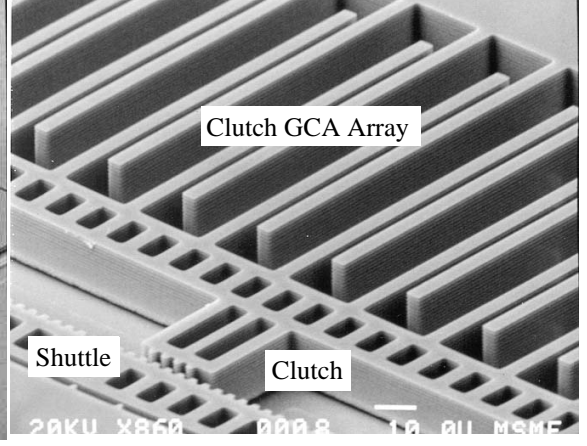


Fig. 9. Close-up view of clutch and shuttle. The clutch engages the shuttle with teeth to reduce slippage. The ratcheting action of the drive GCA array (not shown) pulls the shuttle forward.

To maximize the force density of the actuator, individual GCAs must be packed tightly together. However, increasing the spacing from one GCA to the other, g_b , could reduce the total amount of output force. Since g_f is usually limited by the minimum resolution of the process, g_b can be chosen so as to maximize σ_{GCA} . g_b^{opt} can be calculated by taking the derivative:

$$\frac{\partial}{\partial g_b} \sigma_{GCA}(g_b^{opt}) = 0 \quad (3)$$

This results in a cubic polynomial in g_b :

$$\left(\frac{g_b}{g_f}\right)^3 - 3\left(\frac{g_b}{g_f}\right) - 2\left[1 + 2\left(\frac{d}{g_f}\right)\right] = 0 \quad (4)$$

Yeh found that for practical actuators, the optimal ratio of g_b to g_f is around 2.2 to 2.5 [58].

Electrostatic actuators are extremely efficient since they do not dissipate static power. In fact, most of the loss comes from how the actuator is controlled. With an

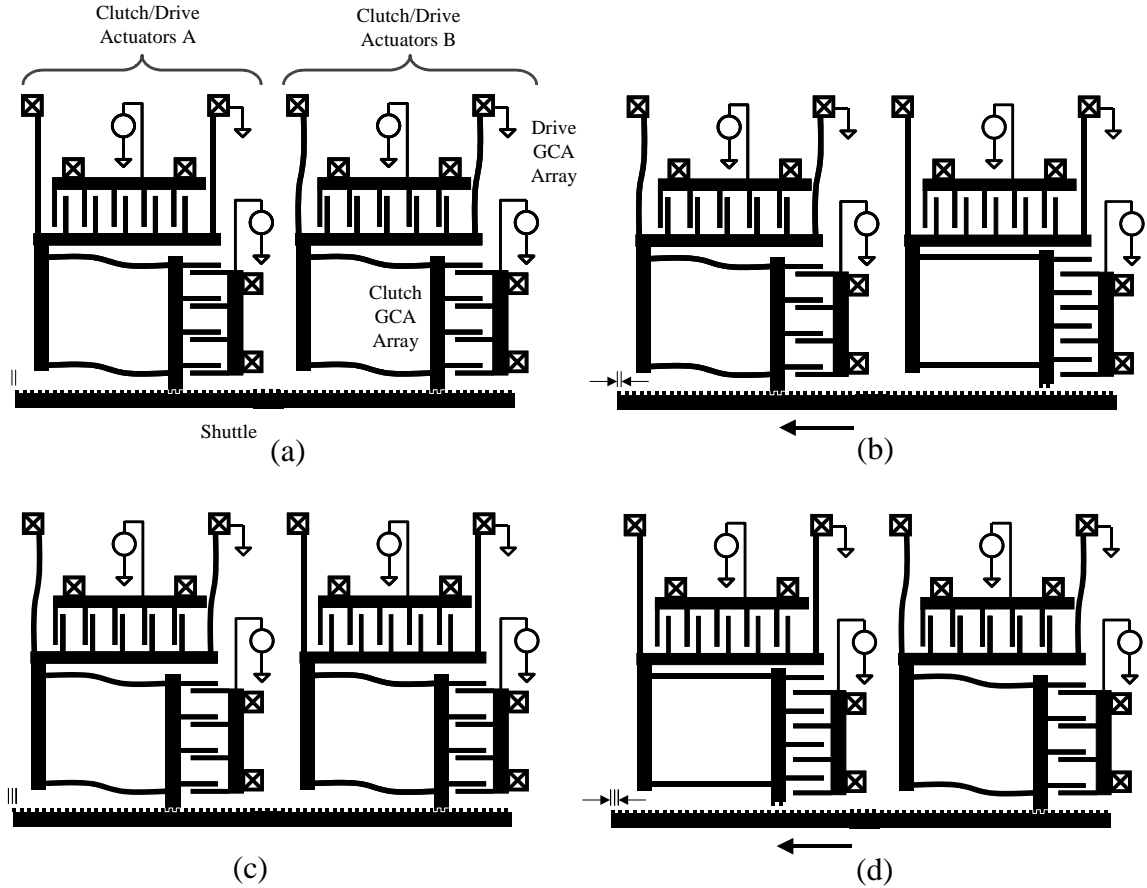


Fig. 10. Diagram of an inchworm cycle. (a) clutch A engages shuttle (b) clutch B disengages shuttle and drive A pulls shuttle forward (c) clutch B engages shuttle (d) clutch A disengages shuttle and drive B pulls shuttle forward. Cycle is then repeated.

appropriate choice of the inductance, an L-C tank can be used to raise the voltage beyond that of the original power supply. In GCAs, we estimate that an inductively charged controller-actuator can be up to 80% efficient. Voltage-controlled actuators, where the controllers are much simpler in design, suffer from increased charge injection during actuation.

While “large” forces can be attained electrostatically, small displacements limit the overall usefulness of gap-closing actuators. The inchworm electrostatic motor overcomes this stumbling block. The motor decouples actuator force from total travel and allows the use of electrostatic actuators to achieve large force and large displacement. Figures 8 and

Table 1: Inchworm Sequence

Step	Clutch A	Drive A	Clutch B	Drive B
a	1	0	1	1
b	1	1	0	0
c	1	1	1	0
d	0	0	1	1

9 show an inchworm motor fabricated in a single mask SOI process. The operation of the motor is very similar to someone climbing a ladder, by consecutively grabbing and pulling oneself up one rung at a time. Instead of using hands and feet to move up the ladder, the inchworm motor uses sets of clutch and drive actuators to grab and pull a shuttle forward. The inchworm is composed of four sets of GCA arrays: two drive actuators and two clutch actuators. Each clutch/drive actuator pair is used to inch the shuttle forward (Figure 9). The clutch actuator engages the shuttle, and once engaged, the drive actuator pulls the shuttle forward.

Figure 10 shows the operation of the inchworm and Table 1 shows the input sequence to the actuators. Yeh's original 50 μm SOI electrostatic motors exhibited a force density of 87 $\mu\text{N}/\text{mm}^2$ at 33 V with an estimated energy efficiency of 8% [57].

1.3 Articulated Links

Articulated links transfer the forces generated by the motor to the legs of the microrobot. One issue with planar micromachining is creating 3D structures from an inherently 2D process. In 1992, Pister realized 3D fold-up structures by creating pin-in-slot microhinges from polysilicon [39]. This was followed by Suzuki who created a 3D microrobot skeleton that could be actuated electrostatically by using polyimide flexural hinges [45]. Previous work by Yeh showed how hollow-triangular-beams (HTB) could be used to make 3D structures from an inherently 2D process [55] (Figure 11). Similar to

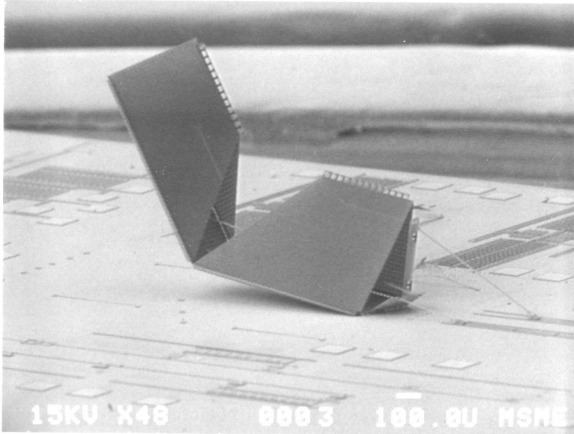


Fig. 11. Two-DOF legs without actuation. The legs are assembled with hollow-triangular beams made from polysilicon [56].



Fig. 12. Legs with thermal actuation. One and two-DOF poly-Si legs with hinged thermal actuators [31].

origami, HTBs can be made by “folding” up three flat polysilicon plates. In 1999, Kladi-tis *et al.* built one- and two-DOF polysilicon legs. Using pin hinges, he rotated the legs 90° out-of-plane and actuated the legs thermally [31] (Figure 12).

1.4 **Microcontrollers, Sensors, and Communication**

No autonomous robot is complete without the ability to communicate, compute, and sense its environment. Much of the effort to provide millimeter-sized components was through the Smart Dust project [48]. Smart Dust’s goal was to build an autonomous sensing, computing, and communicating node in a millimeter-sized package (Figure 13). Subsystems on board this prototype included customized CMOS electronics for computation and a temperature sensor. Additionally, optical communication was accomplished using a MEMS corner-cube-retroreflector (CCR). Doherty *et al.* provides a theoretical analysis of the power constraints of such a system [11].

For robots in general, the computational power can be as simple as an array of relays or as complicated as an Intel microprocessor. Many inch-sized robots use 8-bit microcontrollers, most notably from Microchip Technology, Inc. Future microrobot colo-

nies can include a means for interacting with the environment through sensors. Among the milli-sized sensors available today are temperature sensors, accelerometers, magnetometers, microphones, light sensors, and humidity sensors.

To have a mobile robot community or to control the motion of the robot, a communication system must be in place. Communication can be accomplished with either optical or radio frequency (RF) communication. MEMS corner-cube-reflectors (CCR) modulate reflected light to transmit data [59]. The asymmetric nature of the communication system, though, requires one device to house the laser - the interrogator - while the other device communicates with a CCR. The energy cost of the CCR communication is extremely low, ~100 pJ/bit, but peer-to-peer communication would be impossible due to the power requirements of the interrogating laser (usually milliwatts). As an alternative, laser beam steering can achieve peer-to-peer communication at relatively low power costs [33, 35]. For example, a communications system could be developed with a laser power of 50 μ W, a maximum range of 1.4 meters, and a received power cost of 20 pJ/bit.

RF communication is well established in the commercial world. In particular, the Bluetooth standard appears to be the most promising for civilian sensor networks, with short-range communication costs of roughly 100 nJ/bit in the 2.4 GHz band with a range on the order of 10 meters.

1.5 Solar Cells

Conventionally, solar cells are thought of as large flat panels used to harness the power of the sun from either a terrestrial or space position. Nonetheless, solar cell technology is branching out to appear in watches and calculators, and now it is surfacing in MEMS research. The advantage of solar cells is based on the immense power of the sun

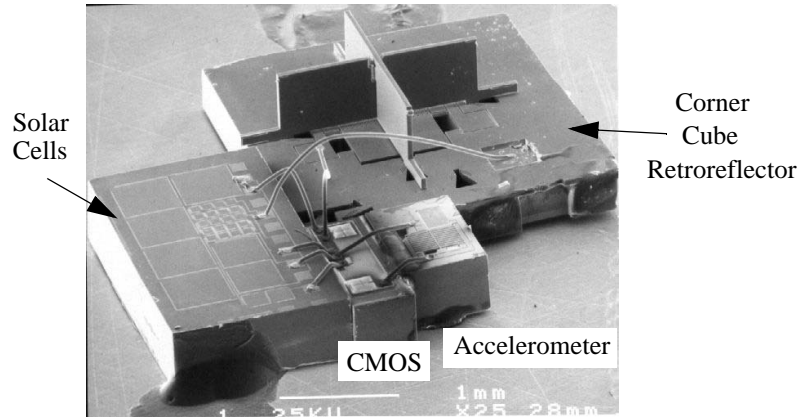


Fig. 13. Smart dust node. The node is composed of four chips: 1) solar cells, 2) general CMOS, 3) corner-cube retroreflector, and 4) MEMS accelerometer.

which radiates $\sim 1 \text{ kW/m}^2$ of optical intensity onto the surface of the earth. As a comparison, light intensity under normal indoor lighting conditions is $\sim 2 \text{ W/m}^2$. While multiple materials can be used to create solar cells, a steady trend shows that crystalline silicon now dominates the world solar cell market with 86% of the market share [20]. Amorphous silicon, its closest rival, encompasses 13% of the market.

1.5.1 Solar Cell Fundamentals

To understand the operating fundamentals of the solar cell, first we must take into account the light spectrum in which the solar cells operate. The sun emits radiation from ultraviolet wavelengths to infrared wavelengths. To a first-order approximation, the solar spectrum resembles that of a black body at 5900 K [20]. More genuine standards come in the form of AM0 and AM1.5, where AM stands for “air mass.” AM0 is the solar spectrum just above the Earth’s atmosphere without any atmospheric attenuation, and AM1.5 is the “average” spectra throughout the day as the sun traverses the sky [38 p.23].

Conventional solar cells employ generated hole/electron pairs in a PN junction to convert solar power to electrical power. Solar cell efficiency and absorption depends on two key factors: the bandgap and whether it is direct or indirect. The bandgap is defined

Table 2: Intrinsic Material Efficiencies [38]

Material	Efficiency	Bandgap Energies (eV)	Direct/ Indirect Bandgap
Si	24.5% [5]	1.12	indirect
GaAs	27.8%	1.43	direct
a-Si	12%	1.6	direct
CdTe	15.8%	1.5	direct

as the difference in energy between the top of the valence band and the bottom of the conduction band. Bandgap energies on the order of 1.4 eV to 1.6 eV yield the most efficient solar cells. Silicon's bandgap is a little lower at 1.1 eV. Table 2 below lists the intrinsic efficiencies of popular solar cell materials.

For direct bandgap semiconductors, a single photon whose energy is greater than the bandgap can create a hole/electron pair. For indirect bandgap semiconductors, the process is a two-step phenomenon, involving a photon and a phonon. The probability of this two-particle event occurring is much smaller than the single photon event in a direct bandgap semiconductor. Hence, absorption of light is greatly reduced for indirect bandgap semiconductors [21 p.47]. To obtain 90% absorption of light in silicon, an indirect bandgap material, the solar cell requires a silicon thickness of 100 μm . GaAs, a direct bandgap material, requires only 1 μm [20]. For microrobots, the weight contribution from silicon solar cells could be substantial compared to that of direct bandgap materials.

Examples of popular solar cell materials with a direct bandgap structure are amorphous hydrated silicon, GaAs, CdTe, and CdS. Indirect bandgap materials are Si, Ge, and SiCAlAs. A comprehensive table can be found on p.206 in [25].

1.5.2 Single Cells

Hebling showed that solar cells can be fabricated by growing 46 μm of epitaxial

silicon on a layer of SiO₂ [23]. Both the P- and N-type contacts were made on the top surface by means of an interdigitated front grid structure. This reduced the complexity of supplying backside contacts to the buried layer. A back surface field of highly doped P-type silicon was used to reduce the series resistance of the cell. Efficiencies up to 18.2% were demonstrated.

1.5.3 Stacked Cells

For MEMS and microrobots, the major actuators are electrothermal, electrostatic, piezoelectric, and magnetic. The electrothermal and magnetic actuators often require currents larger than those obtainable from reasonably sized solar cells. Electrostatic and piezoelectric actuators, however, have extremely low DC leakage current. Often electrostatic actuators require 10s to 100s of volts with currents ranging from nanoamps to picoamps. For a single cell, the open-circuit voltage (V_{oc}) does not exceed one volt. Solar cells, however, can be placed in series in order to increase their overall output voltage. The following three papers present fabrication techniques for stacking solar cells on a single substrate.

1. Ohsawa *et al.* stacked 24 cells on a single substrate, generating an open-circuit voltage of 22.5 V [37]. The total area of the solar cell stack was 800 μm x 1500 μm . Ohsawa used GaAs wafers that were doped with CrO at the surface. Isolation was achieved by etching 3 μm deep trenches around the cells, using polyimide as an insulating layer and then electrically connecting cells with AuGe/Au and AuZn/Au.

2. In another example, Lee *et al.* demonstrated 150 V from amorphous hydrogenated silicon (a-Si:H) in an area no larger than 1 cm^2 under AM1.5 [34]. A single-cell triple-layer stack yielded a V_{oc} of 1.8 ~ 2.3 V. Because amorphous silicon is a direct bandgap semiconductor, only 1 μm of amorphous silicon was needed to absorb most of

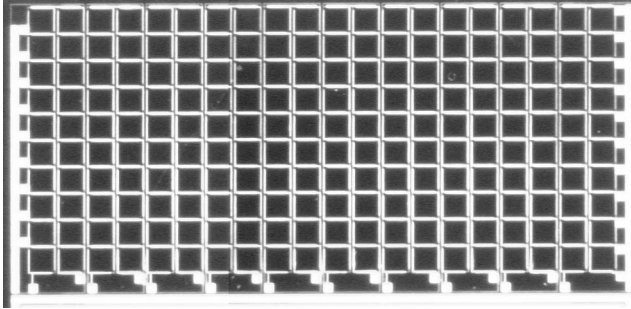


Fig. 14. Die photo of solar cell arrays. The 20 x 10 array of solar cells (10 mm x 5 mm) has been shown to have about 100 volts of open-circuit output voltage. Bellew later demonstrated the integration of MEMS, solar cells arrays, and electronics all on the same substrate. Efficiencies of the solar cells were as high as 15% [6].

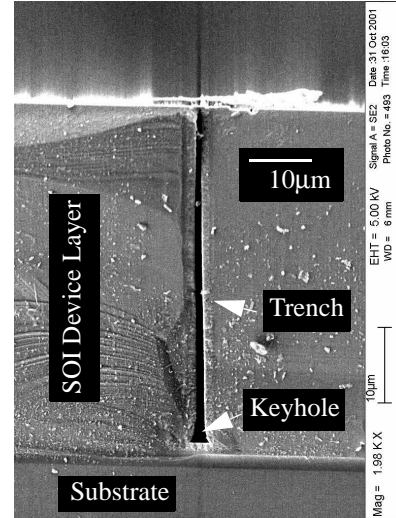


Fig. 15. SEM of isolation trench. Isolation trenches coated with nitride and undoped polysilicon isolated blocks of the device layer in SOI wafers [6].

the light. With such thin films, electrical isolation around solar cells was readily micromachined. The calculated efficiency was 0.16%. As a demonstration of a full system, Lee actuated an electrostatic micromirror with the solar cells in a hybridized system.

3. Bellew has demonstrated stacked single crystalline silicon solar cells on a silicon-on-insulator (SOI) substrate [6]. Much like Hebling [23], he uses the buried SiO_2 layer as the insulator and provides front-side contacts for both the N and P regions. Isolation is accomplished by performing a Bosch-process advanced silicon etch (ASE) through the device layer. The trenches measure $2 \mu\text{m}$ in width (Figure 15). The trenches are back-filled and electrically isolated with nitride and undoped polysilicon [7]. The wafer is then planarized for successive lithographic steps. Because of silicon's indirect bandgap, device layer thicknesses on the order of $\sim 50 \mu\text{m}$ were used. He has demonstrated a micro-solar cell array with a V_{oc} of 88 V in less than 50 mm^2 of area. Single cells demonstrated efficiencies as high as 15%. Going one step further, Bellew integrated NMOS transistors and solar cells with a MEMS gap-closing actuator on the same substrate.

1.6 **Microbatteries**

One issue with solar power is the intermittent availability of light. [32] surveys the feasibility of micro-power supplies. A possible solution is to integrate rechargeable batteries with solar cells to maintain vital functions of a device during dark periods. The most likely types of microbatteries would be lithium and zinc-air. Newer lithium batteries are rechargeable and have energy densities on the order of $2,000 \text{ J/cm}^3$ [11]. As an example, if the microrobot were to contain a 1 mm^3 battery, the battery's energy capacity would be 2 Joules and its weight, 2 mg. Zinc-air hearing aid batteries have even higher energy densities, $4,600 \text{ J/cm}^3$ [47].

More exotic power sources include vibrational and nuclear energy. Roundy *et al.* has demonstrated a millimeter scale vibrational energy harvester using PZT as the transducer [42]. Lal has used a beta emitter radiation source to electrostatically actuate a cantilever [26].

1.7 **Microrobot Applications**

Let us imagine, for the moment, future microrobots: ones equipped with a choice of sensors, behavioral processing capabilities, and reasonable communication systems. With not just one such robot but a whole colony of robots, the plethora of design variations and applications instantly becomes apparent.

In this section, we consider a set of revealing applications for robotic sensor networks. Based on the requirements of each application, we estimate qualitatively the energy budget and the expenditures required of the robotic network. Each scenario involves a disparate set of constraints and performance criteria; we expound on applications such as surveillance and search and rescue. Lastly, we consider the feasibility of using microrobots for Mars exploration and antenna construction.

1.7.1 Tracking Scenario (Surveillance)

The goal is to sense and track activity in buildings in a military setting. While surveillance can also be performed with immobile devices, microrobots have the additional ability to move toward areas where they can sense information more readily or to improve communication with their peers.

As an example, consider monitoring the inside of a building using microrobots. First, the robots are delivered to the site by being dropped out of a microairplane over and around the building of interest. The robots then must establish an ad-hoc network under highly variable transmission and reliability conditions. Robots that are out of communication contact with their peers can perform a random walk in an attempt to gain contact. The preferred method of communication would be agile laser beam steering, with communication ranges on the order of meters. Once a network is established, robots could walk towards areas of darkness; presumably towards the building; underneath door frames. If the layout of the building were known, perhaps a more intelligent algorithm could be attempted to locate the front door.

Robots would only scout around so long as they stayed within the communication range of the network. Some robots could act as relay stations transferring information from one robot to the next. Once inside, temperature, humidity, and lighting conditions could be recorded. While for outdoor operation the robots can rely on solar cells, inside and during the night, the robots would have considerably less power to communicate, move around, and sense their environments. To solve this problem, the robots could use a one-mm³ lithium battery source (2 J of energy) which could be recharged during the day.

To outline the requirements for the robot's mobility, we must first determine the energy dissipation for each cycle of the robot. Inchworm motors have only been demon-

strated with 8% efficiency, but by using charge-controlled driving electronics, the efficiency could be close to 50%. For a reasonable estimate of the generalized robot, the motor would dissipate 2.4 nJ per micron of travel. For simplicity's sake, we assume that one micron of travel for a single motor translated to a micron of travel for the microrobot, with motors operated one at a time. In that case, for two joules of energy, a robot could travel almost a kilometer. This, of course, does not include power needed for sensing and communication.

1.7.2 Human Detection in Post Earthquake Rescue Missions

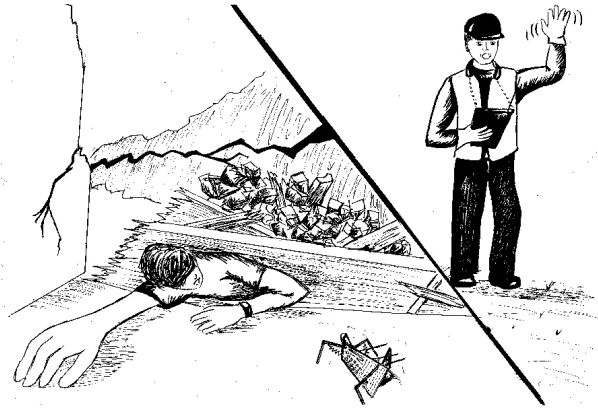


Fig. 16. Earthquake scenario. Robots scour through collapsed buildings in search of survivors.

In this scenario, the goal is to locate people trapped in collapsed buildings after devastating earthquakes like those in Turkey (1999) and El Salvador (2000). The robots' role would be to locate humans trapped in the debris. Using environmental factors such as acceleration, temperature, and sound, the robots could detect the movement, heat, and/or voices of a trapped person. The job of the robot network would be two-fold. Some devices would burrow through the open crevices of the debris in search of human life. Other robots would act as communication relays that would transmit information along a networked line to the surface.

As an example, emergency personnel could deploy tens of thousands of these

devices on the surface of the collapsed building. Immediately, the robots would haphazardly start burrowing downward using their accelerometers to determine which way was down. Some of the robots would burrow just a little ways and then stop. These robots would act as repeaters, sending information from the robots below to the surface. Other robots with temperature sensors might try to detect human body temperatures. Those temperatures might be at or below $37.5\text{ }^{\circ}\text{C}$ as people in a state of shock have suppressed body temperatures. Still other robots might be equipped with chemical sensors that could home in on chemical signatures of the human body. And still others would use microphones to detect sounds that might have frequencies within the human voice range.

Once there was sufficient evidence that a person was found, the location of the human would need to be deciphered. The robots on the surface would be equipped with corner cubes to spatially locate robots that identified a victim. The surface robot that would be relaying the signal of human life could be used as a starting point to begin searching in a specific site. That search could include deploying a concentrated amount of microrobots in that area or manually searching through the debris.

While in the debris, robots will not have access to sunlight, so they would rely on battery power. Additionally, their operation would be limited by the energy requirements to maneuver through debris. For instance, if it takes 100 meters of random walking to travel downward 10 meters in rubble, walking alone would consume 0.24 J. During their random walk they could periodically communicate with other robots and check for human vital signs. If the robots travelled at a rate of 1 mm/s, then it would take them 100 kiloseconds or 28 hours to burrow 10 meters.

1.7.3 Construction Scenario

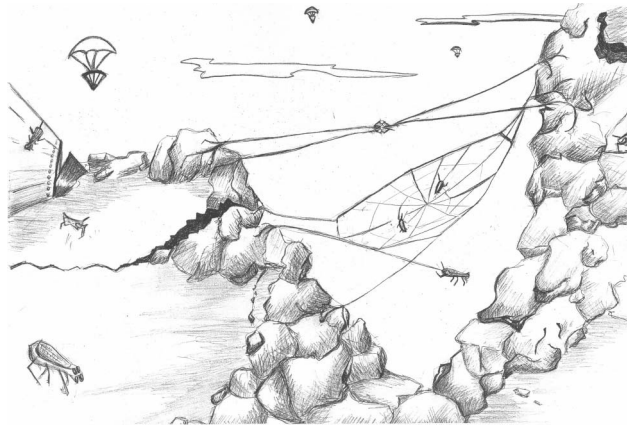


Fig. 17. Mars exploration scenario. Robots explore the surface of the planet and collectively build a satellite dish.

While microrobots can operate in a haphazard manner monitoring the environment or performing search and rescue missions, they can also work as a cooperative community to perform high level tasks. Much like a community of ants building a nest, microrobots could work together to form structures or perform tasks that the individual robots could not do themselves. An application would be the deployment of microrobots to the surface of the planet Mars. Previous Mars missions (Mars '98 and Mars Surveyor) have focused on smaller orbiters and landers that would be both inexpensive and expendable. We can go one step further. One particular advantage of using microrobots is that they can significantly reduce the overall weight of the rocket's payload. Suppose, for example, each robot weighs a total of 1.7 mg. If we deploy one million microrobots to Mars, the total weight of the robots would be 1.7 kilograms. With such little weight, the associated transportation costs to the Red Planet would be limited to a deployment system for the microrobots and a Mars orbiter for relaying information back to Earth.

In this particular scenario, environmental sensors on the robots would include light sensors, thermometers, and specialized chemical sensors tailored to the Mars atmosphere. Some robots would have one sensor; others a different sensor, and so forth. If the

microrobots were capable of communicating up to three meters away, then after landing, the robots could spread themselves out so that they maximized the total surface being monitored. For one million robots, the total area would be a circle of radius 2.7 kilometers. However, it would take an entire month to travel from the center to the edge of the circle.

To relay information back to the Mars orbiter, the robots could construct a directional satellite antenna. By welding silicon beams together with high current, much as a spider might spin a web, the robots would construct and position their own satellite (see Figure 17). By linking solar-cell power from individual devices, enough RF power could be generated to transmit to the orbiter, which in turn would relay the findings back to Earth. Several such “colonies” of microrobots could be dispatched to Mars.

Chapter 2. Fabrication and Assembly

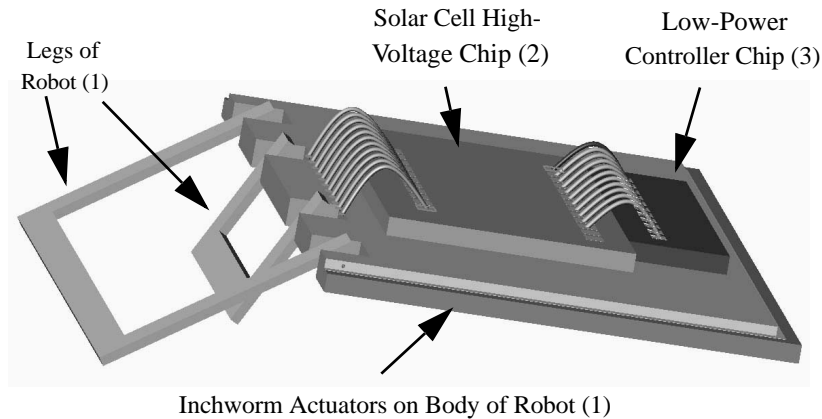


Fig. 18. Computer modeled rendering of walking robot. The three-chip hybrid is composed of chips made from three fabrication processes: 1) legs and motor process, 2) solar cells and high-voltage process and 3) low-power CMOS process.

2.1 *Microrobot Concept*

At the beginning of this project, there was no known “process” or manufacturing scheme to combine a solar power source, large force motors, and out-of-plane MEMS linkages. While a unified process that combined electronics and MEMS together seemed appealing at first glance, the time and energy required for such a development would have been more appropriate for a large company than a small group of researchers. Therefore, we broke down this difficult task into separate processes, allowing us to manage complexity while maintaining freedom of design.

We decided to decompose the problem into three facets: (1) control, (2) power, and (3) mechanical motion. Figure 18 shows a conceptual image of the final robot. (1) The digital sequencer (controller chip) controls the operation of the motors and coordinates open-loop walking. This controller was fabricated by National Semiconductor Corporation in their 0.25 μm , five-metal layer process. (2) Not only is solar power an abundant source of energy, but solar cells integrate easily with existing electronics. Following the

Table 3: Mask Names for Icarus Process

Lithographic Step	Description	Mask Name	Figure Reference
1	Alignment	Align	21a
2	P- Well Field Implant	PMINUS	19b
3	N- Well Field Implant	NMINUS	19b
4	Poly Gate	POLY	19c
5	N+ Implant	NPLUS	19d
6	P+ Implant	PPLUS	19d
7	Isolation Trench	ISO	19e
8	Contact	CONT	19i
9	Metal	METAL	19j
10	SOI Structures	WELLSTR	24a

work of Bellew [6], we developed a process that allowed us to combine solar cells and high-voltage buffers on a single SOI substrate. (3) Lastly, the mechanical process was chosen to incorporate large-force electrostatic actuators with polysilicon pin hinges. The enabling technology for this process is a novel planarization step that allowed subsequent polysilicon deposition on an SOI wafer after a silicon device layer etch [53]. After all three chips were fabricated, we manually assembled the robot.

As a matter of simplicity, our initial design included neither communication systems nor sensors. For that reason, the controller operated open-loop, simply sequencing the legs to achieve a forward walking gait.

The following sections discuss the fabrication of the microrobot based on two in-house processes, the solar cell process and the mechanical process. Lastly, final assembly of the robot is discussed.

2.2 Solar Cells, Transistors, and Isolation Trenches - Icarus Process

As mentioned previously, power is delivered by solar cells from one of the three chips that compose the robot. The process was adapted from the work of Bellew [6] (see

Section 1.5.3). Using three ion implants and aluminum as the gate material, Bellew demonstrated 30 V transistors and solar cell supplies up to 88 V. With the addition of two more masks, the CMOS process described in this dissertation has gate-aligned transistors with breakdown voltages ranging from 42 V to 100 V, in addition to high-voltage solar cell supplies. The process was fabricated in-house in the Berkeley Microfabrication Facility.

Our process is dubbed Icarus, after the mythological story of Icarus and his father, Daedalus¹. Before continuing, it is important to point out the disadvantages of using silicon for solar cells. As mentioned in Section 1.5.1, silicon has a bandgap energy of 1.12 eV and is an indirect bandgap material. For high absorption, silicon solar cells need thicknesses of 100 μm , and in the Icarus process, we used a device layer that was substantially thinner (15 μm) at the cost of less absorption. With such large thicknesses, silicon solar cells could contribute a substantial part of the weight to a robot compared to direct bandgap materials. In the prototype robot's case, 22% of the weight comes from the Icarus die, but most of that is contributed by the 135 μm -thick substrate of the SOI. Furthermore, the silicon's bandgap is not as ideal as other materials, which causes its efficiency to suffer. Nonetheless, the ease of integration of silicon solar cells into existing CMOS processes made it an attractive choice.

2.2.1 Icarus, the Solar Cells and the High-Voltage CMOS Process

In short, Icarus is a 9-mask, gate-aligned, CMOS process with isolation trenches. The layers are listed in Table 3. One mask is used for alignment purposes, seven masks

¹Daedalus, a famous inventor, fashioned wings with wax so that he and his son could escape an island. Icarus' father, however, warned him not to fly too close to the sun. Flouting his father's warnings, Icarus flew as high as he could, only to have his wings melt. To his father's great sorrow, Icarus plummeted into the sea and perished. While some may suggest that Icarus is a poor choice to name the solar cell process: we name it so in irony; while Icarus was doomed by the sun, our robot operates only because of the sun.

Table 4: Ion Implantation Doses and Energies

Process Step	Species	Energy (KeV)	Dose (cm ⁻²)
N- Well Implant	Phosphorus	25	6.00E+12
P- Well Implant	Boron	20	3.00E+12
N+ S/D Implant	Phosphorus	35	5.00E+15
P+ S/D Implant	Boron	20	5.00E+15

are used for the simplified CMOS process, and the ninth mask defines the isolation trenches. Table 3 lists a final tenth mask, which is described in Section 2.2.2. This tenth mask creates the MEMS structures for a separate research project. Doping profiles were chosen to obtain high-voltage transistors (see Section 3.6.1). The process flow can be found in Figures 21a-j.

2.2.1.1 Ion Implantations, Gates, and Drive-In

For further background, the fundamentals of CMOS processing are outlined by Jaeger [28] and Wolfe [50]. For the Icarus process, we use an SOI wafer. Its 15 μm device layer is p-type and has a resistivity greater than 5 ohm-cm. The first mask, ALIGN, is strictly for alignments marks, which are used for the alignment of subsequent layers (Figure 21a). The next step is the application of the PMINUS mask which is used to selectively implant boron. This mask creates the p-well of the NMOS transistors. The implant power and dose levels are listed in Table 4. Likewise, the NMINUS mask is used to selectively implant phosphorus for the n-well of the PMOS transistors. In this simplified CMOS process, the concentrations of the n-well and p-well also set the threshold voltage of the depletion-mode transistors. To drive in the dopants, the wafers are heated to 1100 °C. The heat treatment involves a dry O₂ oxidation for 40 minutes, followed by 12 hours in an N₂ ambient at the same temperature (Figure 21b).

Afterwards, the thermal oxide is removed in HF and the silicon dioxide that will

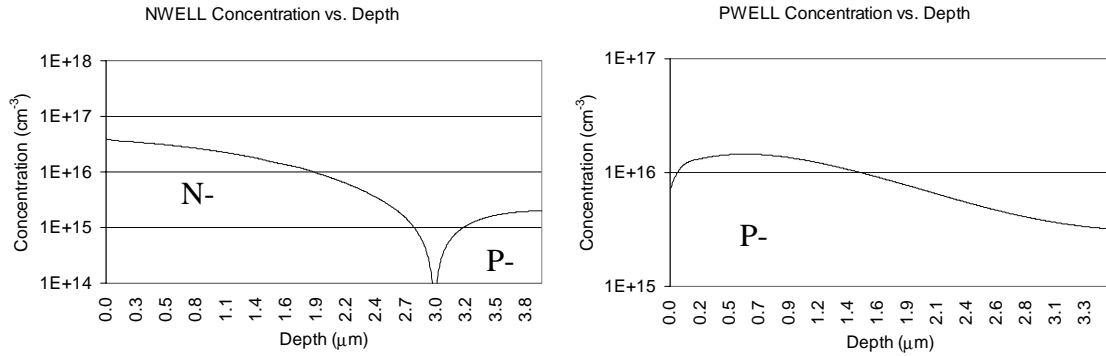


Fig. 19. Doping profiles for wells of transistors. a) NWELL Concentration vs. Depth. The NWELL depth is approximately 3.0 μm .

b) PWELL Concentration vs. Depth.

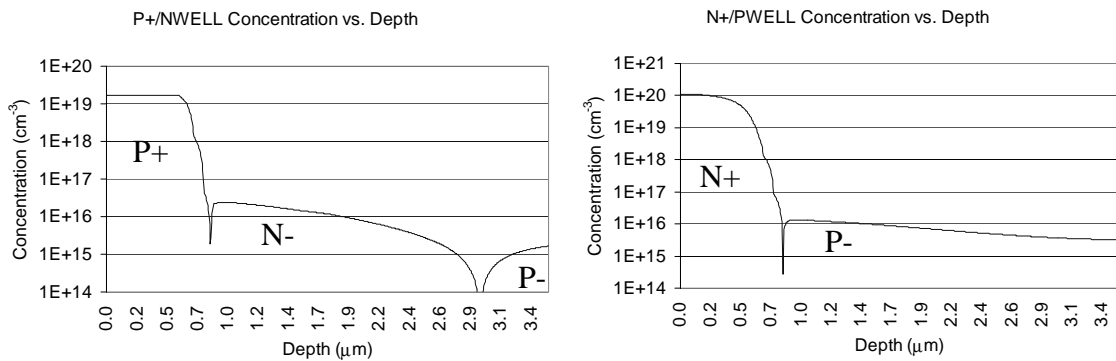


Fig. 20. Doping profiles for the source/drain regions of transistors. P+/NWELL concentration vs. depth. Source/drain junction is approximately 0.8 μm .

b) N+/PWELL concentration vs. depth. Source/drain junction is approximately 0.8 μm .

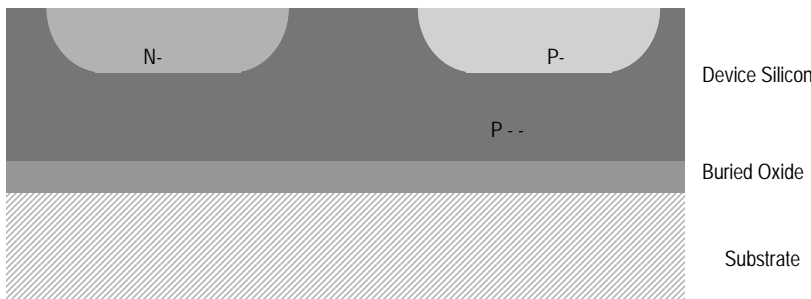
serve as the gates of the transistors is grown in a dry O_2 ambient at 1050 $^\circ\text{C}$ for 85 minutes, followed by a 60 minute N_2 anneal. The predicted results of the drive-in can be seen in TSuprem's modeled junction profile for both the phosphorus and boron species in Figures 19a and b. Junction depth of the n-well is approximately 3.0 μm . Immediately following the growth of the gate oxide, 0.55 μm of phosphorus-doped polysilicon is deposited using low-pressure chemical vapor deposition (LPCVD) at 610 $^\circ\text{C}$. The POLY mask is used to pattern the gates of the transistors. A reactive ion etch (RIE) removes the unwanted polysilicon (Figure 21c).

The P+ mask is used to define the pattern of the next ion implant step. The boron-doped implant defines the source and drain regions of the PMOS transistors. In addition

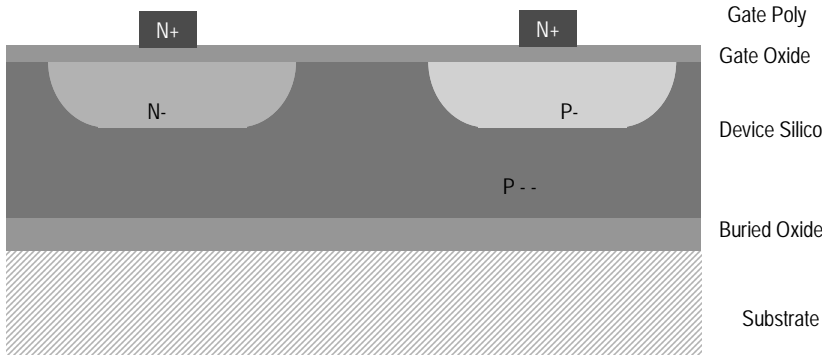
Icarus Process Flow



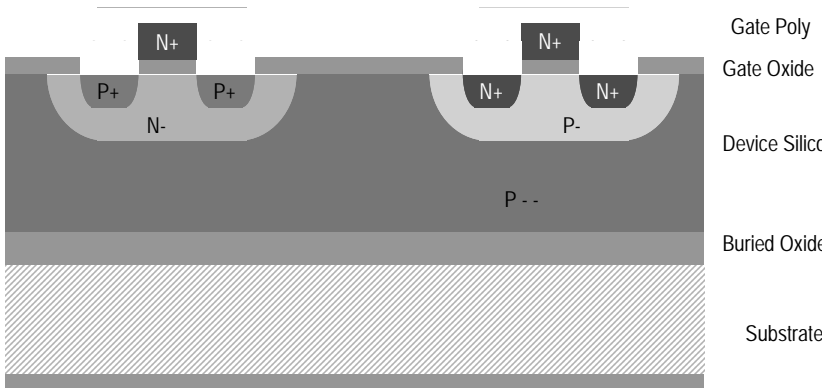
Fig. 21. Icarus process flow. a) Begins with 15µm device layer SOI wafer. The Align Mask is used to make alignment marks.



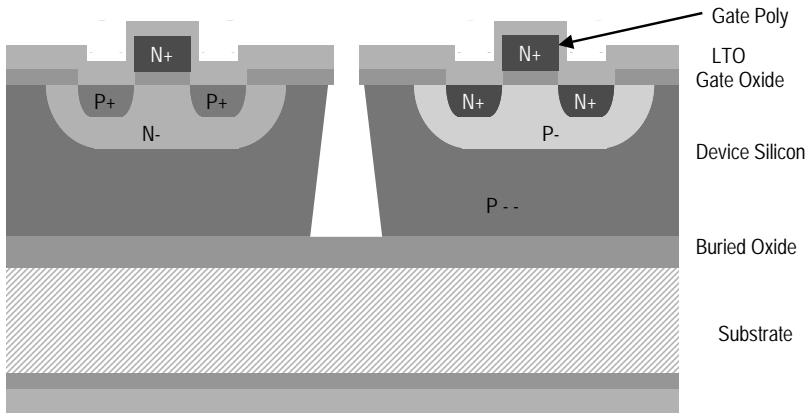
b) Ion implant both boron and phosphorus which define the wells of the transistors (NMINUS and PMINUS masks). Afterwards, drive-in the dopants at 1100 °C.



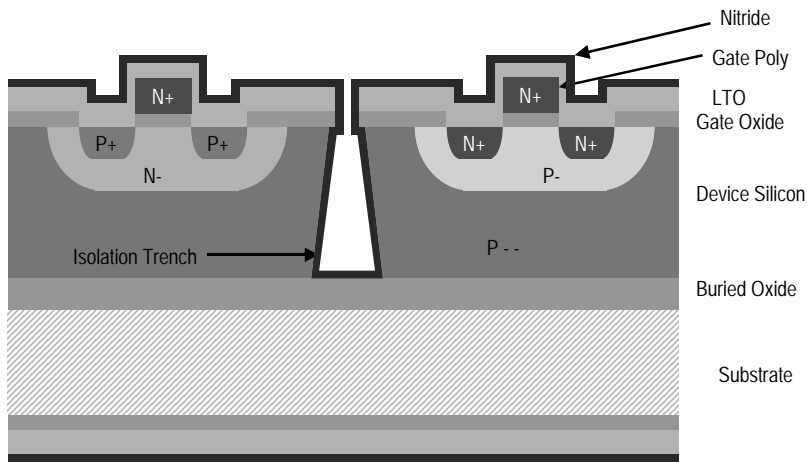
c) Grow 1000 Å of gate oxide at 1050 °C, then deposit phosphorus doped poly-Si for the gate. Pattern and etch gate poly-Si (POLY mask).



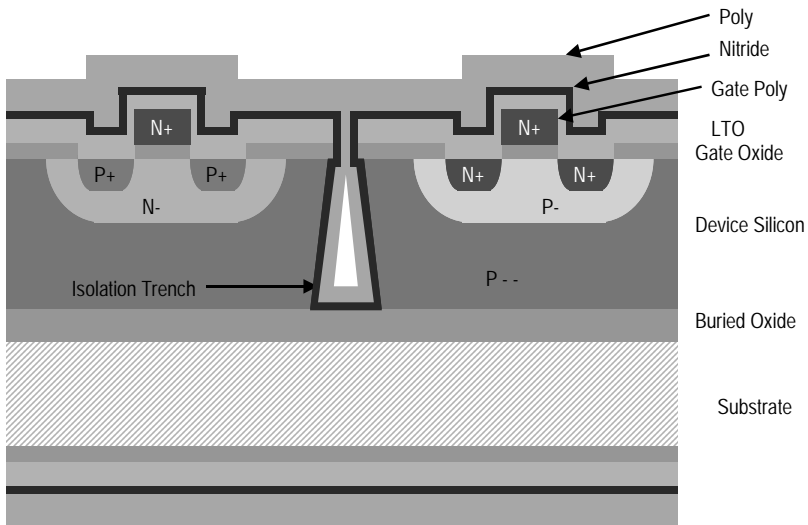
d) Perform a gate-aligned ion implant of both phosphorus and boron to define the source and drain of the transistors (NPLUS and PPLUS masks).



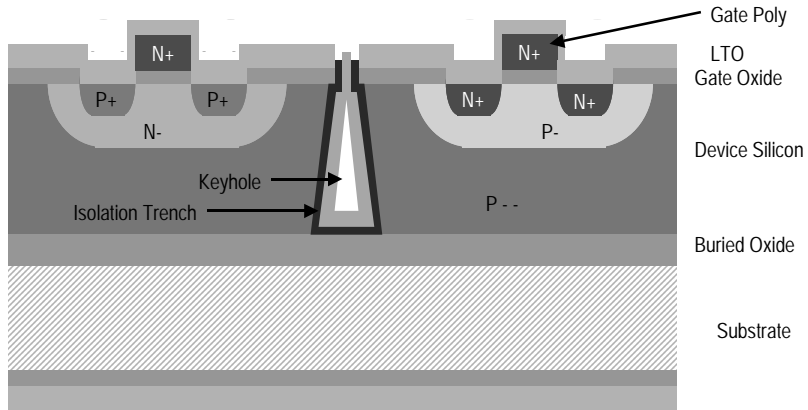
e) Deposit 0.6 μm of LTO. Etch high aspect ratio reentrant trench through the device layer using Bosch-process ASE etch. This etch defines the electrical isolation between solar cells and transistors (Iso mask).



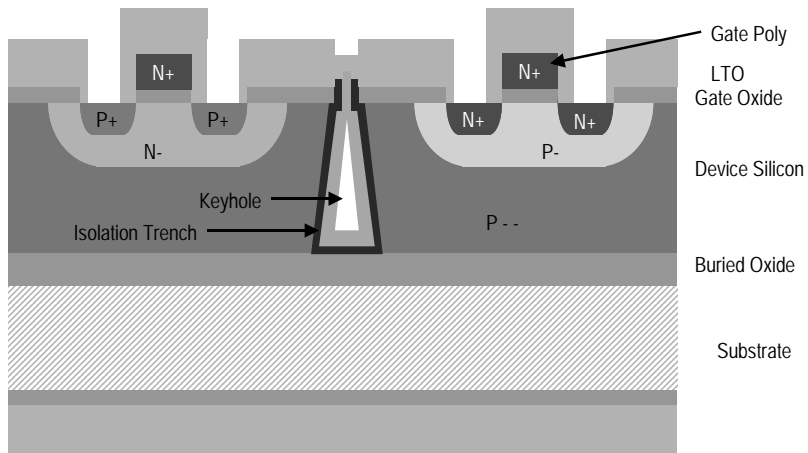
f) Deposit 0.2 μm of stoichiometric silicon nitride. Si_3Ni_4 is used as an inter-layer dielectric between blocks of device silicon.



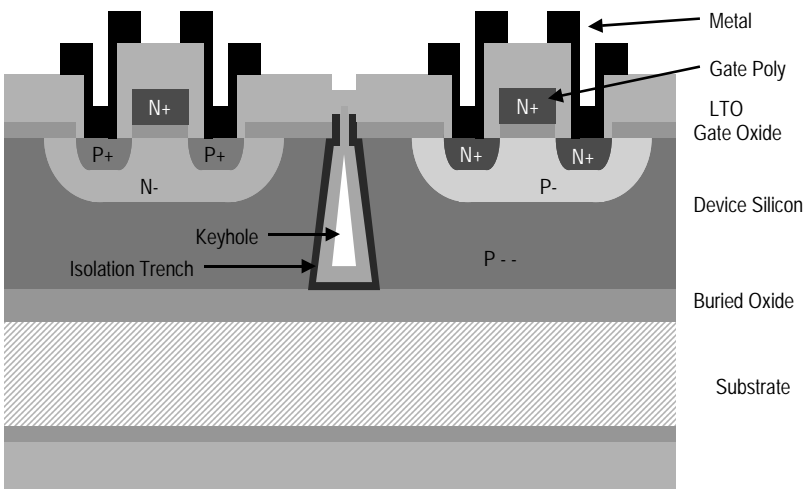
g) Deposit 3.5 μm of undoped poly-Si. The poly-Si is used to backfill the trenches with a lower stress and higher rate than silicon nitride.



h) Undoped poly-Si is etched back on the surface using DRIE. Poly-Si remains backfilled in the trenches. Surface nitride is removed in hot phosphoric acid.



i) A 1 μm LTO insulating layer is deposited. CONT mask defines contacts for the metal layer and is etched using a RIE oxide etch with a brief BHF dip.



j) Al + 2% Si is evaporated onto the wafer. Using photoresist as a mask (METAL mask), a wet etch removes the unwanted aluminum. A final anneal at 450 °C finishes the process.

to photoresist, the polysilicon gate acts as an implant mask to make gate-aligned transistors. With photoresist as a mask, a 5:1 buffered oxide etch (BOE) removes the 1000 Å gate oxide before implantation. Likewise, the N⁺ mask follows the same steps. This mask defines the area for the source and drain regions of the NMOS transistors. Again, implant doses and energies can be found in Table 4.

The last high-temperature step is the drive-in of the N⁺ and P⁺ dopants. This drive-in occurs in an O₂ ambient at 1000 °C for 20 minutes (Figure 21d). Lastly, a passivating layer of LPCVD low-temperature oxide (LTO) is deposited (6000 Å). The resulting predicted concentration profiles can be seen in Figures 20a and b. The N⁺ and P⁺ junctions both have a junction depth of approximately 0.8 μm.

2.2.1.2 Isolation and Refill

The previous section described the implants and thermal steps necessary for making simplified CMOS transistors. In this step, we deviate from standard CMOS processing and incorporate isolation between devices. Isolation trenches, originally proposed by Brosnihan [7], are high-aspect-ratio trenches in the device layer that electrically isolate devices. The trenches are back-filled with a passivating layer, and the wafer is subsequently planarized for further lithographic steps. Based on this technology, Bellew demonstrated 88 V from 200 series-connected solar cells.

In Bellew's solar cell work, the creation of isolation trenches was the first step in the process. In Icarus, however, isolation trenches are incorporated into the process after the high-temperature and ion implantation steps. This allows us to take advantage of existing CMOS foundry services and reduce the amount of in-house labor. Since the trenches are designed purely for physical isolation of the device layer, one can be flexible as to the order of the process. As an example, one could have a foundry partially fabricate

devices to the point right before making metal interconnect. If such a foundry process were economically feasible, this would allow for reliable, high-yield transistors to be made commercially, while the non-standard step, i.e., isolation trenches and refill process, could be processed in-house. Such “hybrid” processing would drastically reduce the amount of in-house labor from a 9-mask process with moderate yield to a high-yield commercial grade process with only three masks to be completed in-house.

For our purposes, we completed the entire process in-house. Creating trench isolation is a two-step procedure. With the Isolation Trench mask (ISO mask), an RIE oxide etch exposes the silicon by removing the LTO and gate oxide. The second step is a high-aspect-ratio advanced silicon etch (ASE) using the Bosch process. The etcher made by Surface Technology Systems (STS) can etch with aspect ratios as high as 25:1. Because of the depth and narrow width of the trenches, endpoint detection was not possible. To compensate, we etched to the buried oxide with a 50% overshoot (Figure 21e).

The trenches need to be backfilled and planarized before the metal layer is deposited. Backfilling the trenches is a four step-process. First, we deposited 2250 Å of stoichiometric silicon nitride at 800 °C (Figure 21f). With a breakdown field of 5 MV/cm, the nitride layer can tolerate voltage differences up to 100 V. For logistical reasons, stoichiometric nitride was deposited, but Bellew has shown that low-stress nitride is also adequate. Because of the low deposition rate and high stress of silicon nitride, polysilicon was used to fill the rest of the trench (Figure 21g). Approximately 3.5µm of undoped polysilicon was deposited with LPCVD at 600 °C.

We observed that in the backfill process, keyholes were formed within the trenches (see Figure 15). One concern with keyholes is that they can pierce the surface of the trench and cause trouble during subsequent metal deposition steps. Bellew described this

phenomenon in detail. He solved the problem by including key-hole reduction features. Without going into too much detail, these key-hole reduction features allow deposition to continue in the trenches even while the trenches are sealed off from the top. The keyholes, consequently, are reduced in size, and the risk of exposing trenches during the etch back step is reduced.

After backfilling the trenches, the deposited polysilicon on the backside of the wafer is removed to reduce stress. An RIE silicon etch with endpoint detection is performed to planarize the frontside. Optical endpoint detection is used to detect SiCl, a by-product of the etch. After the polysilicon is removed, the silicon nitride can peel off the surface but does not tear, forming small bubbles around areas of nonuniform topography. Specifically, edges around the polysilicon gates had nitride peeling up. It was not a big concern, however, because in the next and last step of trench isolation, backfill, and planarization, the surface silicon nitride is removed in hot phosphoric acid at 170°C (Figure 21h).

The process continues with depositing LTO on top of the planarized trenches in preparation for the contacts and metallization. Contacts in the oxide are patterned using RIE with the CONT mask. A brief 5:1 BOE dip removes back-sputtered oxide and guarantees that the oxide is fully removed (Figure 21i). Next, approximately 3000 Å of aluminum is evaporated onto the wafer (surface resistance 0.07 Ω/square). The aluminum contains 2% silicon to prevent junction spiking. The METAL mask is used to define the metal lines. With photoresist as the etch mask, an aluminum wet etch (phosphoric and acetic acids) selectively etches the aluminum. Afterwards, the aluminum is sintered at 400 °C for 15 minutes (Figure 21j).

To reduce the weight of the solar cell chip, the whole wafer is ground down from

Surface Contamination of Dopants

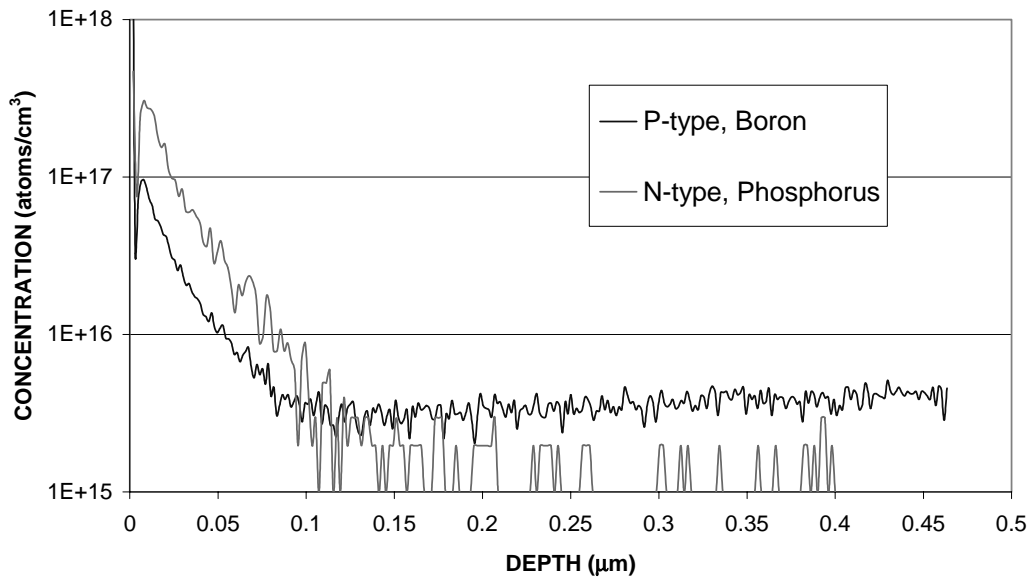


Fig. 22. Surface contamination of dopants. Both dopants were detected on the surface of a processed wafer. The nominally $5E15/cm^3$ boron-doped wafer had contamination of both types up to 1000 Å into the surface.

560 μm to 150 μm, reducing the weight of a chip by 250%. After the wafer has been ground, chips are diced up using a dicing saw.

2.2.1.3 Phosphorus Contamination and Transistor Rings

After the first fabrication run of the Icarus process, we characterized the transistors. The PMOS transistors operated normally. To our dismay, the NMOS devices showed significant drain-to-source leakage below the gate threshold voltage. With the help of Dimitry Kousminov from Accurel Systems, we used secondary ion mass spectroscopy (SIMS) to detect surface contaminants. We analyzed the concentration of phosphorus and boron at the silicon/oxide interface. The results are indicated in Figure 22. The sample area itself, did contain implanted species. However, we detected within the first 1000 Å of the silicon device layer, high concentrations of both boron and phosphorous. In addition, phosphorous exceeded the concentration of boron. This is akin to having a thin

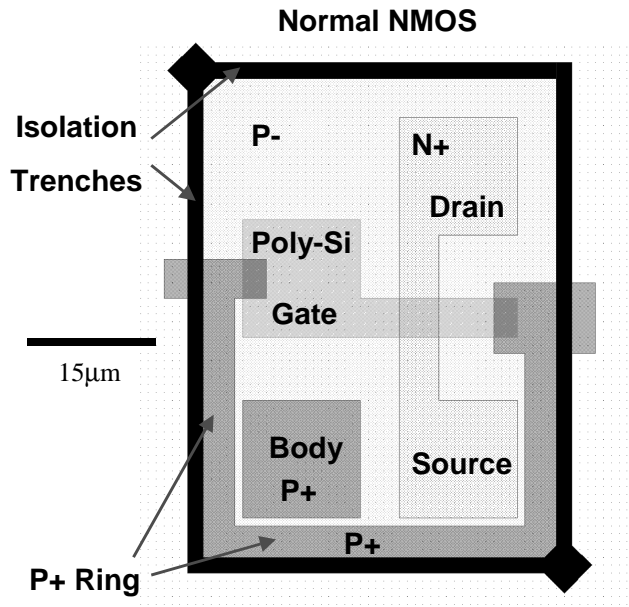


Fig. 23. P+ ring on NMOS transistor. The layout picture shows an NMOS transistor with an isolation trench surrounding the whole transistor and a P+ ring surrounding the source. The P+ ring was used to eliminate source to drain leakage from phosphorus surface contamination.

surface N-type layer throughout the wafer, which supported our findings that the NMOS transistors leaked, but the PMOS transistors operated normally.

We were never able to determine the exact cause of the contamination, but we did verify that it was a repeatable phenomenon. To circumvent the problem, we borrowed techniques from conventional CMOS processes. In these processes, a “P-TUB” or “channel stop” implant surrounds the transistor. This P+ ring reduces surface currents from one device to the other underneath the field oxide. With such a ring, NMOS devices can also be protected from drain-to-source leakage. We realized this design without altering the process by including a P+ ring in the PPLUS mask. Figure 23 shows a layout of a typical NMOS transistor. An isolation trench electrically isolates transistors from one another. Additionally the P+ ring surrounds the source of the device preventing drain-to-source leakage.

2.2.2 Solar Cells, CMOS, and MEMS

With the addition of just one more mask (WELLSTRUCT) to the Icarus process,

Process Flow Addendum for MEMS, Solar Cells, and High Voltage Devices

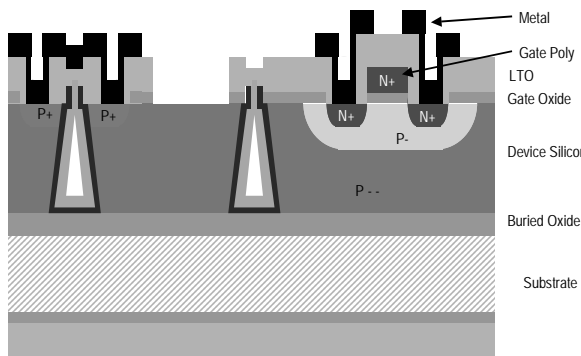
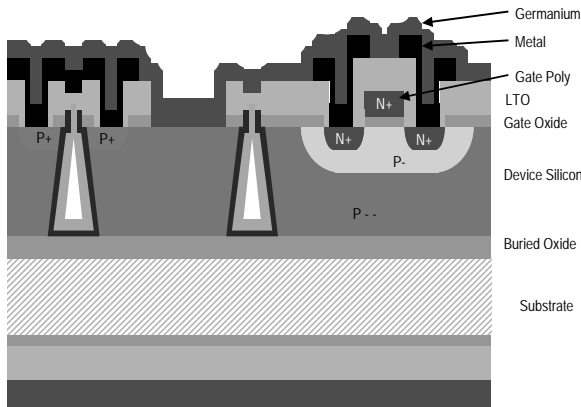
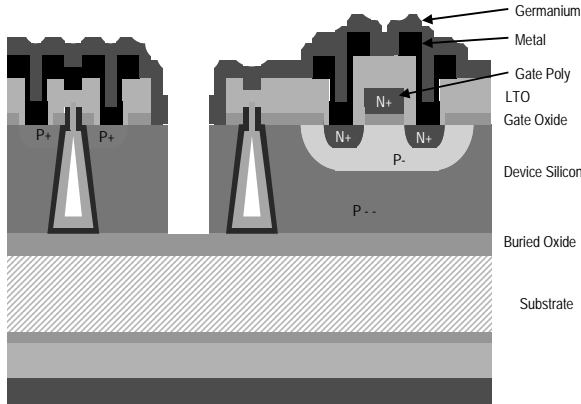


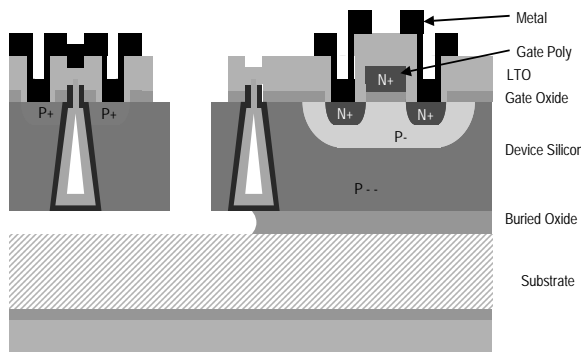
Fig. 24. Process flow addendum for MEMS. a) An oxide etch defines where MEMS structures will be patterned. (WELLSTR mask).



b) One micron germanium is deposited at 350 °C. Germanium can be etched using the Bosch process ASE etch and it is chemically resistance to HF. This makes germanium a protection layer for the electronic devices and metal wiring on the wafer.



c) A high aspect ratio Bosch process ASE etch is performed. This etch creates the MEMS structures in the process. Among the structures that can be made are electrostatic devices and thermal actuators.



d) Afterwards, the chips can be diced and individually released in a timed HF etch. After the buried oxide is selectively removed, the germanium is removed in hydrogen peroxide at 80 °C.

one can fabricate solar cells, CMOS electronics, and MEMS devices. The MEMS fabrication process is a single mask SOI process with trench isolation. However, the entire process forms the foundation for a fabrication methodology that would integrate all parts of a microrobot in a single monolithic chip. Bellew has demonstrated fully integrated MEMS devices with power in his process [6]. This section outlines the processing steps Bellew took to fabricate MEMS in the Icarus process.

As described in section 2.2.1, the solar cells and CMOS transistors are fabricated up to the point where the metal is evaporated (Figure 24a). Instead of using aluminum, Bellew evaporates titanium followed by titanium nitride (TiNi). TiNi is used as an interface layer to provide better adhesion to germanium, which is subsequently deposited using LPCVD at 350°C (Figure 24b). The germanium layer acts as an HF protection layer during the MEMS release later in the process.

Using the MEMS mask (WELLSTR), the wafer is patterned with photoresist. The device layer is then etched using a high aspect ratio ASE etch (Figure 24c). The ASE etch etches both germanium and silicon, so an additional etch step is not necessary. As Figure 21e suggests, the initial isolation trenches are not perfectly vertical. In performing the structure etch, it is important that the isolation trenches be reentrant (i.e. wider at the bottom than at the top). Brosnihan discovered that bands of silicon on the sidewalls of the isolation trenches can electrically short adjacent blocks of the SOI device layer [7]. Reentrant trenches expose the silicon during the MEMS etch, effectively eliminating the chance of electrical shorting.

The wafers are then diced into individual chips and the photoresist is removed. Using germanium as an HF barrier, the chips are placed in HF for a timed release to remove the buried oxide underneath freed structures. Lastly, the germanium is removed in

Table 5: Layer Names for Iolanthe Process

Lithographic Step	Description	Mask Name	Figure Reference
1	SOI Structures	WELLSTR	27a
2	First Poly-Si Layer	POLY1	27g
3	Anchors	CONT	27h
4	Second Poly-Si Layer	POLY2	27i
5	Backside removal	BACKSIDE	27j

hot hydrogen peroxide at 80 °C (Figure 24d). For the full details of the germanium HF protection layer the reader is referred to [6].

2.3 Planarized SOI and Polysilicon Micromachining - Iolanthe Process

The Icarus and National Semiconductor’s CMOS processes supply the power and brains of the robot, respectively. However, we needed a process to fabricate the legs and motors. Specifically, we wanted to incorporate electrostatic inchworm motors from SOI wafers with thin polysilicon hinges. As such, we designed a MEMS process that combines low-power, high-force actuators in SOI with hinged structures and linkages from traditional polysilicon micromachining. The process, dubbed Iolanthe¹, is based on a Gilbert and Sullivan operetta [44].

Iolanthe is a five-mask process whose layers are listed in Table 5. The process is detailed pictorially in the process flow in Figures 27a-h. We start with an SOI wafer whose substrate and device layers are doped type N+, and the device layer thickness is 45 μm (Figure 27a). The first mask, WELLSTR, defines the structures in the SOI device layer, most notably the inchworm motors. An ASE etch creates high-aspect-ratio (25:1)

1. The humorous operetta tells the story of a fairy, Iolanthe, whose son, Strephon, is half fairy and half mortal. Being half fairy, Strephon can perform all sorts of magical feats, but only halfway. For example, he can squeeze through a keyhole up to his waist, but his legs get stuck and are left kicking behind. In a similar vein, the robot has legs for mobility on its front end, but the rear end is left dragging itself.

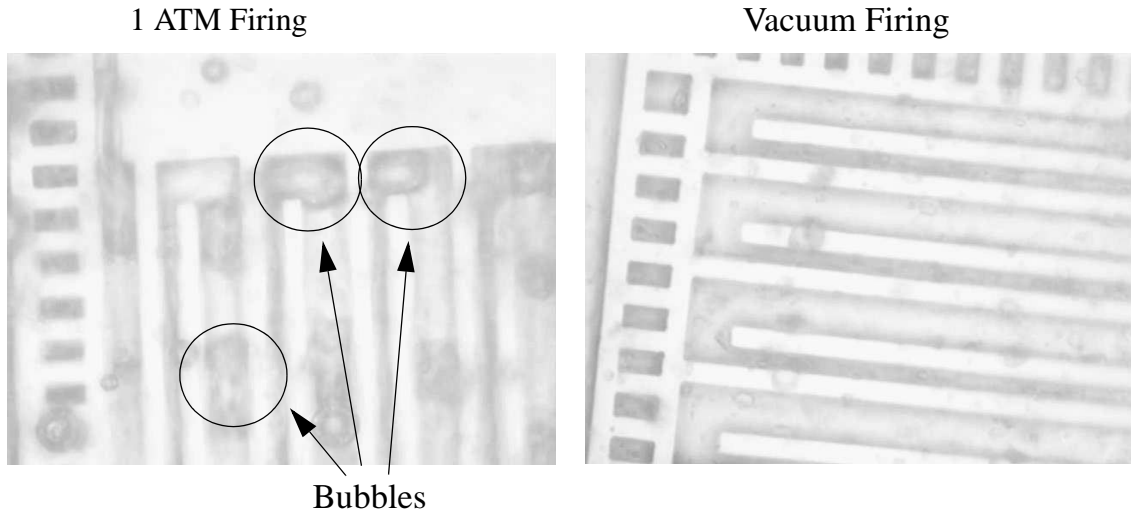


Fig. 25. Atmospheric firing vs. vacuum firing. a) The atmospheric firing of glass over 20 μm silicon trenches yields bubbles in narrow trenches. b) The vacuum firing of the glass yields fewer or no bubbles in narrow trenches.

structures with gaps as small as 1.5 μm (Figure 27b).

As described in Section 3.3.1, the high aspect ratio ASE etch contributes a small but finite lateral etch of the trenches in the SOI device layer. For reliable operation of the inchworm motors, however, we need to know the amount of lateral etch a priori. The ASE etch varies from wafer to wafer making it difficult to design to a particular lateral etch. To solve this problem, the wafers subsequently undergo a wet oxidation to consume the silicon sidewalls to a predetermined value. This allows us to tailor the total lateral etch even though the ASE's lateral etch varies. In this case, the ASE etch and subsequent oxidation step result in a total lateral etch in the device layer of 0.5 μm .

2.3.1 Thick Glass Film Technology

A key challenge of the process is adding structural polysilicon after the primary SOI etch. This is accomplished using Yasseen's thick glass planarization technology [53]. For the creation of the robot, we have extended the capabilities of this technology in numerous ways. Whereas Yasseen had demonstrated planarization of polysilicon structures up to 15 μm high, we demonstrate planarization of an SOI device layer that is 45 μm

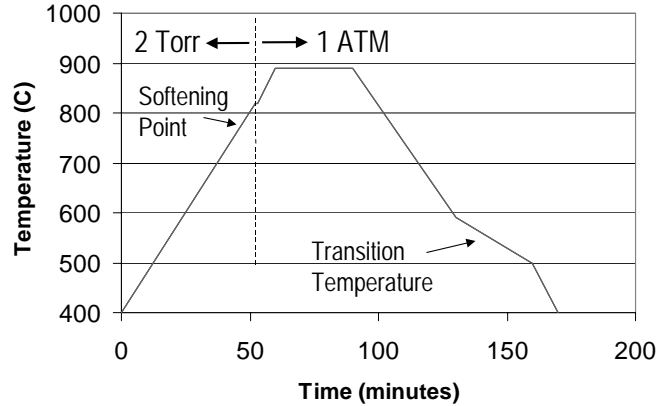


Fig. 26. Firing profile of glass. The glass was heated in an oxygen ambient at 2 Torr to allow the glass to flow into deep trenches. Any remaining bubbles were then minimized during the pressurization stage from 2 Torr to 1 ATM.

thick. Furthermore, we actively micromachine the planarized surface creating polysilicon structures on top of the glass.

Following Yasseen’s protocol, we spin on a glass slurry (Figure 27c), burn out the organic (Figure 27d), and reflow the glass at 890 °C, where the frit coalesces to form a single glass network (Figure 27e). We use a 14:10 ratio by weight of alpha terpineol to glass frit. The slurry is sonified at 20 kHz for 10 minutes to break up the frit agglomerates (Branson Digital Sonifier). Then, the slurry is spun on the wafer for 30 seconds at 500 rpm. The wafer is fired in a low pressure furnace to minimize the occurrence of bubbles (~2 Torr). Figures 25a and b exemplify the difference between glass firings in atmosphere versus low pressure. In atmospheric firings, air at the bottom of trenches becomes trapped during the reflow step and creates bubbles. Additionally, we found that simply firing in low pressure did not completely remove bubbles. As a deviation from [53], we heated the glass to just below the firing temperature in an oxygen ambient at 2 Torr to allow the glass to flow into deep trenches. Any remaining bubbles were then minimized when the chamber was pressurized from 2 Torr to 1 ATM. The firing profile is shown in Figure 26.

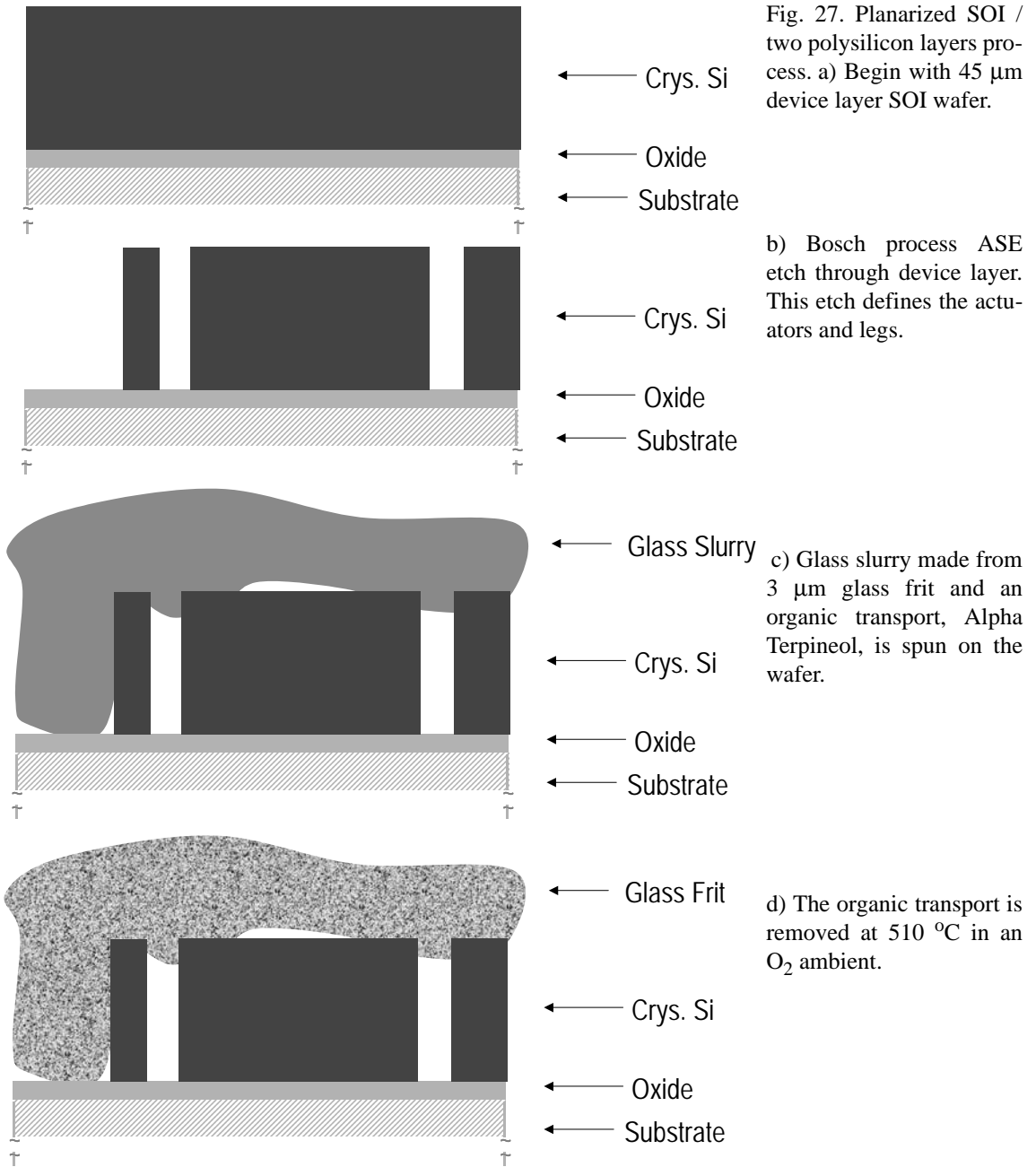
Because we did not have equipment to fire the glass in a vacuum furnace, we

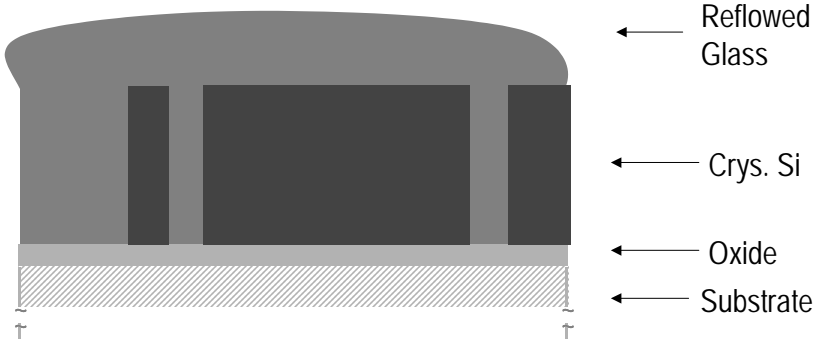
pieced together a make-shift furnace. The furnace is composed of a quartz belljar inside a high temperature Lindberg oven (Figure 28). Tubing for gases and vacuum were piped in through the exhaust at the top of the oven. A vacuum seal was created by placing the quartz belljar on top of a quartz plate. While this seal only maintained vacuums of 2-3 Torr, the vacuum furnace allowed us to run various firing profiles. Additionally, Chris Keller from MEMS Precision Instruments constructed a cold-walled furnace in which vacuums on the order of 100 millitorr could be obtained. To planarize, the glass is chemically mechanically polished (CMP) to the SOI/glass interface (Figure 27f) using a standard KOH slurry.

Yasseen reported on glass planarization of surfaces with thicknesses up to 15 μm [53]. Through repeated applications of the thick glass technology (i.e., spin-on slurry, fire glass, and CMP), we can planarize surfaces with topographies much greater than the 15 μm . While one application of our glass slurry yields final thicknesses of 25 μm , we have demonstrated planarization of device layers with thicknesses up to 50 μm .

In the next step, wafers undergo oxide and polysilicon depositions. Because the wafer is planarized, fine-line lithography can be used (2 μm). Three masks define the two structural polysilicon layers. First, 0.6 μm of phospho-silicate glass (PSG) is deposited at 450 $^{\circ}\text{C}$ using LPCVD. This is followed by a 2 μm thick layer of undoped polysilicon at 600 $^{\circ}\text{C}$. The polysilicon is patterned with the POLY1 mask and etched using the same Bosch process ASE etch (Figure 27g). After another layer of PSG is deposited (1.0 μm), the wafer is patterned with a contact mask, CONT, used for anchoring the polysilicon contacts to the device layer. An RIE silicon dioxide etch is used to cut the contacts (Figure 27h). Next, 2.5 μm of the second and final polysilicon layer is deposited. Again, the polysilicon is patterned with the POLY2 mask with the ASE etch (Figure 27i). A last 2.0 μm

Iolanthe Process Flow

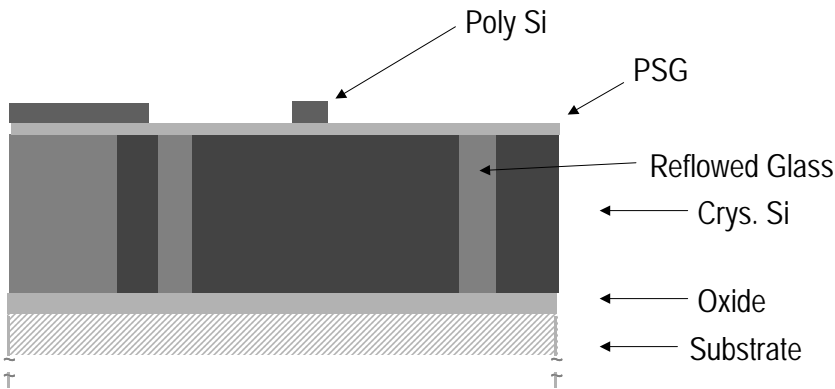




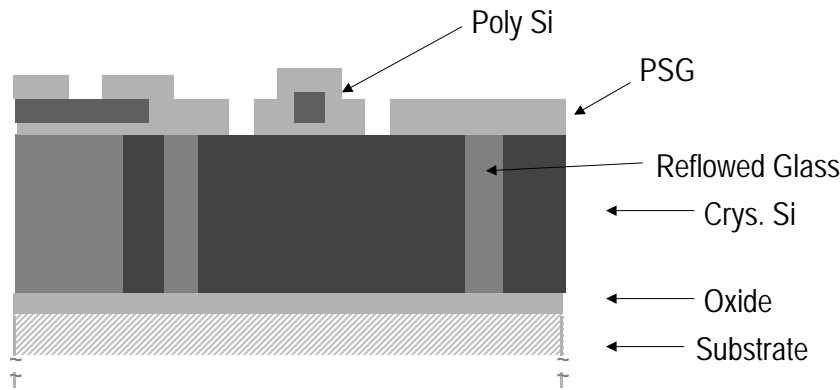
e) The glass frit is then reflowed at 890 °C to form a single glass network. Bubbles are reduced by doing a combination vacuum/atmospheric glass firing.



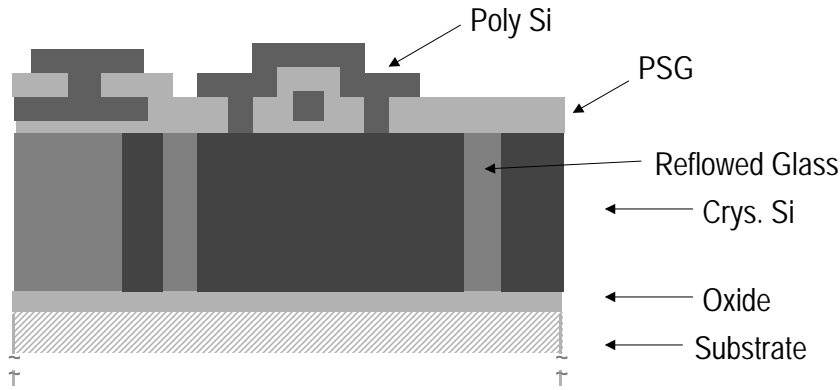
f) A KOH-based slurry is then used to planarize the wafer. Often a single layer of glass slurry only adds ~25 μm of glass. For thick device layers, steps (c) thru (e) should be repeated.



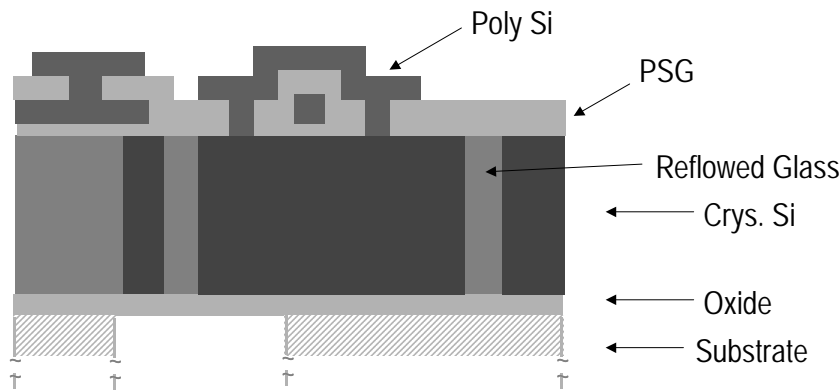
g) After planarization, the wafer can be surface micromachined. A 0.5 μm PSG layer is initially deposited followed by 2.5 μm of undoped poly-Si. The poly-Si layer is then patterned using DRIE.



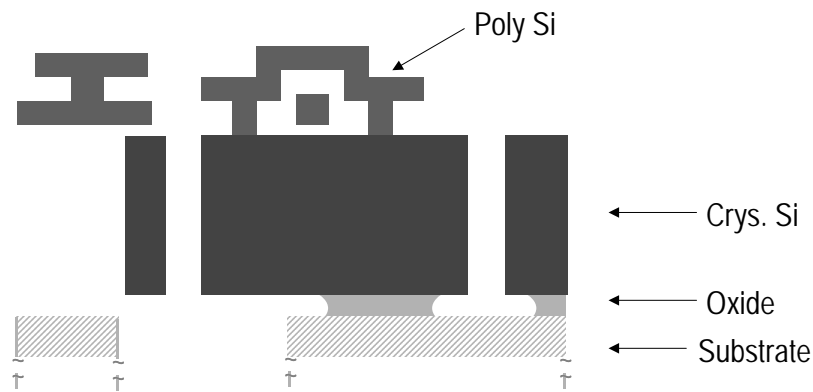
h) A 1.5 μm layer of PSG is then deposited. Careful calculation of layer thickness was performed to allow pin hinges to rotate freely in their pockets. The first and only contact etch is then performed.



i) A 1.5 μm layer of undoped poly-Si is deposited and patterned. The wafer is then annealed at 900 C for 1 hour to dope the poly-Si from the PSG.



j) The wafer is then backside ground to 300 μm total thickness. A backside etch completes the process. Backside exposure helps reduce the total weight of the robot. Additionally, debris and stiction issues are also reduced in the areas where the backside is removed.



k) The backside also defines scribing lanes. The wafer is then broken up into chips and individual chips are released. A timed HF/HCl/H₂O etch removes the glass. A final HF timed etch selectively removes the buried oxide.

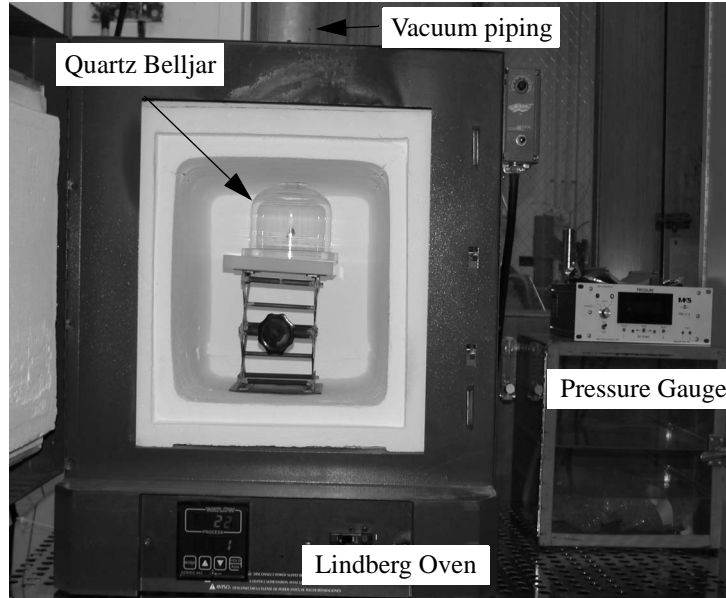


Fig. 28. Belljar furnace. The belljar furnace was made using a Lindberg box oven with a quartz belljar inside. The belljar formed an air tight seal with a quartz plate. N_2 , O_2 , and vacuum lines were fed from the exhaust hole through the top of the oven.

PSG deposition encapsulates the polysilicon and protects the surface in preparation for a backside grind. The backside is ground down from a total wafer thickness of $550\ \mu\text{m}$ to a final thickness of $300\ \mu\text{m}$. Since a few microns are removed from the device layer during planarization, the final substrate thickness is approximately $260\ \mu\text{m}$.

The wafers are then annealed for one hour at $900\ ^\circ\text{C}$ in order to reduce stress and drive-in phosphorus from the PSG to the polysilicon. However, we found large variability in the conductance of the POLY2 layer to the device layer anchor between the two fabrication runs of Iolanthe. In the last fabrication run, we needed to anneal the wafers at $1000\ ^\circ\text{C}$ for one hour to achieve similar conductances. That anneal was done after processing with individual chips. One reason may be due to native oxide growth right before the wafers go through LPCVD for the second polysilicon layer (POLY2). The native oxide can act as a diffusion barrier at low temperatures ultimately reducing the conductivity of the polysilicon.

The last mask, BACKSIDE, is aligned to the frontside via a Karl Suss backside mask aligner. Because of the wafer's thinness and residual stress, one can visually see the warping of the wafer. Some difficulty was encountered in affixing the wafer to the chuck of the aligner. A backside substrate etch is performed using the Bosch ASE process (Figure 27j).

The backside etch yields several advantages over the original inchworm motor process and for the robot in general. Removing the substrate underneath movable structures in the inchworm motors prevents substrate stiction and reduces the chance that particulate matter would get stuck between the gap closing actuators. Additionally, backside removal provides a lightened skeletal frame, which reduces the amount of force required from the motors. By introducing dicing lanes into the BACKSIDE mask, chips can be "diced" in the etch. Afterwards, the chips are held together by only the thin device layer (~40 μm) and can be manually separated with tweezers.

2.3.2 Structure Release

For the release, a solution of HCl, HF and H₂O (32:5:63) is used in a timed etch on the planarized glass, buried thermal oxide, and PSG. The goal is to provide a long enough etch to remove the PSG and reflowed glass, but not so long as to remove all of the buried oxide. The reflowed glass etches approximately 30 times faster than the buried oxide so that tight tolerances in the undercut of the thermal oxide are maintained. Narrow SOI blocks, therefore, are fully undercut while wide SOI blocks remain anchored to the substrate via the thermal oxide (Figure 27k).

An unfortunate by-product of the release is the appearance of alumina particles scattered across the wafer. Since the glass frit was created at Ferro Corporation using an

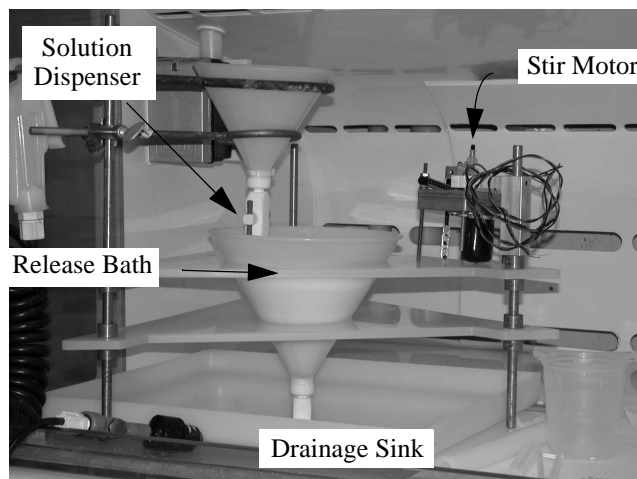


Fig. 29. Release station. The release station is used to hold the chips during the wet etch and final release of the devices. A teflon release holder is used for easy transport from release station to critical-point-dryer. Designed and built by Anita Flynn.

alumina ball mill for an extended period of time, alumina flakes with diameters on the order of $0.5 \mu\text{m}$ are present in the glass mixture. To remove the alumina particles, the devices are placed in a heated bath ($80 \text{ }^\circ\text{C}$) of NH_4OH , H_2O_2 , and H_2O (1:1:3). Critical-point drying is performed to avoid damage from water surface tension.

The structural release involves a number of solution etches and rinse steps and can often take 5 hours or more from start to finish. To reduce the physical labor and time, Anita Flynn designed and built a custom release station to hold the chips during the wet etch and final release of the devices (Figure 29). The release station is modeled after Srinivasan's original SAM release station reported in [43]. It includes a valve for pouring solution into a bath, adjustable valve to remove solution, a motor for stirring, and a teflon chip holder for easy transport from the release station to the critical-point dryer.

The release of the chips is not a straight forward endeavor. Anita Flynn, however, deserves most of the credit for finding and establishing a feasible structural release protocol. We encountered two major issues during the release step: 1) particulate contamination and 2) broken polysilicon structures. When we released robots right side up, a large

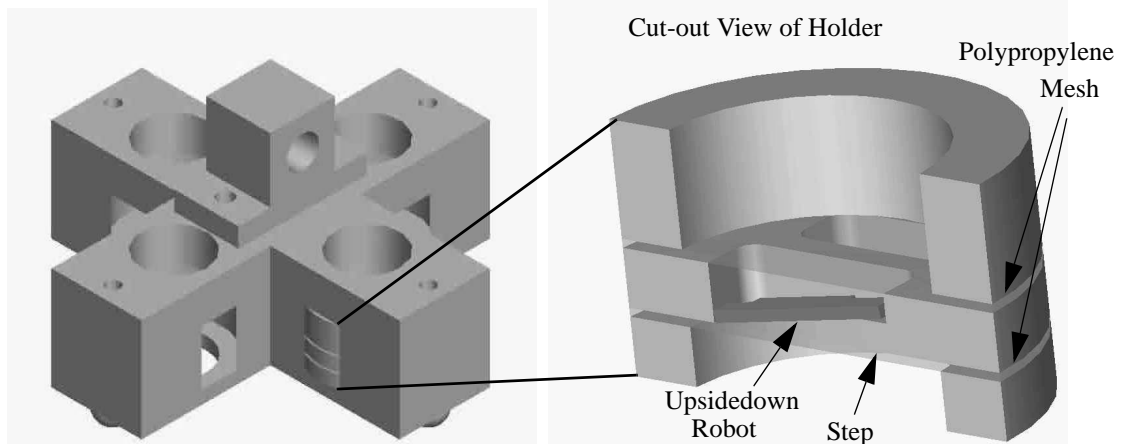


Fig. 30. SolidWorks drawings of release holder. The teflon holder is designed to hold the robots upside down while the delicate structures on the front surface are not damaged by the surface they are lying on. This is accomplished by supporting the tail end of the robot on a raised surface such that the robot lies at an angle. Four robots at a time can be released with this holder. Designed and built by Anita Flynn.

number of particulates were found in the trenches. In addition to being mechanical barriers, these particulates electrically shorted actuators to ground. Since gap-closing actuators operate with no DC current, a key metric to determine the cleanliness of the release was based on the I-V curve of the electrostatic actuator. If no contaminants shorted out devices, the actuators would operate at less than 1 nA of current for voltages exceeding 50 V. Some initial releases, however, showed leakage currents up to 20 mA.

Using Seiko's 8800 FIB System with energy dispersive x-ray analysis, we identified the chemical make-up of some of the particulates. We identified particles composed of aluminum, phosphorus, calcium, and silicon. It was unclear where the particulates came from, though. One possibility is from the release setup and critical-point dry, and another possibility is when the glass is first reflowed. We found that rigorous cleaning of the dishes used in the release and developing a disciplined attitude towards release protocol are mandatory to achieve cleanliness. Performing the release with the chips upside-down, furthermore, dramatically decreases the particulates. Electrical tests verified the cleanliness with less than 1 nA leakage currents. Lastly, agitation during the glass solu-

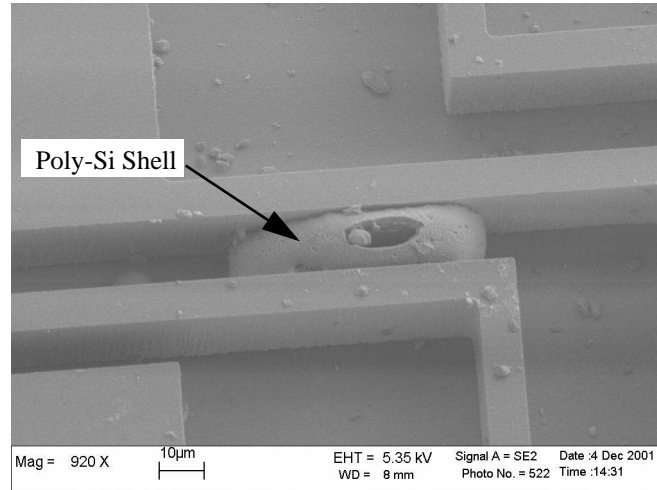


Fig. 31. Poly-Si shell from exposed bubble. After planarization and deposition, the poly-Si formed within the bubbles and remained after release.

tion etch further removes particles.

The robots themselves are released as separate $3 \times 8 \text{ mm}^2$ die. Releasing robots upside down while protecting delicate polysilicon structures proved challenging. Our solution is shown in Figure 30, the chip release holder. The CAD drawings display the release holder with the robot inside. The robot is placed upsidedown to remove particulates. Additionally, a raised step in the holder slightly tilts the robot so that the robot rests on the ends instead of on its face. The polysilicon structures which lie on the front of the robot can therefore never come in contact with the surface and break. Polypropylene meshes surrounding the robot on the top and bottom encourage solution flow and prevent the robot from flipping over.

2.3.3 Bubbles and Pb Diffusion

For the glass planarization step, reducing bubble formation is important in designing and fabricating reliable mechanical structures. Key factors that affect bubble formation are 1) pressure, 2) thickness of the SOI device layer, and 3) temperature. While lower pressures help eliminate bubbles in narrow trenches, more bubbles tend to form in larger

more open areas. Additionally, thicker applications of the glass frit create bubbles with larger diameters. Bubble diameters as large as the glass thickness have been observed. Lastly, temperature can have a significant affect. While we did most of our experiments at maximum firing temperatures of 890 °C, we noticed that firings up to 1000 °C would reduce the number and size of bubbles in the reflowed glass. We also looked at the tendency for the glass to adhere to different surface materials. While the glass did not adhere well to silicon or silicon dioxide, Keller found that the glass adhered well to alumina [30]. In the glass reflow experiments, some bubbles were always present after firing. Bubbles that are exposed after planarization can affect lithography and introduce unwanted polysilicon debris. Especially if bubbles form in narrow trenches, subsequent polysilicon depositions can fill open bubbles much like plastic injection molding. Once the glass is removed, the polysilicon shell remains. As an example, Figure 31 shows a polysilicon shell that has formed between two device layer beams. Ideally, the planarization process would have no bubbles. Still, the existing frequency and size of the bubbles are tolerable and do not significantly reduce the performance or yield of the fabricated devices.

The glass frit, itself, is one of Ferro Corporation's passivation glasses. IP900-VWG has a very low alkali metal content (> 50 ppm) and is composed of 50% SiO_2 , 30% PbO , 12% B_2O_3 , and 8% Al_2O_3 by weight. The powder size is 3 μm . One might be concerned that Pb could easily contaminate the quartz LPCVD tubes during silicon and oxide depositions. However, unlike the piezoelectric material PZT, whose high diffusivity at low temperatures is based on dislocations in the crystal lattice, IP900-VWG is an amorphous structure whose Pb atoms are surrounded by an average of six Si atoms. Pb diffusion does not become appreciable below the softening point, 771 °C. To demonstrate this point, we performed a SIMS analysis on the Si-Pb glass. Figure 32 shows the concentra-

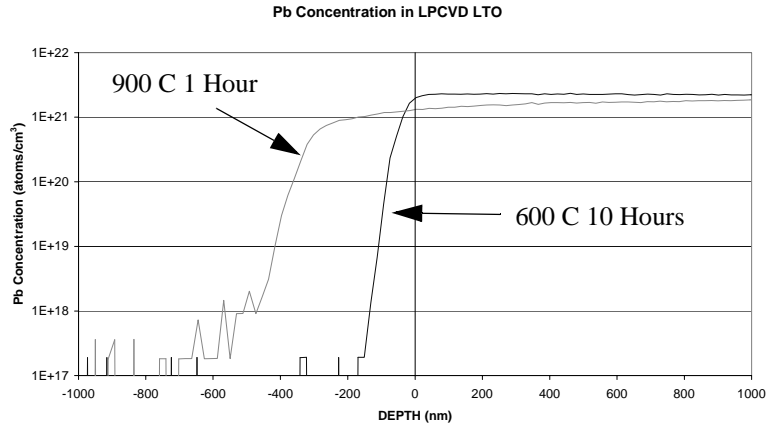


Fig. 32. Lead diffusion into LPCVD LTO. Secondary Ion Mass Spectroscopy (SIMS) was used to determine the concentration of lead in LTO and the glass.

tion of Pb at the interface of LTO and the glass. Wafers were tested at two stages in the Iolanthe process, once during a polysilicon deposition and another at 900 °C during the anneal. For the former, Pb diffused less than 50 nm into unannealed LTO after 10 hours at 610 °C. After one hour at 900 °C, Pb only diffused approximately 400 nm. Depositing LTO over the glass before further processing ensured negligible out-diffusion of Pb in subsequent steps.

2.4 Three-Chip Hybrid Assembly

After processing, three chips are assembled and wire bonded together to form the robot: 1) the CMOS controller chip fabricated by National Semiconductor Corp., 2) the solar cell chip from the Icarus process, and 3) the robot frame from Iolanthe. Because the robot needs to be free to walk, we use assembly methods that do not require permanently fixing the chips to die packages, as is done in traditional wirebonding processes. The assembly sequence follows the three basic steps outlined in Figure 33.

In the first step, the solar cell chip and sequencer are initially bonded to a handle wafer using Crystalbond mounting wax at 90° C. Once it returns to room temperature, the wax forms a solid bond to the chips. Then the chips are wirebonded together (11 wireb-

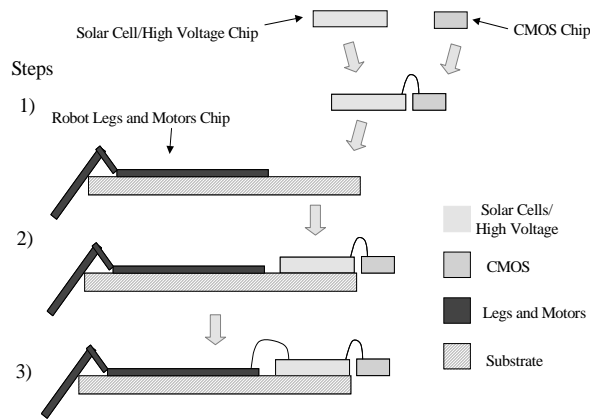


Fig. 33. Robot assembly in three steps. 1) Solar cell chip and sequencer are wire bonded together, 2) Solar cell chip is bonded to robot chip with hot wax. 3) Robot and solar cell chip are bonded together.

onds) using a Westbond ultrasonic bonder with aluminum wire. After wirebonding, the two chips are subsequently removed from their handle wafer by either 1) heating the wax or 2) dissolving the wax in acetone. Care must be taken when dissolving the wax in acetone. Because the METAL layer on Icarus does not have a passivation layer on top, aluminum wires can easily peel up if the chip is allowed to air dry. We verify functionality of the two-chip combination before proceeding to the next step.

The next step entails bonding the robot chip to a handle wafer with Crystallbond wax similar to the previous step. This step is a bit more critical because the robot is only 300 μm thick and already released. Care is taken to prevent the melted wax from wicking up the sidewalls and possibly breaking hinges. Once the robot is firmly held to its handle wafer, wax or epoxy is used to attach the previously wirebonded chips onto the back end of the robot.

Lastly, we wirebond the high-voltage buffers to the robot (9 wirebonds). To release the robot, we dip the handle wafer in acetone which dissolves the wax. Afterwards, we rinse the completed robot in methanol and allow it to air dry. We did not perform another critical-point dry. We have not seen any thin polysilicon structures break.

Surprisingly enough, though, we have witnessed serpentine springs from the thicker SOI device layer break due to surface tension forces in the methanol.

Chapter 3. Analysis

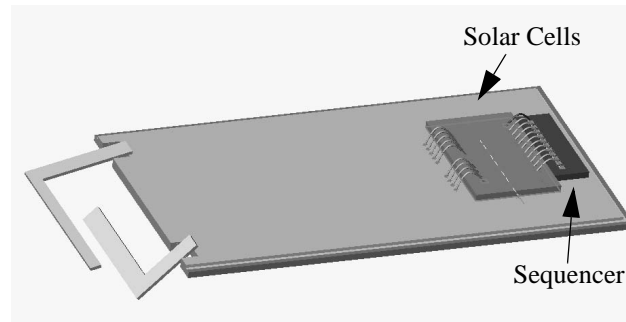


Fig. 34. Improved concept of robot. Two one-DOF legs carry the robot in a forward walk while solar cells and sequencer rest in the back.

In the previous chapter, we discussed the in-house fabrication processes for making the robot. The Iolanthe process is used to fabricate the robot's frame, motors, and legs. The Icarus process provides the solar cells and high-voltage transistors to power the robot. In this chapter, we detail the analyses that were completed to design and manufacture the robot. We begin with a description of the expected robot walking sequence in Section 3.1. In Section 3.2, a generic robot force model is presented. Using the two-legged prototype robot as an example (Figure 34), the model allows us to estimate the size of the motors needed to drive an autonomous robot.

Sections 3.3 through 3.5 discuss the analyses for the Iolanthe chip. Section 3.3 analyzes design strategies for inchworm motors. For high performance electrostatic motors, beam spacings are designed at the limiting resolution of the process. At this dimension, we try to understand the effect the lateral etch in the device layer has on the motor's operation. Next, we discuss reversible inchworm motor operation and its impact on the output force. In Section 3.4, basic mechanical modules which form the out-of-plane building blocks of the Iolanthe process are presented. In Section 3.5, hinges and sliders are combined to create a slider-crank linkage translating the linear motion of the inchworm motor to out-of-plane rotation of the legs. Furthermore, to demonstrate the

design flexibility of the Iolanthe process, a two-DOF robot leg is presented.

Section 3.6 of this chapter discusses the analyses for the Icarus chip. Due to the electrical passivation of isolation trenches on SOI, solar cells can be stacked in series to create a high voltage power supply. Furthermore, we discuss breakdown mechanisms of the transistors, including optimized doping profiles and geometries for higher operating voltages. With such devices, we present a simple cross-coupled inverting buffer which converts the low voltage digital signals from the sequencer to the 50 V needed to drive the actuators.

In last portion of the chapter, Section 3.7, the robot controller is discussed. The controller is a simple open-loop sequencer that drives the motors, creating the walking gait of the robot. The basic modules of the open-loop sequencer are presented including the current-starved oscillator and sequencing logic.

3.1 *Walking Sequence*

Our design of the robot had two goals. First, the robot should demonstrate a possible walking system. Secondly, we aimed to establish a framework and fabrication flow from which more complicated robots could be built with minor design changes. Probably, the simplest walking robot is a two-legged design, in which each leg has one DOF. Figure 34 shows the initial concept of the robot. The robot is composed of a long and short leg. The Iolanthe chip makes up the frame and motors of the robot while the CMOS and Icarus chips are located in the back. While the robot has a very simple design, it demonstrates a number of capabilities of the processes that will be discussed later in the chapter.

To enable walking, two, one-DOF legs are used to move the robot forward. The short leg acts as the horizontal actuator, pulling the robot forward, and the long leg acts as

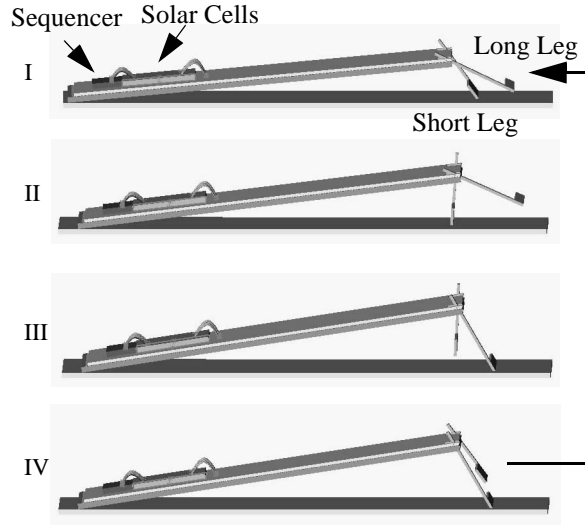


Fig. 35. Leg sequence for walking robot. I) Short leg rests on ground. II) Short leg actuates and pulls robot forward. III) Long leg actuates, lifting short leg off ground. IV) Short leg retracts to nominal position. Long leg then retracts bringing the cycle back to phase I.

the vertical actuator, allowing the shorter leg to reset at the end of each cycle. As illustrated in Figure 35, the legs go through four steps to complete a single forward cycle. At phase I, the robot rests with just its short leg touching the ground. In phase II, the short leg actuates through 30° of motion, pulling the robot forward by $230\ \mu\text{m}$. In phase III, the long leg actuates, lifting the short leg from the ground. In phase IV, the short leg, no longer on the ground, retracts to the nominal position. Finally, the cycle repeats itself when the long leg retracts, bringing the sequence back to phase I. Ideally, the overall forward progress per stride would be $97\ \mu\text{m}$, as the robot would move backwards $133\ \mu\text{m}$ in phase IV.

3.2 Robot Motor Design Approach

In designing our robot, we confined ourselves to first-order estimates of power, mass, and force. Our main concern was the generation of enough force to overcome the weight of the robot. Inchworm motors were chosen because they are extremely efficient and exhibit large force with large displacement. The inchworm motor consists of a shuttle

which is “inched” along by two clutches, each driven by a clutch-drive pair of GCA arrays (see Section 1.2) [57]. Equation (2) in Chapter 1 relates the force density to parameters of the array and is presented here, again:

$$\sigma_{\text{GCA}} = \frac{F_e}{A_{\text{GCA}}} = \frac{\epsilon_0 V^2 N t (g_f^{-2} - g_b^{-2})}{2(2d + g_f + g_b)} \quad (5)$$

where

N is the number of GCAs in the array
 V is the voltage applied across the GCA fingers
 ϵ_0 is the permittivity of air
 t is the actuator thickness (i.e the thickness of the SOI device layer in the process used here)
 d is the width of a GCA finger
 g_f is the initial gap distance over which the actuator will close when voltage is applied
 g_b is the initial gap distance, on the other side of the moveable beam, to the next GCA in the array

Because an inchworm motor is composed of four GCA arrays, along with interconnects, bondpads, etc., the fill factor, FF, must be considered when sizing the inchworm motors for adequately lifting the robot. FF is the ratio of a GCA’s active area to the inchworm motor’s total area. The actual force per unit area of an inchworm motor, σ_m , can then be calculated as:

$$\sigma_m = \sigma_{\text{GCA}} \text{FF} \quad (6)$$

Yeh reported a fill factor of 11% for his inchworm motors, and we used that number for our leg motor designs. To size the motors, we needed to relate the force per unit area of the inchworm motors to the mass of the robot. The mass of the robot can be described as the sum of the masses of the three individual chips. Consequently, the mass of the robot is:

$$M_{\text{robot}} = \rho_{\text{si}} (\alpha_m A_m t_m + A_{\text{sc}} t_{\text{sc}} + A_{\text{cmos}} t_{\text{cmos}}) \quad (7)$$

where

M_{robot} is the mass of the robot
 ρ_{si} is the density of silicon
 A_i is the layout area of chip i where $i = \{\text{motor (m), solar cells (sc), digital cmos}\}$
 t_i is the silicon thickness of each chip i
 α_m is the relative volume of silicon in the motor chip

To save weight, we etched away much of the backside of the SOI wafer of the robot leg/motor chip. Because the robot leg/motor chip volume is not solid silicon, we included an additional factor, α_m , to specify the relative volume occupied by the robot. For our process, α_m is approximately 1/3.

If the robot is moving slowly, the acceleration of the robot can be neglected. While the inchworm motors create forces in the plane of the wafer, our SOI, two-layer polysilicon process allows for linkages and pin-joint hinges which can provide out-of-plane forces. In the case of the prototype robot, the transmission from the motor to the leg is approximately one. Therefore, the weight of the robot must be less than the force that can be generated by the motors:

$$M_{\text{robot}}g < A_{\text{motor}}\sigma_m \quad (8)$$

where

A_{motor} is the area of one inchworm motor (because one leg can be off the ground at times).
 g is the acceleration due to gravity.

Combining equations (6), (7) and (8) yields:

$$\frac{g\rho_{\text{si}}(A_{\text{sc}}t_{\text{sc}} + A_{\text{cmos}}t_{\text{cmos}})}{\sigma_{\text{GCA}}FF - g\rho_{\text{si}}\alpha_m t_{\text{motor}}} < A_{\text{motor}} \quad (9)$$

The above inequality guides the sizing of the motors, given certain constraints on the other chips. With a starting gap size, g_f , of 5 μm and an SOI device layer thickness of 20 μm , the maximum force per unit area at 30 V is about 245 $\mu\text{N}/\text{mm}^2$. Using the param-

eters listed in Table 8 (Section 4.3.3), and a fill factor of 10%, the minimum area for a single inchworm motor is 2.7 mm^2 . However, for a two-legged robot, a single inchworm motor has to support the weight of the other leg's inchworm motor when the other leg is in the air. We found that for two "robot-lifting" motors, the minimum area per motor was 3.5 mm^2 . For extra margin, we designed the robot with inchworm motor areas of 7.5 mm^2 each. Later, however, we moved the Iolanthe process from a $20 \text{ }\mu\text{m}$ SOI device layer to $45 \text{ }\mu\text{m}$ and the high voltage buffer design from a 30 V solar cell supply to a 50 V supply. The fabricated motors would then have a calculated force generation of $400 \text{ }\mu\text{N}$.

3.3 *Inchworm Motor*

Inchworm motors consist of two clutch/drive actuator pairs. Working in tandem, they translate the small displacements of the GCA arrays to large displacements of the shuttle. To maximize the force density of the actuators, the gaps are designed close to the minimum resolution of the process which is limited by the linewidth of the lithography and the aspect ratio of the ASE SOI device layer etch (see Section 2.3).

In this section, we describe some practical guidelines for the design of inchworm motors. Most notably, lateral etching via oxidation and imperfect anisotropies of the silicon ASE etch can affect the final performance of the inchworm motor. Additionally, we introduce polysilicon flaps to direct the shuttle motion allowing nearly unlimited travel of the shuttle. Lastly, we investigate a variant on the original inchworm design, allowing bidirectional operation with equivalent frontward and backward driving forces.

3.3.1 Lateral Etching of Clutch and Drive Gaps

In the SOI/poly process, a high-aspect-ratio ASE etch defines the inchworm motors in the SOI device layer. For high force density electrostatic actuators, it is desirable to have the smallest gap and thickest device layer possible. The thickness of the SOI

device layer can be optimized based on the minimum resolution of the lithography and the aspect ratio of the ASE etch. Our lithography allows us to draw 2 μm lines, and the ASE etch gives us an aspect ratio of 25:1. For device layers that are too thick, the aspect ratio during the ASE etch will widen the gap resulting in a loss of force density. For device layers that are too thin, the gap will not widen as much, but the force is lower due to the reduced actuation area from the thinner device layer. The best result is when the aspect ratio creates gaps on the order of the minimum resolution. In our case, we used SOI wafers with a 45 μm thick device layer.

The ASE vertical etch in the device layer yields a small but finite lateral etch. This results in a lateral etch that is on the order of the minimum resolution of the lithography. The lateral etch affects backstop spacings, electrostatic gaps, and tooth widths in the inchworm motors. If the lateral etch can be predicted a priori, the design of the inchworm can be modified to account for this irregularity.

Figure 36 shows a CAD layout of the clutch, shuttle, and backstop. Two clutch fingers are also shown towards the bottom of the figure. The drawn gaps of the backstop, teeth, and clutch are g_{bs} , g_{teeth} , and g_{clutch} , respectively. Figure 37 shows a close-up SEM image of the fabricated clutch and shuttle. It is important to remember that if a lateral etch uniformly etches the perimeter of the structures with a lateral of δ , the final gap spacing is an additional 2δ on top of the originally drawn width. To prevent shorting of the electrostatic fingers, the gap between the clutch GCA fingers must be larger than the sum total of the backstop gap and teeth gap.

This requirement can be expressed by the equation below:

$$(2\delta + g_{\text{bs}}) + (2\delta + g_{\text{teeth}}) < 2\delta + g_{\text{clutch}} \quad (10)$$

after simplification the inequality yields:

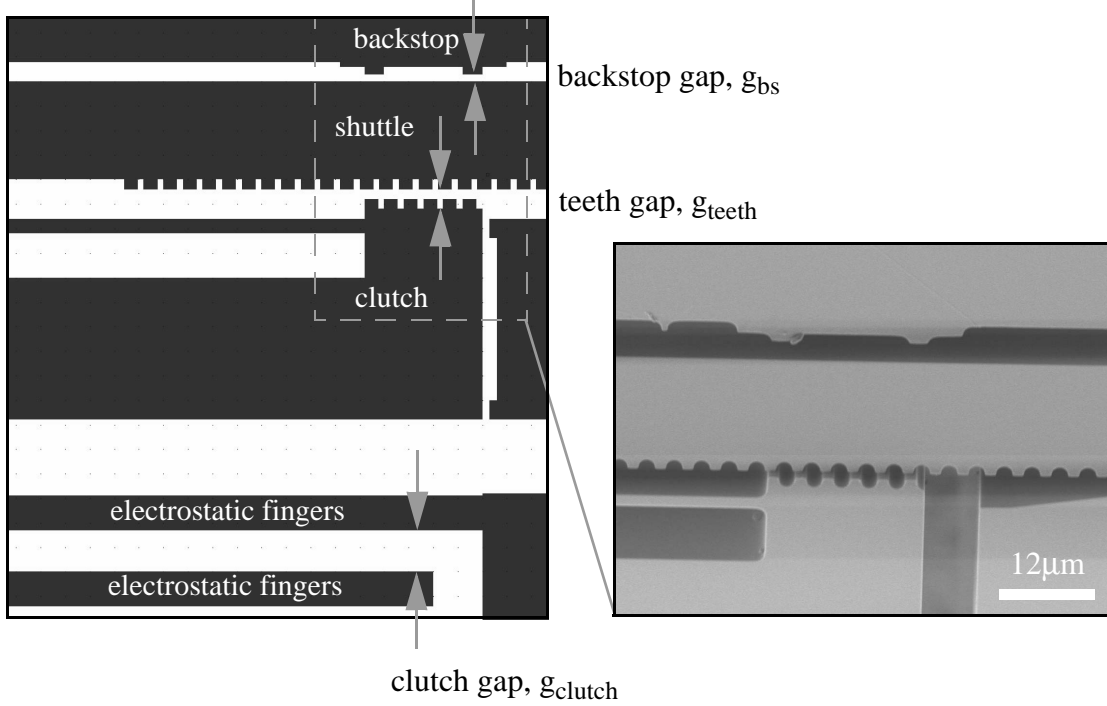


Fig. 36. Layout of backstop, shuttle, and clutch. Spacing of the gap between the shuttle and backstop and between the clutch and shuttle dictate the minimum spacing between the GCA fingers.

Fig. 37. SEM of actual backstop, shuttle, and clutch.

$$2\delta + g_{bs} + g_{teeth} < g_{clutch} \quad (11)$$

Here, we see that as the lateral etch increases, g_{clutch} must also increase to prevent finger shorting. For our inchworms, we tailored the lateral etch so that $\delta = 0.5 \mu\text{m}$. With $g_{bs} = 1.5 \mu\text{m}$, and $g_{teeth} = 4 \mu\text{m}$, g_{clutch} must be greater than $6.5 \mu\text{m}$. In this case we made $g_{clutch} = 8.5 \mu\text{m}$, giving us a tolerance of $2 \mu\text{m}$.

Similar arguments follow for the drive actuator. In this case, there are only two gaps to be concerned with. As Figure 38 shows, the final drive gap must be greater than the final backstop gap. Again, with a lateral etch of δ , we extract the following inequality:

$$2\delta + g_{bs} < 2\delta + g_{drive} \quad (12)$$

and simplifying we have:

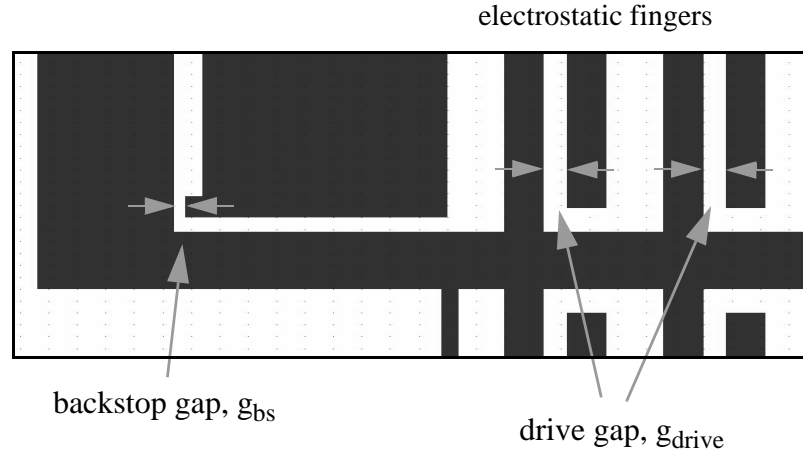


Fig. 38. Layout of drive and drive backstop. Spacing of the gap between the backstop and drive frame dictates the minimum spacing between the GCA drive fingers.

$$g_{bs} < g_{drive} \quad (13)$$

In this case, no amount of lateral etch affects the requirements. The lateral etch on both gaps cancels out the effect. For our inchworms, $g_{bs} = 2.0 \mu\text{m}$ for the drive backstop and $g_{drive} = 4 \mu\text{m}$. Again, this gives a tolerance of $2 \mu\text{m}$.

For both the clutch and drive actuators, the effect of lateral etch also reduces the initial force the GCAs can produce. The inchworm's initial force comes from the drive actuators in their "normally open position," the point where the gap distance is largest. This is determined by:

$$g_f = 2\delta + g_{drive} \quad (14)$$

Based on equations (1) and (12), the actual gap width, g_f , is $5 \mu\text{m}$ instead of the drawn gap of g_{drive} , $4 \mu\text{m}$. This represents a 36% difference between the calculated force based on the drawn gap and the actual gap.

The force applied on the shuttle by the clutch is determined by the gap spacing of the clutch GCA array after the clutch has engaged. With a sufficient clutch force, the

clutch will have pushed the shuttle fully against the backstops. In this case, the final electrostatic gap spacing is $2\ \mu\text{m}$ which produces a force on the shuttle approximately 20x larger than the clutch's normally open position. With such a large increase in engagement force, the clutch GCAs can be designed to be substantially smaller than the drive GCAs of the inchworm actuators.

3.3.2 Lateral Etching of the Inchworm Teeth

Since electrostatic forces are inversely proportional to the square of the gap spacing, it is desirable to have as small a gap as is practical. We are constrained by the minimum linewidth of the lithography and aspect ratio of the ASE etch. Furthermore, to prevent shuttle-clutch slippage, we introduced gear teeth. If the gaps of the GCA arrays are fabricated at the minimum size, the pitch of the teeth is also limited to that distance. In this case, lateral etching plays a significant role in the teeth engagement of the clutch and shuttle.

To understand this issue mathematically, consider Figures 39a-c. The pictures give a close-up view of a clutch engaging the shuttle. In Figure 39a, the lateral etch, δ , is assumed to be uniform around the perimeter of the structures. The drawn tooth width is α (not to be confused with α_m in Section 3.2) while the pitch of the teeth is Ω . In an entire inchworm cycle, each drive actuator needs to pull the shuttle one-half a tooth pitch, $\Omega/2$. The actual toothwidth, T_W , is the drawn toothwidth minus the lateral etch:

$$T_W = \alpha - 2\delta \quad (15)$$

And the actual gapstop spacing is:

$$g_{\text{gapstop}} = \frac{\Omega}{2} + 2\delta \quad (16)$$

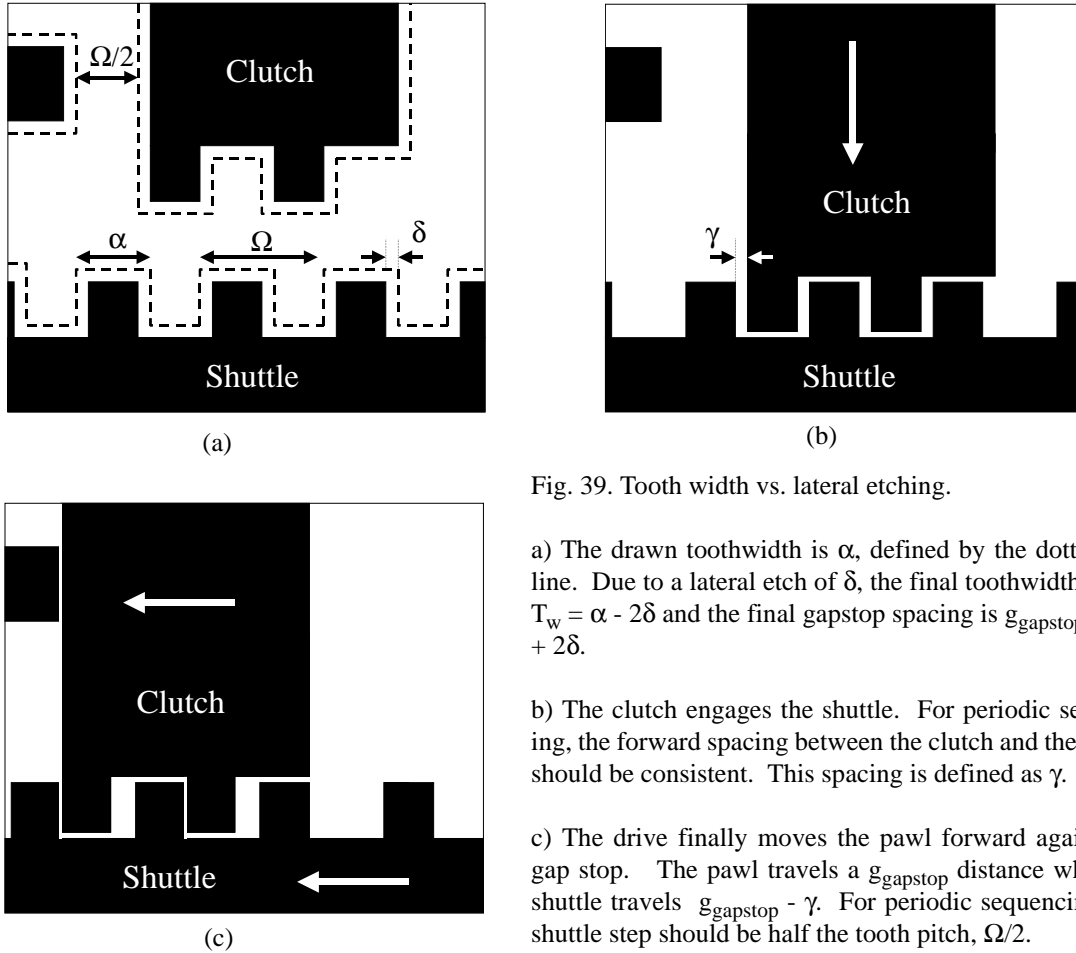


Fig. 39. Tooth width vs. lateral etching.

a) The drawn toothwidth is α , defined by the dotted outline. Due to a lateral etch of δ , the final toothwidth, T_w , is $T_w = \alpha - 2\delta$ and the final gapstop spacing is $g_{\text{gapstop}} = \Omega/2 + 2\delta$.

b) The clutch engages the shuttle. For periodic sequencing, the forward spacing between the clutch and the shuttle should be consistent. This spacing is defined as γ .

c) The drive finally moves the pawl forward against the gap stop. The pawl travels a g_{gapstop} distance while the shuttle travels $g_{\text{gapstop}} - \gamma$. For periodic sequencing, this shuttle step should be half the tooth pitch, $\Omega/2$.

Figure 39b shows the clutch engaging the shuttle. While the inchworm motor operates, it goes through repeated cycles to accumulate large displacements on the shuttle. The clutch should engage the shuttle with the same relative spacing between the teeth for every cycle. Specifically, the clutch will engage the shuttle with a consistent forward spacing between the clutch and the shuttle teeth. In Figure 39b, this spacing is denoted as γ .

In Figure 39c, the drive actuates, and the pawl moves forward against the gap stop. The clutch travels the width of the gap defined by the backstop, g_{gapstop} . The shuttle, however, does not move until the teeth make contact. The clutch first travels a distance, γ , before the shuttle is pulled forward. For periodic sequencing of the inchworm, the shuttle

must travel exactly $\Omega/2$ in order for the next tooth engagement to also have a spacing of γ .

Therefore, we can set up the following equation governing the shuttle step distance:

$$\xi_{\text{gapstop}} - \gamma = \frac{\Omega}{2} + 2\delta - \gamma = \frac{\Omega}{2} \quad (17)$$

and simplifying:

$$\gamma = 2\delta \quad (18)$$

In other words, the forward spacing during engagement is twice the lateral etch of the device.

For the clutch to engage the shuttle, the width of the tooth plus the forward spacing, γ , must be less than the spacing between teeth. If not, the clutch teeth would not fit in the shuttle. We can set up the following inequality:

$$T_{\text{W}} + \gamma < \Omega - T_{\text{W}} \quad (19)$$

This simplifies with the help of equation (15) to:

$$\alpha < \frac{\Omega}{2} + \delta \quad (20)$$

Inequality (20) states that the drawn toothwidth must be less than half the period plus the lateral etch. An additional restriction on the drawn toothwidth requires that the tooth is not completely etched away. This is represented simply enough by:

$$2\delta < \alpha \quad (21)$$

Combining the two inequalities yields the boundary constraints on α :

$$2\delta < \alpha < \frac{\Omega}{2} + \delta \quad (22)$$

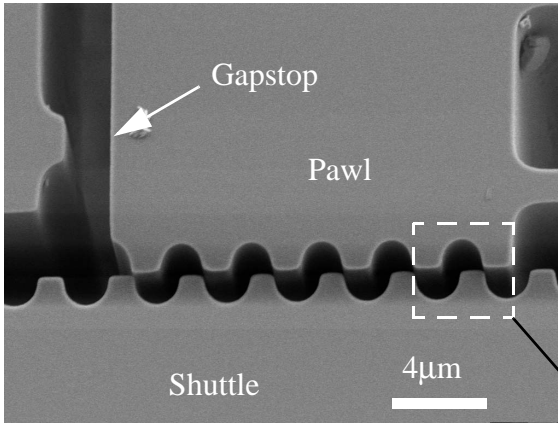


Fig. 40. SEM of gear teeth. With this close-up shot of the gear teeth, one can notice that the teeth are no longer rectangular as they were drawn.

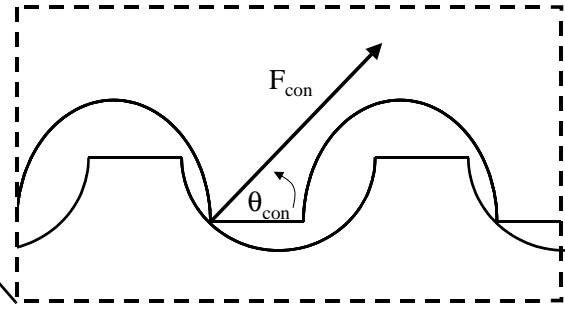


Fig. 41. Close-up drawing of gear teeth. The drawing shows how a nonzero contact angle, θ_{con} , contributes to forces perpendicular to the motion of the shuttle

Assuming a uniform lateral etch is a reasonable first order estimate, one can use (22) as a rule of thumb in designing tooth widths and pitches.

In actuality, rounding and lithography resolution can also affect the final shape and size of the gear teeth. Figure 40 shows a close-up SEM of the clutch and shuttle gear teeth. The gear teeth were drawn as rectangles but because their feature size was on the order of $2\ \mu\text{m}$, the minimum feature size of the process, the fabricated teeth came out fairly rounded.

For clutch/shuttle engagements, the point where one tooth of the clutch contacts one tooth of the shuttle can affect the force transfer from the drive actuator to the shuttle. In this case, we define the contact angle, θ_{con} , as the angle the contact force makes with the direction of the shuttle. For example, a nonzero contact angle, θ_{con} , (as shown in Figure 40) can have a force, F_{con} , whose components consist of forces parallel and perpendicular to the motion of the shuttle. A large perpendicular force can act against the electrostatic force of the clutch actuator, reducing the engagement strength of the clutch. In some cases, slip of the clutch with the shuttle can occur, ultimately limiting the overall

output force of the inchworm motor.

3.3.3 Bidirectional Motion in Inchworm Motors

In the next sections, we move away from the details of optimizing the motor and discuss bidirectional motion in inchworm motors. The inchworm motors from Yeh were originally designed to drive in one direction [56]. Resetting the shuttle was done with a pair of parallel beam flexures (see Figure 42). Once both clutches released the shuttle, the shuttle would spring back to its nominal position. Instead of using parallel flexures the inchworms of the robot described in this dissertation used serpentine springs to recoil the shuttle back to its initial position (see Section 3.5.2, Figure 54).

As alternatives to the aforementioned techniques, we discuss two additional methods for reversing the shuttle direction in an inchworm motor. Section 3.3.3.1 discusses reversing the driving sequence of the inchworm motors. Force in the backward direction is controlled by the size of the restoring spring of the drive GCA array. In another scenario, one may wish to have a motor with equivalent frontward and backward force outputs. Section 3.3.3.2 solves this problem by adding an additional set of biasing GCA arrays. The biasing arrays act as a transmission, allowing bidirectional actuation of the drive GCA array.

3.3.3.1 Reinforced Restoring Spring in Drive Actuator

One method for reversing the motion in an inchworm motor is to sequence the inchworm in the opposite direction. Figure 43 shows only a single clutch/drive actuator pair, but this is sufficient to demonstrate the reversing mechanism. In the initial position (Figure 43a), both the clutch and drive actuators are at rest. The drive actuator is initially preset before the clutch engages (Figure 43b). Then, the clutch engages (Figure 43b).

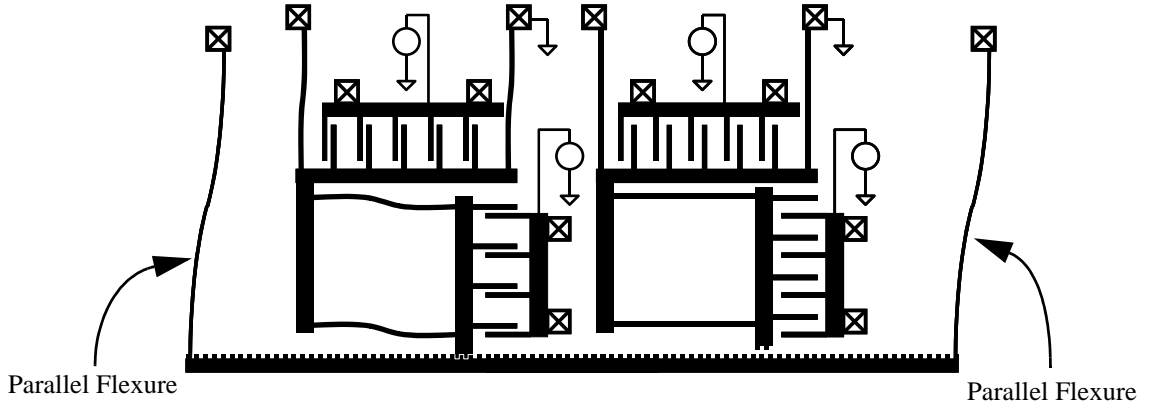


Fig. 42. Diagram of inchworm motor with shuttle. Shuttle is supported by two parallel flexures which constrain the motion of the shuttle. Shuttle is reset by the restoring force of the parallel flexures.

Since the drive is already preset, the engagement with the shuttle is one half-pitch in the backwards direction (Figure 43c). Lastly, the electrostatic drive force is turned off allowing the restoring spring to force the shuttle in the reverse direction (Figure 43d).

The restoring force depends on the drive restoring spring (see Figure 43a). In the static view, the force of the spring should be greater than the load through at least half the period of motion, which is half the pitch of the teeth. As we have seen in Section 3.3.2, total displacement of the clutch is actually larger than half the tooth pitch due to the etch in the lateral direction. As previously defined, γ represents the forward spacing between the teeth of the clutch and the shuttle. In a similar vein for reversible motors, the same γ can be related to the maximum force the drive restoring springs can exert on the shuttle. In Figure 43b, the springs are preset a distance of (from Section 3.3.2):

$$g_{\text{gapstop}} = \frac{\Omega}{2} + 2\delta \quad (23)$$

If the drive restoring springs must pull the shuttle half the pitch, $\Omega/2$, then at the end of the restoring action in Figure 43d, the spring will be stretched $2\delta = \gamma$ at maximum. Therefore, the load must satisfy the following inequality for the inchworm to operate in

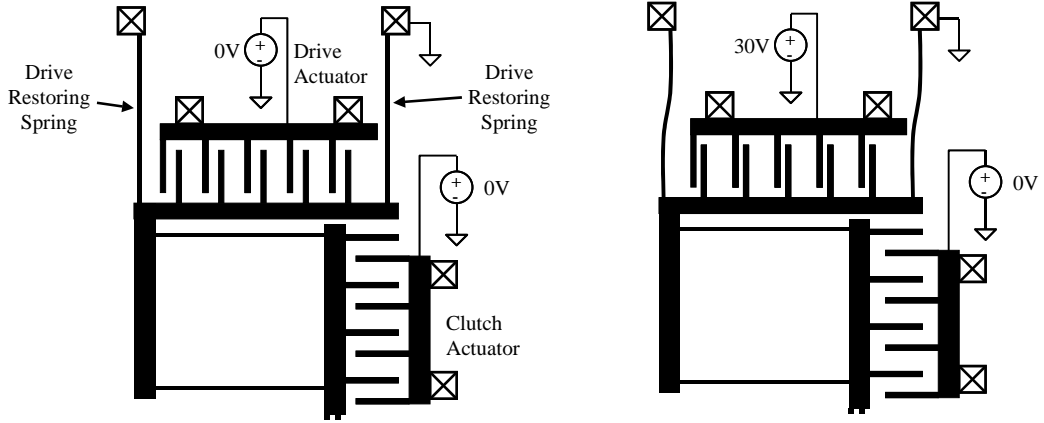
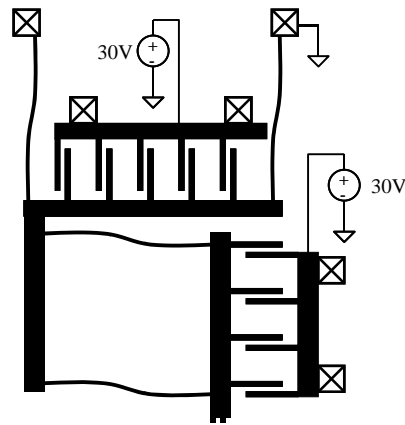
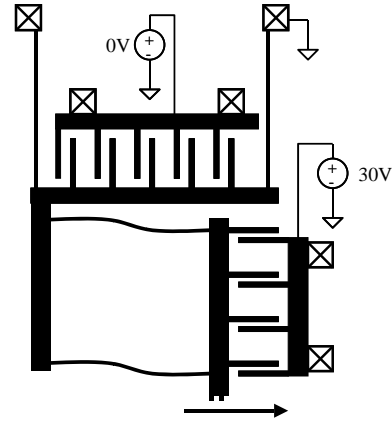


Fig. 43. Reversing sequence of inchworm motor.
a) In the initial position both the clutch and drive actuators are at rest.

b) The drive actuator is initially preset before the clutch engages.



c) Clutch engages while drive is preset.



d) Turning off the drive actuator allows the drive restoring drive spring to pull the shuttle backwards.

the negative direction:

$$\gamma k_{\text{spring}} < F_{\text{load}} \quad (24)$$

where

k_{spring} is the spring constant of the drive restoring springs

F_{load} is the load on the shuttle

As an example, the two-DOF leg presented in Section 3.5.3 is driven using this reversible mechanism. The drive restoring spring constant is $16 \mu\text{N}/\mu\text{m}$, and the lateral etch rate is $\delta = 0.5 \mu\text{m}$. According to inequality (24), the shuttle load in the reverse direction is limited to $16 \mu\text{N}$.

Of course, the drive restoring spring acts against the drive GCA arrays, and hence, the overall drive force in the forward direction is reduced. If the reverse load is equivalent to the forward load this driving scheme seems less desirable than other possibilities. While it is certainly possible to design such a system, the stiffer spring will necessitate more actuator area to accommodate the larger restoring force. Therefore, in the next section, we introduce a different reversible motor concept.

3.3.3.2 Symmetric Bidirectional Inchworm Motor

As discussed earlier in this chapter, a variety of methods can be used for bidirectional actuation. The feature that separates competing concepts is force density. Ultimately, the goal is to provide a high force, large displacement actuator in as small a die area as possible. One possible design that has a minimal effect on force density yet offers equivalent output force in either direction is shown in Figure 44. The addition of two small sets of GCA arrays (left and right) enables one to bias the drive array in one direction or the other. Figure 44a shows a cutout section of the motor that contains the drive array and biasing array. The clutch mechanics are identical to the original motor and therefore, are not included in this figure. The biasing frame is used to bias the drive GCA array in one direction or the other.

In Figure 44b, the right GCA array is charged to -20 V, causing the biasing frame to actuate to the right. This places the drive electrodes closer to one set of the electrostatic fingers than the other. Gap stops (not shown) prevent the left/right GCA arrays from shorting. In Figure 44c, the drive frame is actuated to the left by applying 30 V onto the biasing frame. The biasing GCA arrays are decoupled from the engagement of the shuttle, so in the practical limit, they can be designed arbitrarily small. Therefore, the biasing GCA array need not have a large force, just enough force initially to move the biasing

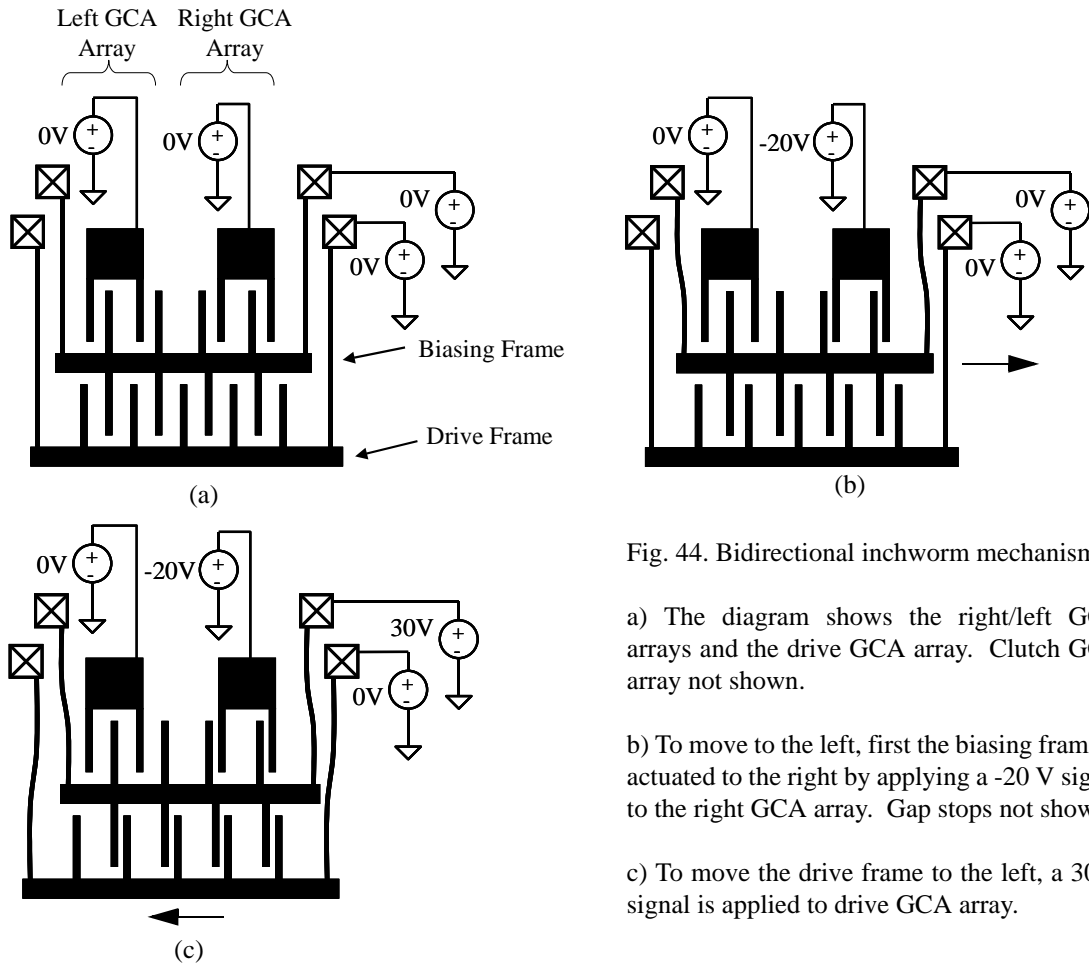


Fig. 44. Bidirectional inchworm mechanism.

a) The diagram shows the right/left GCA arrays and the drive GCA array. Clutch GCA array not shown.

b) To move to the left, first the biasing frame is actuated to the right by applying a -20 V signal to the right GCA array. Gap stops not shown.

c) To move the drive frame to the left, a 30 V signal is applied to drive GCA array.

frame. Consequently, the biasing GCA array need only be a fraction the size of the drive GCA array, and therefore, the force density of the actuator is not significantly degraded.

The bidirectional motor offers compelling force densities in both directions with a minimal effect on force density. However, the motor is further complicated by the addition of two more signals and thus requires a more complicated signal stream to drive the motors. If negative voltages are available, the biasing electrodes can be simply biased before a right or left motion commences. Then, the signal streams for the drive and clutch actuators can remain the same. Instead, if negative voltages are not available, the motors can also be driven in either direction with a more complex signal stream that requires switching all six signals in a single inchworm cycle. Table 6 shows the drive sequence to

Table 6: Sequence to Drive Shuttle to the Left

Step	Clutch A	Drive A	Clutch B	Drive B	Right GCA	Left GCA
a	1	0	1	1	0	1
b	1	0	1	1	1	0
c	1	1	0	0	1	0
d	1	1	0	0	0	1
e	1	1	1	0	0	1
f	1	1	1	0	1	0
g	0	0	1	1	1	0
h	0	0	1	1	0	1

actuate the bidirectional inchworm to the left.

As a last note, unlike a single direction inchworm motor where the drive frame is always at ground relative to the substrate, the movable frames of the bidirectional motor undergo nonzero voltages. This is not a problem in the Iolanthe process because the substrate can be removed underneath the motor. However, in a single mask SOI process [57], the electrostatic forces between the frame and the substrate can cause the structure to pull in to the substrate.

3.3.4 Constraining Motion of Shuttle

Yeh's inchworm motors used parallel flexures in the SOI device layer that were stiff out-of-plane, yet flexible in plane (see Figure 42). In addition to resetting the position of the shuttle after actuation, these flexures constrained the shuttle to translate in the direction of operation. Depending on the design however, there is a trade-off between force and displacement. To overcome this obstacle, we have suggested using flaps in place of the parallel flexures. Like the parallel flexures, the flaps confine the shuttle to the plane of the actuator. With the use of the polysilicon layers from the Iolanthe process, we were able to design flaps to constrain the motion of the shuttle to the plane of the device. As seen in Figure 45, the flap attached to the shuttle on the left prevents the shuttle from fall-

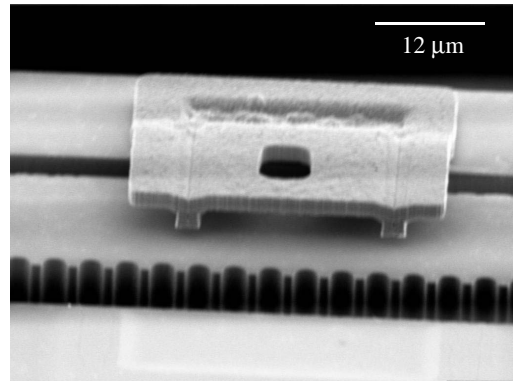
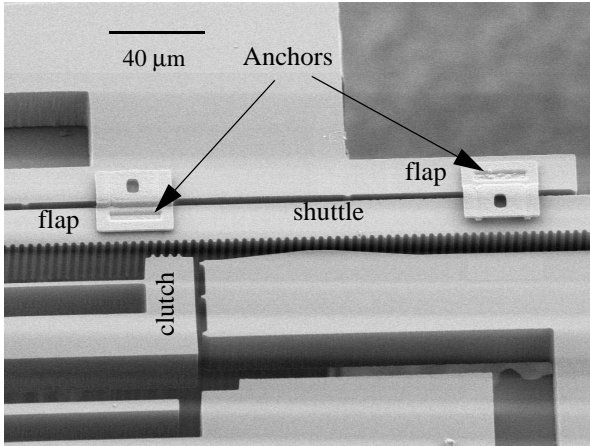


Fig. 45. The inchworm motor shuttle and pawl. a) The flaps are used to constrain the motion of the shuttle. Flap anchors are labeled to show the direction of the flap constraint.

b) Close-up view of flap. Flap is designed with dimples to minimize contact with the shuttle. A POLY1 dummy layer is used to make the dimples.

ing through the wafer, and the flap over the shuttle on the right prevents the shuttle from popping up out-of-plane. A close-up of the flaps (Figure 45b) reveals dimples on the underside. A POLY1 sacrificial rectangle with slots is used to make the dimples on the POLY2 layer. During release, the POLY1 rectangle floats away. The dimples are used to minimize the contact area of the flaps on the shuttle.

While the use of flaps allows the shuttle unconstrained travel, we have subjected the inchworm motor to additional contact friction. Furthermore, the polysilicon flaps can fracture much more easily than parallel flexures in the SOI device layer. In our release and assembly of the robot, we took special care not to damage the flaps (see Section 2.4).

3.4 *Iolanthe Design Considerations*

With the ability to design high force actuators with thin polysilicon flexures, one can imagine a number of design advantages. We describe here some design considerations we encountered developing this robot including: 1) the use of preset structures to maximize initial out-of-plane moments, 2) creation of dummy blocks to ensure defect-free polysilicon structures, and 3) considerations for electrical wiring on the robot.

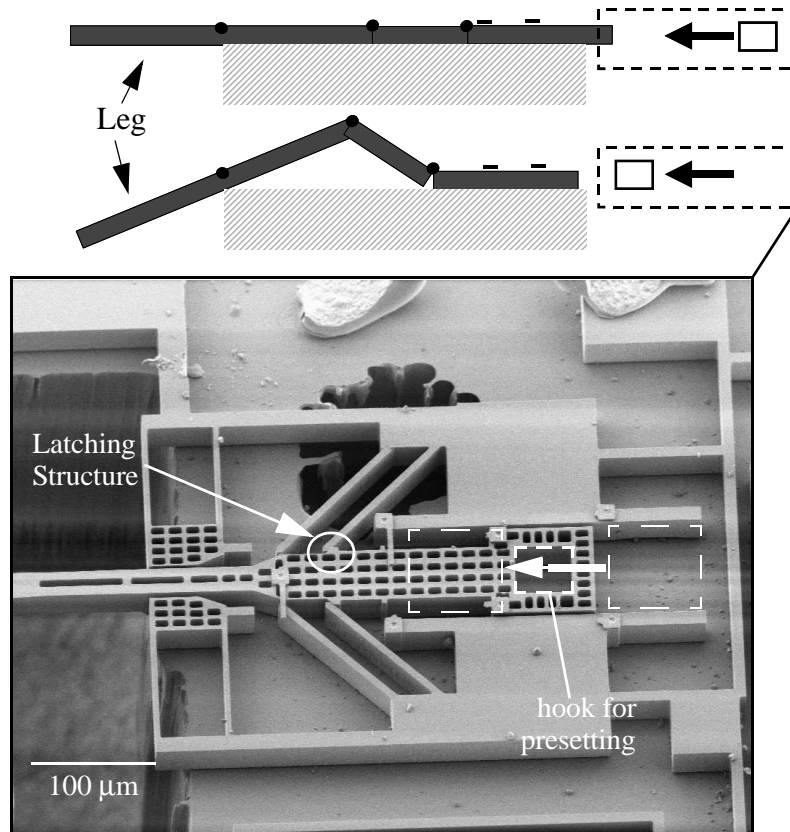


Fig. 46. SEM of latch structure. The latch is midway between starting position and latched position. Schematic shows how leg is moved out of plane for a larger initial moment arm.

1. To take advantage of out-of-plane actuation, hinges can be designed in this process. However, the designs are initially planar during fabrication, so initial out-of-plane torque is limited ultimately to the device layer thickness. Preset structures that lock into place can be used initially to set structures significantly out of the plane. The lever arm is then no longer limited to the thickness of the substrate, and larger initial torques can be obtained. As shown in Figure 46, a preset structure can be translated and latched into place with a manual probe. Guided by the preset structure, the shuttle of the inchworm motor is also repositioned.

2. As another design methodology in the Iolanthe process, we discuss ways to form defect free polysilicon structures. Because the glass planarization process can

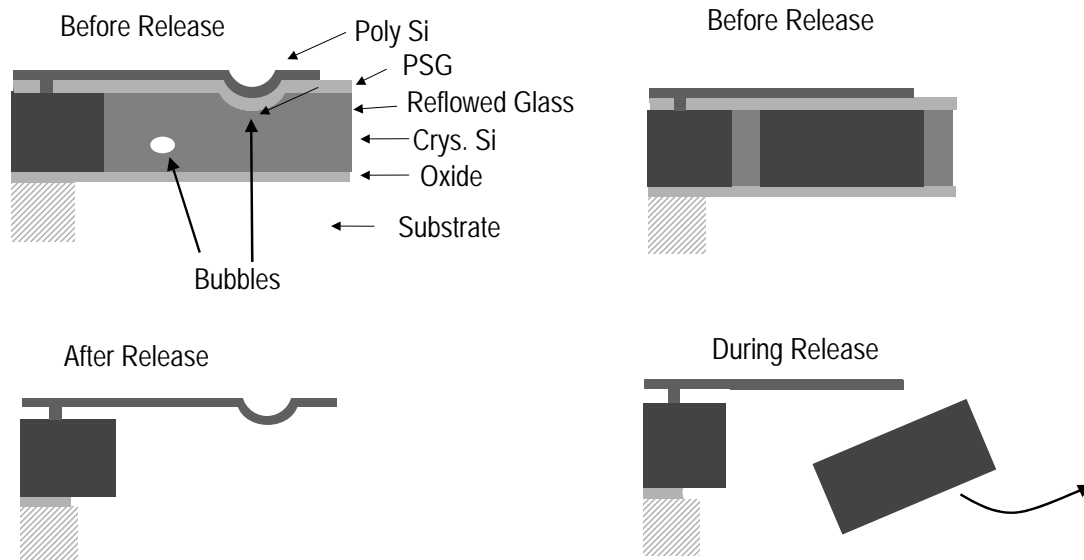


Fig. 47. Bubble deformation of Poly-Si. a) Bubbles can appear and interrupt the planar poly-Si. Once released, the Poly-Si forms the shell of the bubble.

b) To avoid bubble deformations, a dummy SOI block beneath the sheet of poly-Si prevents this deformation.

embed bubbles within the device layer, subsequent polysilicon layers can be deformed by the bubble shell. In large areas of reflowed glass, bubbles can appear and interrupt the planar polysilicon. Once released, sheets of polysilicon can have shells of bubbles embedded in them. This can be seen in Figure 47a. To avoid bubble deformations, one can place a dummy SOI block beneath the sheet of polysilicon. When released, the dummy device block floats away leaving a planar polysilicon layer behind (Figure 47b). One example of a device that took of advantage of this is the slider test structure in Figure 72 in Section 4.3.1.

3. Like printed circuit boards, we only need two conductive layers plus a via layer to do arbitrarily complex connections. In this case, we can use the SOI device layer, POLY2, and the CONT mask, which provides the electrical vias from one layer to the other. With just these two layers, we can draw connections from the inchworm motors into a row of bond pads near the back of the robot. An example of a polysilicon wire bridging an SOI wire is shown in Figure 48. Wiring over long distances is a bit problem-

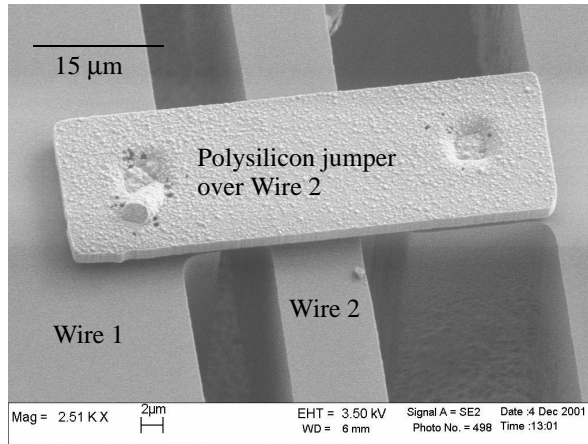


Fig. 48. Polysilicon jumper bridges Wire 2.

atic in the SOI device layer. Since both the SOI and polysilicon are susceptible to electrostatic pull-in after the glass and silicon dioxide are removed, SOI anchors were placed periodically along the wire. These anchors provided enough mechanical stiffness to withstand electrostatic forces between the SOI wiring and substrate.

3.5 *Out-of-plane Linkages and Legs*

The next step in design was to translate the motion of the motor's shuttle into leg movement. The flexibility of the Iolanthe process allowed us to freely create structures that moved out-of-plane. Here, we describe how to make hinges and legs with the polysilicon layer atop the SOI device layer. We also describe two leg designs we created: a one-DOF leg used on the robot and a two-DOF leg to test the motion of a more complex leg structure.

3.5.1 Hinge Design

In designing hinges using polysilicon, careful attention must be paid to the thickness of the oxide and polysilicon layers. For the Iolanthe process, the pins in Iolanthe are restricted in lateral motion by the oxide thickness surrounding the pin during fabrication (Figure 49). With this type of pin hinge, there are two limitations on the thicknesses of

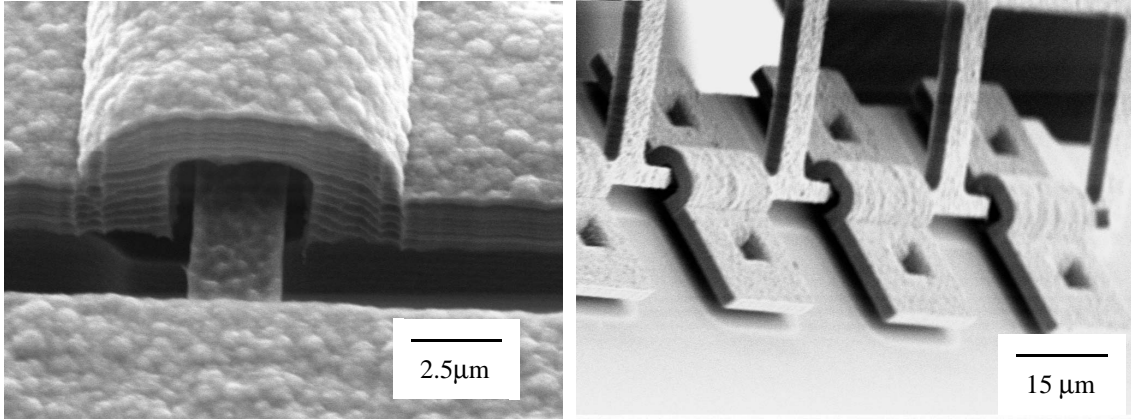


Fig. 49. SEM images and cross sections of hinges. a) Image of hinge. The striations on the POLY2 layer are artifacts of the ASE etch.

b) Image of a rotated hinge.



c) The POLY1 layer needs to be thick enough such that the pin of the hinge does not get wedged near the POLY2 anchors.

d) The pin needs to rotate freely. To accomplish this, the hinge staple needs spacing to accommodate the pin hinge at a diagonal.

the poly and oxide layers that define the hinge. First, a layer thickness is chosen that prevents the pin of the hinge from becoming trapped under the POLY2 anchors. This problem is shown graphically in Figure 49c. Therefore, the layer thicknesses are limited by the following inequality:

$$LTO1 + LTO2 < POLY1 \tag{25}$$

where

LTO1 is the thickness of the first PSG layer

LTO2 is the thickness of the second PSG layer

POLY1 is the thickness of the first polysilicon layer

For a cross section of the Iolanthe process, see Section 2.3.

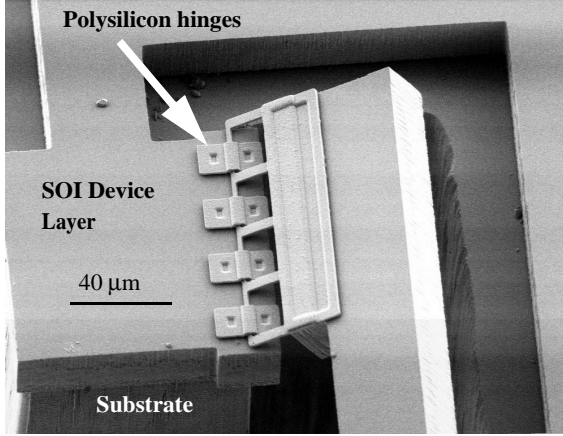


Fig. 50. Polysilicon hinges attached to SOI device layer. The substrate is also seen in this SEM.

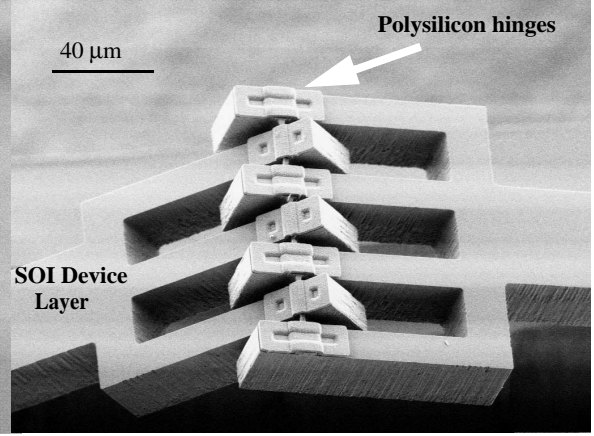


Fig. 51. Interdigitated SOI device layer fingers. This hinge has a rotation range of almost 360°.

Secondly, the pin needs to rotate freely. To accomplish this, the hinge staple needs spacing to accommodate the pin at its maximum height when it is rotated at 45°. Assuming $LTO1 < LTO2$, we have:

$$\sqrt{2}POLY1 < LTO1 + LTO2 + POLY1 \quad (26)$$

Combining equations (25) and (26) yields the simplified condition below:

$$1 < \frac{POLY1}{(LTO1 + LTO2)} < 1 + \sqrt{2} \quad (27)$$

The design parameters for Iolanthe are: $POLY1 = 2.5 \mu\text{m}$, $LTO1 = 0.55 \mu\text{m}$, and $LTO2 = 1.5 \mu\text{m}$. Evaluating the middle expression in (27) yields $1 < 1.6 < 2.4$. The value, 1.6, is clearly within the reasonable bounds of the requirement.

Fabricated devices in Iolanthe used two different hinge designs. Figures 50 and 51 show SEM photos of the fabricated hinges. In Figure 50, the hinges are designed entirely out of polysilicon, only using the device layer as the base. In Figure 51, however, the SOI device layer is interdigitated among the individual fingers formed with the SOI device layer. This allows the hinge almost 360° of motion.

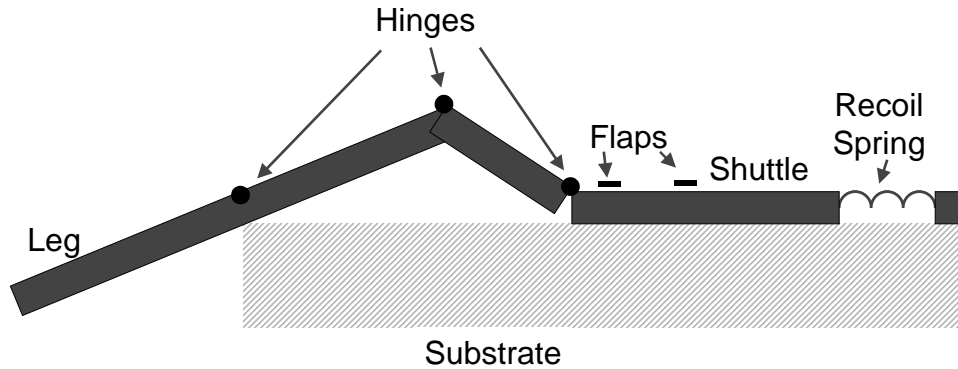


Fig. 52. Schematic of one-DOF leg. The one-DOF leg is composed of three rigid links and three hinges. These form the base of the linkage, transforming the displacement from the shuttle to leg motion in front. Since the inchworm drives predominately in one direction, a recoil spring is used to reset the leg motion upon completion.

3.5.2 One-DOF Leg

In previous sections of this chapter we discussed basic mechanical components for out-of-plane actuation and design considerations for inchworm motors. Here, we use those components to design an inchworm-actuated, out-of-plane, one-DOF leg. Figure 52 shows the conceptual design of the leg. The leg is based on a slider-crank mechanical construct. A combination of sliders and hinges transform linear displacement into angular rotation.

Designing the lengths of the leg segments appropriately, we can get a 1:1 mechanical coupling from shuttle actuation to vertical leg distance. Figure 53 shows the shuttle displacement versus the vertical deflection of the leg. Furthermore, by following the equations relating robot weight to motor force (Section 3.2), we can determine the needed size of the inchworm motors. In this case, we calculated an inchworm motor area of 7.5 mm^2 .

Given these constraints, we designed the legs and inchworm motors shown in the CAD layout in Figure 54. The majority of the backside is removed to reduce the total mass of the robot. Furthermore, substrate is removed underneath the SOI device layer

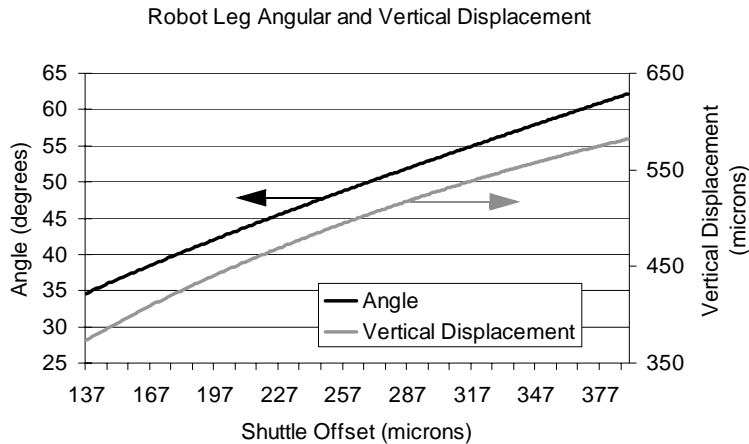


Fig. 53. Angular deflection and vertical displacement of leg tip. The mechanical advantage of this linkage is approximately one. Therefore, the downward force of the leg is comparable to the horizontal force of the shuttle.

areas that contain moving structures, such as the shuttle and the moving frames of the inchworms. This reduces the chance these structures will stick to the substrate after the release of the structures from the glass.

To reset the leg, a serpentine spring allows the shuttle to recoil to its nominal position after the leg is actuated forward. The preset structure located near the back of the robot presets the shuttle 150 μm for an initial moment arm. This sets the shorter leg 30° out of the plane. Lastly, a set of four hinges converts the linear motion to angular motion. Two “hip” hinges are placed on either side of the leg. This helps reduce excessive moments on the hinges from leg tip forces that could occur off-axis from the shuttle. Flaps with dimples are also used to constrain the motion of the shuttle to lie within the plane of the inchworm.

Figure 55 shows the final layout of the whole robot structure for Iolanthe. A space in the back of the robot approximately 2 x 3 mm² is reserved to hold the Icarus and CMOS chips. Using the SOI device and polysilicon layers, we can route the signals from the motors to bondpads in the back. With two motors and four signals for each motor, 8 signal

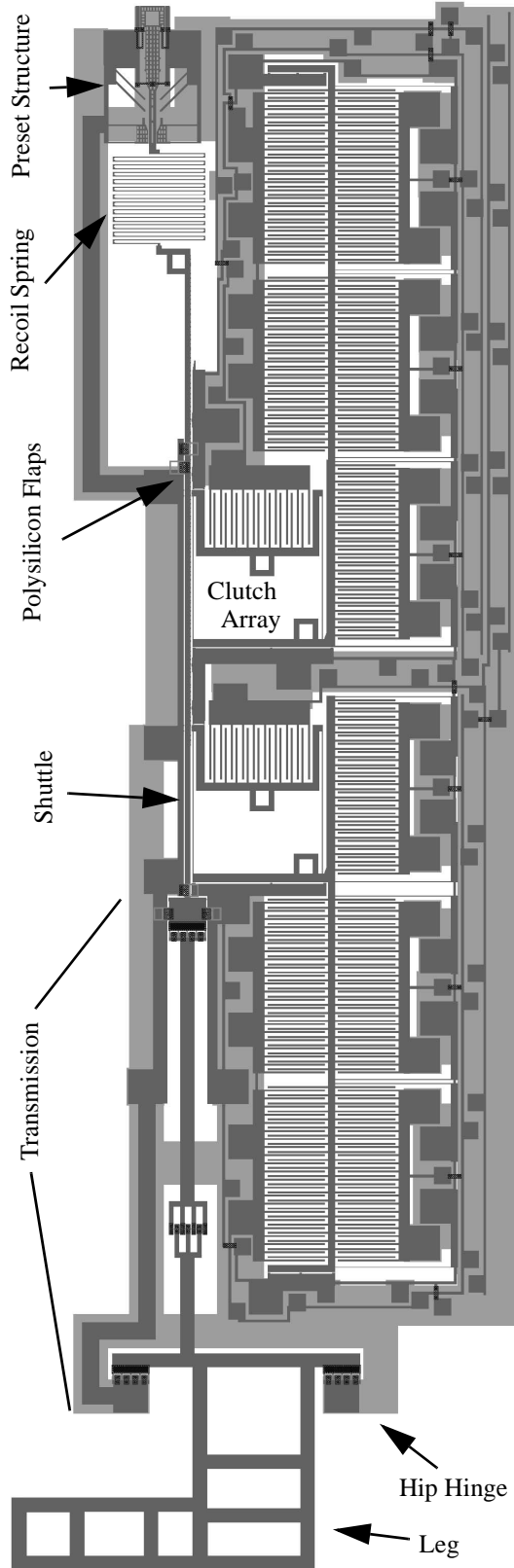


Fig. 54. CAD drawing of single leg and inchworm motor of the robot. The leg/motor length is 6 mm.

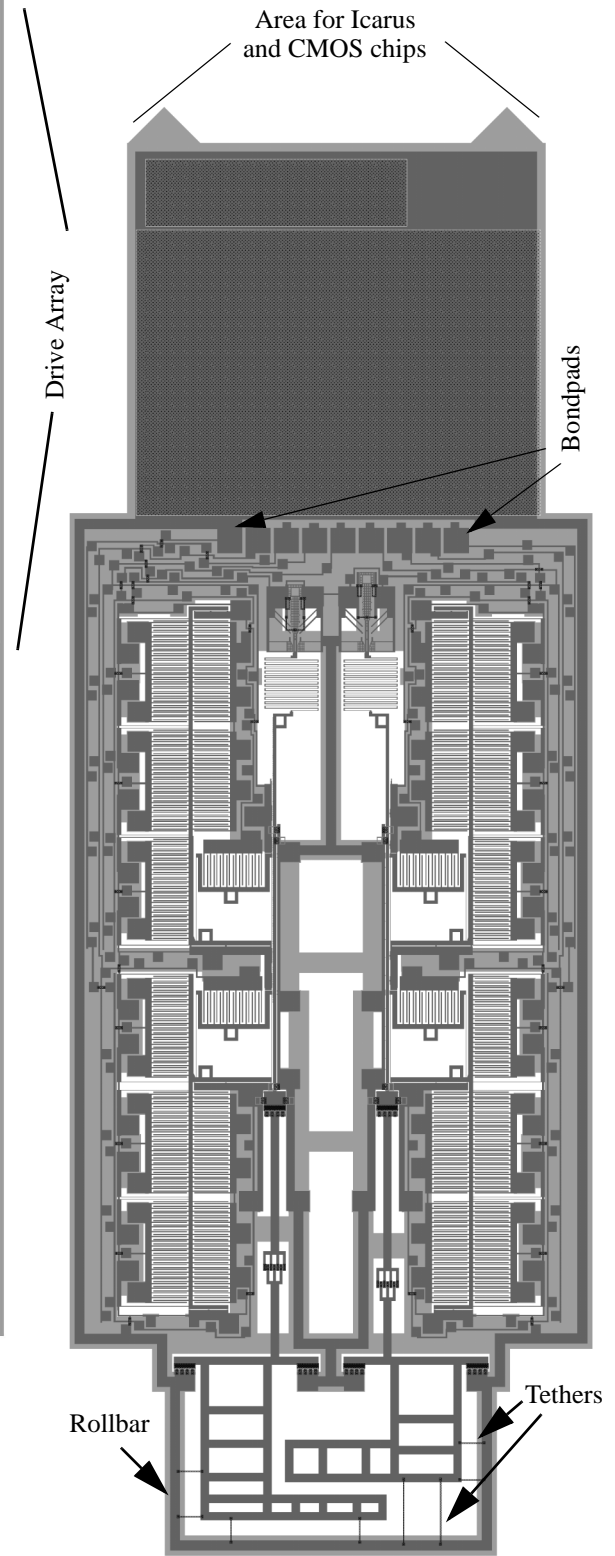


Fig. 55. CAD drawing of robot frame with both legs. The length of the robot is 8.6 mm.

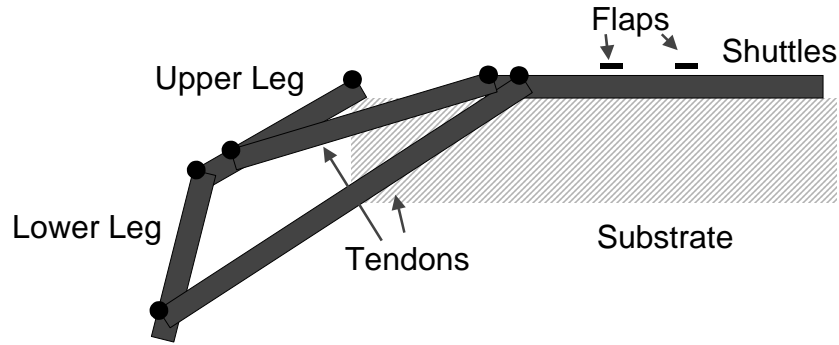


Fig. 56. Two-DOF leg schematic. Two motors drive the tendons of the upper and lower legs. Flaps, again, constrain the motion of the shuttles. However, the shuttles have no recoil spring, so they reverse direction by reversing the driving sequence of the inchworms.

pads and a ground pad are required. Lastly, to protect the legs during release and assembly, a rollbar surrounds the legs. The rollbar, consisting of substrate and device layer SOI, is substantially more robust than the legs with polysilicon hinges. The legs are held in place by polysilicon tethers that attach the legs to the rollbar. Robots that are dropped or bounced around during the release can absorb hits on the rollbar much more effectively than on the legs.

3.5.3 Two-DOF Leg

While the one-DOF leg was used in the final robot, one could readily imagine designing more complex linkages through Iolanthe. As an example, the conceptual drawing of a two-DOF leg is shown in Figure 56. While we will focus our attention on this one type of leg, the Iolanthe process could easily realize a plethora of alternative two-DOF linkages. The leg uses two inchworm motors to drive two shuttles. Each shuttle is attached to a tendon which in turn moves an upper or lower leg. The upper leg assembly is, again, a slider-crank mechanical construct like the one-DOF leg. The upper leg orientation depends solely on the position of just one shuttle. The lower leg is part of a 5-bar crank-slider construct, and its orientation depends on the positions of both shuttles.

The conceptual drawing is realized in the CAD design shown in Figure 57. Again,

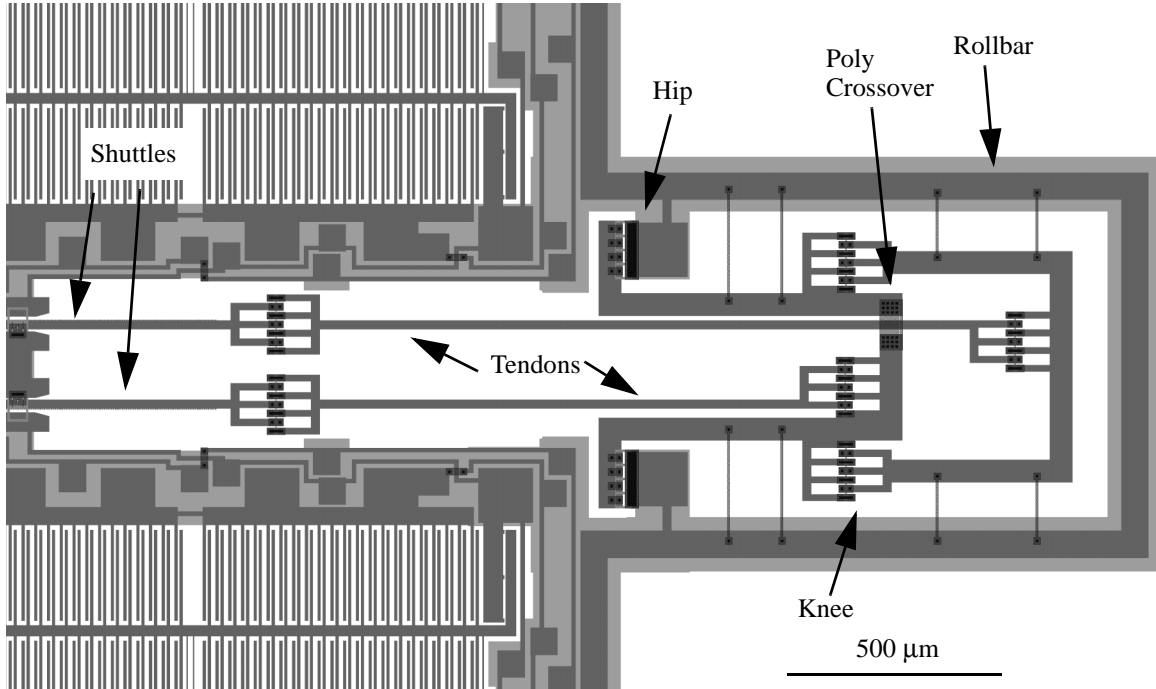


Fig. 57. CAD drawing of two-DOF leg. Shuttles attach to the upper leg and lower leg. Hip and knee joints allow flexing of the leg out of the plane.

flaps constrain the motion of the shuttle to remain in the motor's plane. A rollbar is used to tether the legs in place and protect the legs during release and assembly. Lastly, as more degrees of freedom are implemented, cross-over beams are needed to bridge overlapping mechanical structures. In this case, only one polysilicon cross-over beam is used. The polysilicon cross-over beam (see Figure 57) bridges the lower leg structure overtop one of the tendons.

One way we simplified the mechanical design of the two-DOF leg over the one-DOF leg is the removal of the recoil spring. In this case, the shuttle is suspended only by the polysilicon flaps. Lifting the leg up requires only enough force to overcome the friction of the flaps and hinges which should be small compared with lifting up a robot. Since we require large forces in one direction and small forces in the other, we can simply reverse the driving sequence of the inchworms to lift up the leg (see Section 3.3.3) eliminating the need for a recoil spring. This is a good example of how we can trade complex-

ity of designs among the three processes. By marginally increasing the complexity of the sequencing in the CMOS chip, we can reduce the complexity of the mechanical design in the Iolanthe chip.

3.6 Solar Cells and Transistors from the Icarus Process

The chip containing the solar cells and the high-voltage transistors was fabricated in the Berkeley Microfabrication Facility using the Icarus process. This solar-cell/high-voltage-transistor process is an 8-mask, simplified CMOS process with a ninth mask to define isolation trenches (see Section 2.2). Originally proposed by Brosnihan *et al.* [7], isolation trenches are used to electrically isolate devices on an SOI wafer. The Icarus process allows one to integrate electrically-isolated MOSFETs along with solar cells onto a common SOI substrate.

3.6.1 High-Voltage Transistors

In designing the Icarus process, it was important to understand the factors that affect the breakdown voltage of high voltage (HV) devices. For further reading, Hussein and Declercq discuss in detail breakdown phenomena, high-voltage transistor designs, and associated fabrication processes [4]. For our purposes, we satisfy ourselves with some simple guidelines for designing HV devices. There are a few different types of breakdown voltages: 1) oxide breakdown, 2) avalanche breakdown, and 3) surface breakdown.

1. Oxide breakdown can be a destructive (nonreversible) process where the electric field is strong enough to compromise the integrity of the oxide. Breakdown voltages for silicon dioxide are on the order of 10 MV/cm. With a 1000 Angstrom gate oxide, we would expect a breakdown voltage of 100 V.

2. For PN junctions, avalanche breakdown occurs when electrons gain enough energy to create a secondary hole-electron pair. These secondary pairs collide with ter-

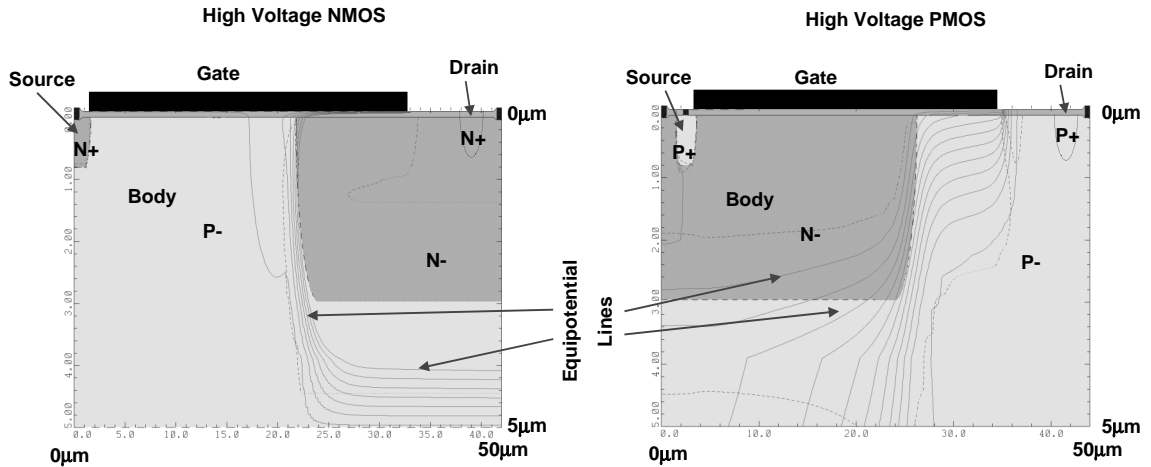


Fig. 58. Avant! Medici simulation of potential fields across HV devices. a) HV NMOS device. Equipotential lines indicate lines of constant voltage.

b) HV PMOS device. Drain connects to device layer but is separated from other devices via isolation trenches.

tiary pairs causing a chain reaction. The energy of the electrons can be characterized by the electric field strength in the depletion region. As the depletion region expands, the electric field for a given voltage shrinks. The width of the depletion region depends on the doping concentrations at the PN junction. Lower concentrations yield larger depletion region widths and consequently higher breakdown voltages. Another factor that affects electric field strength is the geometry of the device. Sharp corners in a diode will exhibit lower breakdown voltages than smoother varying interfaces. The radius of curvature for a PN junction can be used as a metric for determining the breakdown voltage [28]. For higher breakdown voltages, larger radii are preferred. In driving in the p-well and n-well species in the Icarus process, we obtained a diffusion depth of at least $3\ \mu\text{m}$. As a rough rule of thumb, the lateral diffusion rate is 75% of the vertical diffusion rate, leaving us with a radius of curvature of a square diode of approximately $2.25\ \mu\text{m}$. With background dopings for the n-well on the order of $3 \times 10^{16}\ \text{cm}^{-3}$, the diode breakdown voltage was expected to be over 50 V.

3. Finally, surface breakdown is caused by surface charges that affect the depletion

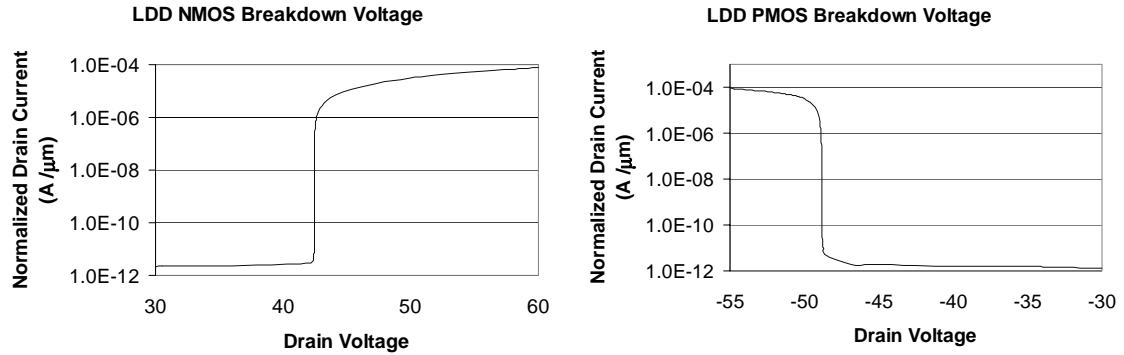


Fig. 59. Simulated breakdown curve for HV CMOS using Medici. a) For $V_{gs} = 0$, plot shows a breakdown voltage of 43 V for NMOS transistors.

b) For $V_{gs} = 0$, plot shows a breakdown of -49 V for PMOS transistors.

region of a PN junction. Surface charges can be due to either trapped ions in the surface oxide or conductive plates above the surface. One example of a conductive plate in the Icarus process is the polysilicon gate layer. Depending on the polarity of the surface charge, the depletion region can either be “pinched” or expanded. Pinched depletion regions result in higher electric fields, ultimately reducing the breakdown voltage of the junction.

The high electric fields of a gate-aligned transistor are found at the gate/drain overlap region. The gate acts as a field plate that causes the depletion region to be pinched. To counter this effect, one can incorporate a lightly doped drain (LDD) extension. The LDD is an area where the dopant is still N-type for NMOS transistors, for example, but the concentration is much lower. The result is an increase in the depletion region width at the interface and a reduction in the electric field strength. Using this concept we have designed both HV NMOS and PMOS transistors (Figures 58a and b). Most notable about the PMOS device is the location of the drain. For gate-aligned transistors, the PMOS would be entirely located within the N-well. In this case, however, the drain is connected to the device layer outside of the well. Electrical isolation between devices is still maintained because of the isolation trenches in the SOI. Furthermore, HV CMOS is possible

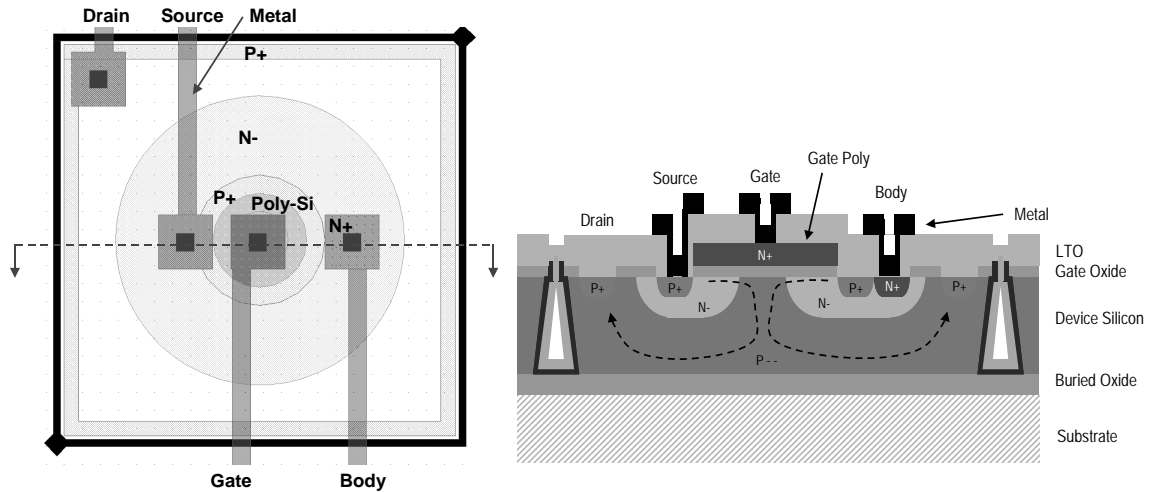


Fig. 60. Vertical DMOS transistor. a) CAD drawing of circular HV transistor. Circular design has no sharp geometries.

b) Cross section of DMOS transistor. By incorporating drain under the gate, higher breakdown voltages are possible.

without any alterations in the Icarus process. The resulting breakdown voltages were simulated with Avant! Medici, a modeling tool that uses the Poisson-Boltzmann equations to determine electric field strengths, among other transistor characteristics. Figures 59a and b show the breakdown curves for the HV transistors. Simulated breakdown voltages for the devices were 43 V and -49 V for the NMOS and PMOS devices, respectively.

Lastly, another HV PMOS transistor design is the vertical buried layer DMOSFET. Because of the P-type device layer, only P-channel DMOSFETs are possible in the Icarus process. The source and channel of the device remain the same, but the drain is buried underneath the gate, eliminating abrupt changes in the geometry caused by the drain/gate overlap. Figures 60a and b show the CAD layout and its cross section, respectively. Experimentally, while the HV PMOS in Figure 58b has shown a breakdown voltage of -65 V, the vertical buried layer DMOSFET has demonstrated a breakdown voltage over -100 V.

3.6.2 High-Voltage Buffer

While many methods exist for driving electrostatic actuators (charge/voltage con-

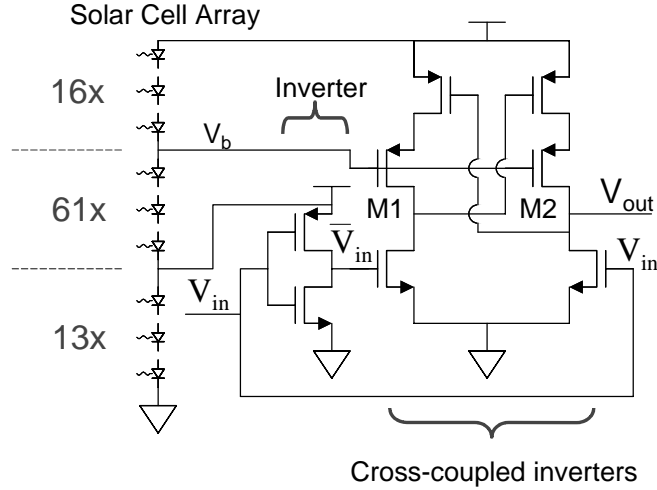


Fig. 61. Schematic of high-voltage buffer. The high-voltage buffer converts the digital signals from the sequencer chip (0 to 3.2 V swing) to voltages needed to run the actuators (0 to 50 V swing).

trol, adiabatic charging, inductive charging), we chose voltage control for its simplicity and ease of implementation. Ultimately, we designed the high-voltage buffer circuit in Figure 61. As will be described in Section 3.7, the output signals of the sequencer are digital signals with a 3.2 V swing. The HV buffer circuit first creates a complementary signal to the input, \bar{V}_{in} , and then both V_{in} and \bar{V}_{in} are input into a variant of a cross-coupled inverter. The circuit requires no static current to operate. While the output voltage swings from 0 to 50 V, the input voltage only needs to swing from 0 to 3.2 V.

To reduce the sizes of the NMOS and PMOS transistors, M1 and M2 are biased such that the pull-up current is limited. Since the solar cell array is composed of 90 cells connected in series, V_b could be set to almost any desired value by connecting it to any one of the individual solar cells. For additional flexibility, we used the top metal layer to connect to three possible voltages from the solar cells. We selected the desired voltage after fabrication and dicing of the Icarus chip by cutting the aluminum lines with either a probe tip or a laser.

To create the large voltages required to operate the actuators, 90 solar cells con-

nected in series were fabricated, producing an open-circuit voltage above 50 V. With a total effective area of 2 mm^2 , the solar cells generated over $100 \text{ }\mu\text{W}$ of power under solar illumination. In all, the high-voltage buffer chip contained 90 solar cells in series with 8 high-voltage buffers (4 signals per inchworm motor).

Lastly, the circuits would exhibit significant leakage current if exposed to light. Since we only had one metal layer, we could not use it as a light block. Instead, we used black commercial electrical tape diced into rectangles. Using a 5:1 reduced-motion manipulator, we manually placed the tape over the active circuits of the chip. The electrical tape can be seen in Chapter 4 in Figure 64.

3.7 Sequencer

As in the Smart Dust program, we chose to use a customized CMOS chip. A customizable chip allowed us to tailor the device specifically for the needs of the robot. A simple sequencer circuit was designed to operate the motors, but one could easily imagine adding additional computation for more complex behavior. The sequencer does not contain any sensors or communication subsystems. Instead, the open-loop sequencer automatically generates the walking sequence of the robot when power is applied. The chips were fabricated in National Semiconductor's $0.25 \text{ }\mu\text{m}$ five-metal layer process.

Since the operation of each of the GCA arrays of the inchworm motors is strictly on/off, the voltage signals generated can be digital. The sequencer has three basic functional blocks: 1) clock oscillator, 2) logic to generate the walking sequence, and 3) level shifters which convert the 1 V signals used internally to 3.2 V output levels.

A current-starved ring oscillator, designed by Warneke [49], provides the clocking source (Figure 62). A low-power current reference, based on [17], uses weak inversion concepts to limit the oscillator's total power to 22 nW. The current reference is based on

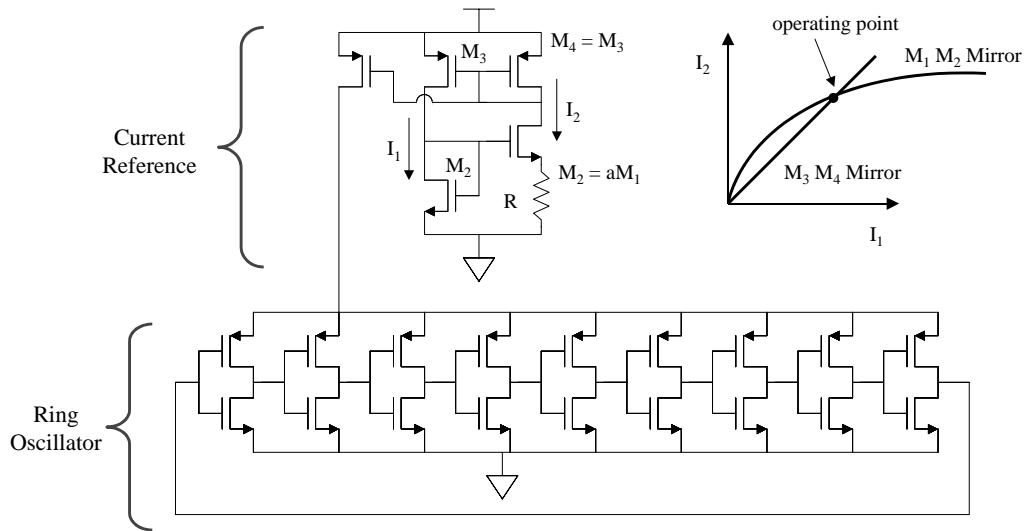


Fig. 62. Current-starved ring oscillator. Nine transistors form the ring oscillator. The current reference is formed by a complementary set of feedback-stabilized current mirrors.

complementary PMOS and NMOS current mirrors, which are feedback stabilized (Figure 62). Sizing M_3 and M_4 the same requires I_1 and I_2 to be the same. By sizing M_2 appropriately, a low-current stable operating point can be chosen.

As mentioned previously, the robot goes through four steps to complete a full walking cycle. During two transitions (between I->II and II->III of Figure 35), the sequencer logic generates the signals used to operate the inchworm motors through 64 inchworm motor cycles (not to be confused with walking cycles) during which the shuttle travels 256 μm . During the other transitions, the recoil springs behind the shuttles retract the legs passively. Figure 63 shows a simplified diagram of the sequencer circuit.

While the sequencer operates on a 1 V power supply, it has a power pin which is supplied by the solar cells (~ 3.2 V). This second supply provides level shifting, so that the output levels will be compatible with the input requirements of the high-voltage buffers on the Icarus chip. This 3.2 V intermediate voltage is sufficiently above the threshold voltage of the high-voltage buffers on the Icarus chip, and safely below the breakdown voltage of the devices on the sequencer chip to allow reliable operation.

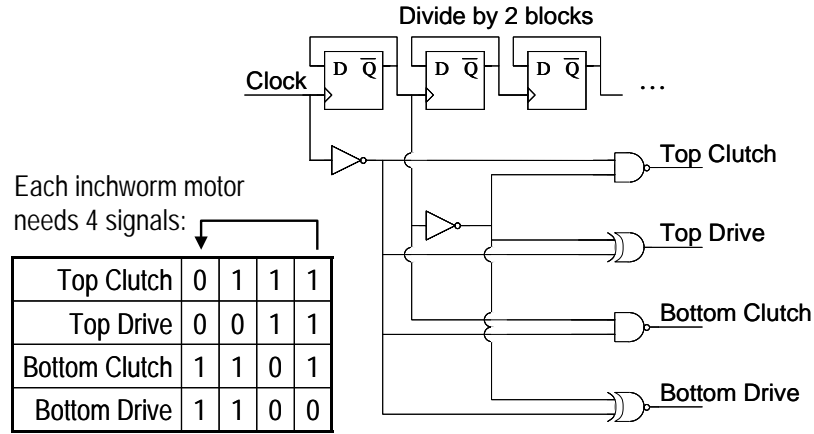


Fig. 63. Logic to generate inchworm sequence. The logic gates and flip flops generate the digital signals to operate of the inchworm motor.

In some situations it is possible to design circuits in low-power CMOS that exceed the typical operating voltage. In [2], Annema explains how circuit techniques can be used to limit oxide stress and hot-carrier degradation. Voltages up to 2.5 times the nominal supply voltage have been demonstrated. Furthermore, Ballan and Declercq explain how HV CMOS transistors can be fabricated in a standard low voltage CMOS process by violating traditional design rules [4]. In such a process, LDD extensions can be created from the transistor WELL and TUB implants. Furthermore, the polysilicon gates on top of the field oxide can act as field plates, limiting high voltage gradients. Breakdown voltages as high as 85 V have been demonstrated. Although we did not implement either of these techniques, they represent alternative methods to obtain high voltages.

As a last note, circuits exposed to light can exhibit relatively large leakage currents. This occurs due to light-generated minority carriers crossing PN junctions of the transistors. We use the top-most metal layer, not as a routing layer, but as a light block, to reduce total leakage current and allow 50 μm of overlap from the circuits to the edge of the metal layer. Although a large fraction of the light is absorbed before hitting the circuits, the generated hole/election pairs can still travel considerable distances before

recombining. To reduce recombination in the junctions of the transistors, we have added additional recombination sites in the form of a large unconnected substrate diode. The diode is not connected to power so it does not leak any current, but at the same time, it provides a much larger area for recombination than the actual circuits do. In theory, a substantial fraction of the generated hole/electron pairs should recombine in the diode as opposed to generating leakage current in the sequencer.

Chapter 4. Results

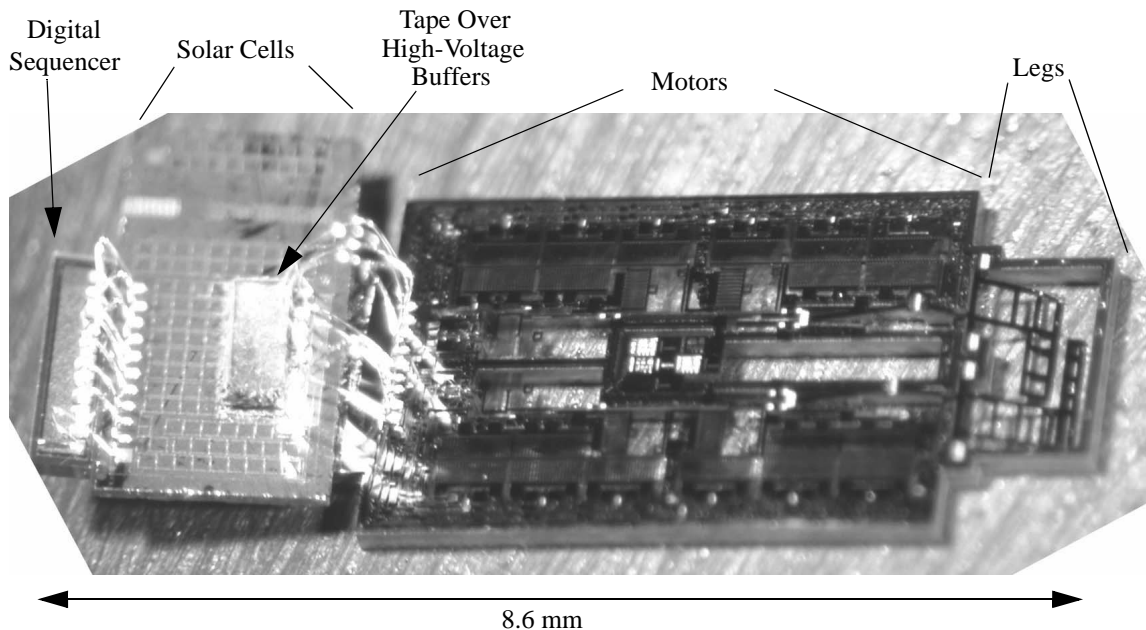


Fig. 64. Three-chip working robot. The digital sequencer outputs 3.2 V signals which are converted to 50 V on the solar-cell/high-voltage-buffer chip and sent to the robot chip to drive the electrostatic inchworm motors. The motors drive the legs via rigid links and pin-joint hinges to lift up the robot.

The final robot, after fabrication and assembly of the three chips, is shown in Figure 64. The total robot measures 8.6 mm in length and weighs 10.2 mg. The Iolanthe chip provides the frame for the robot with the legs and motors. The power is supplied by the solar cells and high-voltage buffers located on a separate chip. Lastly, the digital sequencer generates the signals to drive the motors. Before discussing the performance of the entire robot assembly, we will evaluate the individual components of the robot, beginning with the sequencer.

4.1 Sequencer Performance

Our initial sequencer chip design worked nominally at 22 nW. The oscillator frequency was down-converted to generate motor cycles on the order of 50 Hz that drove walking steps a little longer than one second each. However, when the sequencer was illuminated with about one-fourth the intensity of the sun, leakage current increased up to 300

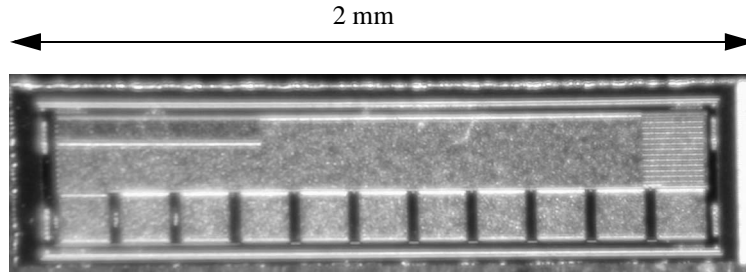


Fig. 65. Die photo of sequencer. Eleven bond pads connect to the Icarus chip: gnd, 2 power supplies and 8 motor signals.

nW. At this point, the leakage current swamped the current-starved oscillator, preventing it from functioning properly. For our experiments, however, we simply focused a light source on the solar cells but not on the sequencer chip, to the extent that that was possible.

A second sequencer chip was then designed with a larger current supply for the oscillator. We intentionally increased the power consumption, which eliminated the risk of light saturating the oscillator. This chip consumed about 200 nW of power in darkness, and when illuminated with about one sun (AM1.5 illumination), consumed close to 800 nW. This second sequencer continued to function under the strongest lighting environments.

4.2 Solar Cells, Transistors, and Buffer Performance

Both individual solar cells and solar cell arrays produced by the Icarus process were tested. Individual cells, equivalent in size to those used on the robot, $150 \times 150 \mu\text{m}^2$, have yielded efficiencies up to 14.3% under AM2.0 illumination. Efficiencies were calculated based on the method outlined in Bellew's dissertation [6]. Using sunlight and estimating light intensities based on date, time of day, and sun angle, one can calculate the actual light intensity fairly accurately.

Figure 66 shows an I-V curve of a 60-cell array fabricated in the Icarus process. The open-circuit voltage is over 30 V with 250 W/m^2 light intensity from an incandescent

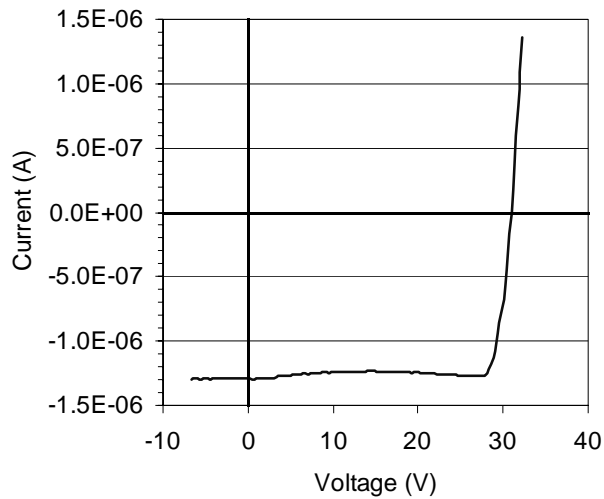


Fig. 66. Sixty cell solar array. The open-circuit voltage is greater than 30 volts on this array whose total area is 0.6 mm².

bulb. Each cell in this array measures 100 x 100 μm², yielding a total cell area of 0.6 mm². This represents over a 100% decrease in area over previously reported micro-solar cell arrays [see Section 1.5.3].

As a last experiment on individual solar cells, Piotr Prokop investigated the total energy generation of the solar cells in an outside environment. A 525 x 525 μm² solar cell was placed outside for a 24-hour period. I-V measurements were taken throughout the day, and the power was integrated over time to yield a total energy generated of 0.75 J/day.

4.2.1 Transistor Performance

Threshold voltages from the fabricated transistors were within 20% of those calculated with Avant! TSuprem-4. Breakdown voltages of the HV PMOS transistors ranged from -65 V to -100 V, depending on the design. Initially, HV NMOS transistors exhibited a nondestructive breakdown voltage of 42 V. However, repeated measurements at high voltages raised the transistors' breakdown voltages beyond 50 V. It is not clear why the transistors have progressively higher breakdown voltages when further tested. One possi-

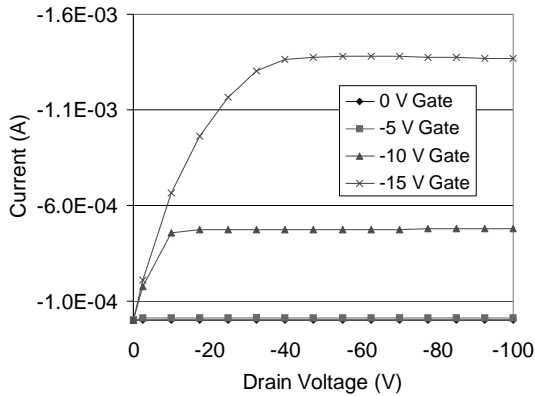


Fig. 67. I_d vs. V_d for circular PFET transistor. Using HP4145 transistor curves show that PFET does not breakdown at -100 V drain voltage.

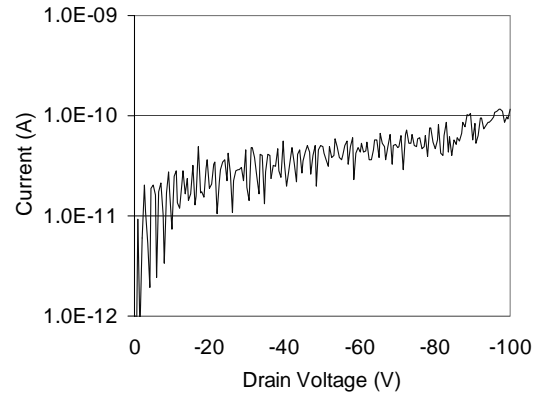


Fig. 68. Drain leakage current for zero gate voltage.

bility is that mobile ions in at the oxide interface may affect the electric field, and, in turn, high electric fields may cause the mobile ions to redistribute themselves.

Table 7 shows the transistor characteristics from the solar cell process for five types of transistors: gate-aligned NMOS and PMOS, LDD high-voltage NMOS and PMOS, and the vertical DMOS p-channel transistor. The unity-gain bandwidth, f_t , was calculated by estimating the gate capacitance. Junction capacitances were not included in the calculations.

Lastly, Figure 67 shows the transistor curve (I_d vs. V_{ds}) for the vertical DMOS transistor. The transistor exhibited breakdown voltages in excess of -100 V. Furthermore, Figure 68 shows the drain leakage current versus the applied drain voltage. At -100 V, the

Table 7: Transistor Characteristics from Solar Cell Process

	V_{t0} (V)	λ (1/V)	$K = \mu_o W/L C_{ox}$ ($\mu A/V^2$)	μ_o (cm^2/Vs)	g_m (1/ Ω)	C_{gate} (fF)	r_o ($M\Omega$)	f_t (MHz)
NMOS	0.94	8.0E-3	26	777	1.3E-4	5.5	0.38	83
PMOS	-3.6	3.9E-3	40	119	2.1E-5	5.5	4.5	14
HV NMOS	1.15	3.2E-4	7.9	524	2.3E-5	4.5	97	1.8
HV PMOS	-4.06	4.5E-5	1.2	71	5.9E-6	50	1540	0.42
Vert. DMOS	-3.97	3.5E-3	5.8	14	1.2E-4	69	0.8	6.0

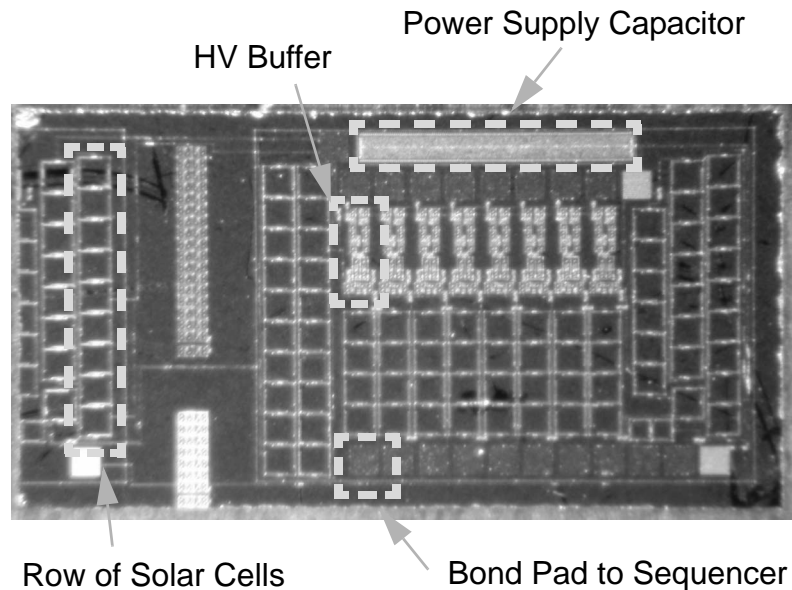


Fig. 69. Die photo of solar cell buffers. The die measures $1.8 \times 3.6 \text{ mm}^2$. Ninety cells in series produce 50 volts. The inputs at the bottom connect to the sequencer and are converted to 50 V signals using eight HV buffers.

drain leakage current was approximately 0.1 nA.

4.2.2 High-Voltage Buffer Performance

The high-voltage buffer chip weighed 2.3 mg, and its dimensions were $3.6 \times 1.8 \times 0.15 \text{ mm}^3$. The chip consisted of 90 solar cells in series; each cell measured $0.15 \times 0.15 \text{ mm}^2$ in area. The solar cell array generated over 50 V when illuminated with 250 W/m^2 of incandescent light.

While a power pad connected to the output of the 90 cells was not used to wirebond to the robot, it was convenient in testing the solar cells and robot in general. Most measurements were taken with an HP 4145 semiconductor parameter analyzer.

Figure 70 shows a plot of the input vs. output voltages of a high-voltage buffer, both measured and simulated. Possible discrepancies between the two plots could be attributed to the simplified transistor models (Level 1 Spice models) and the variation in threshold voltage.

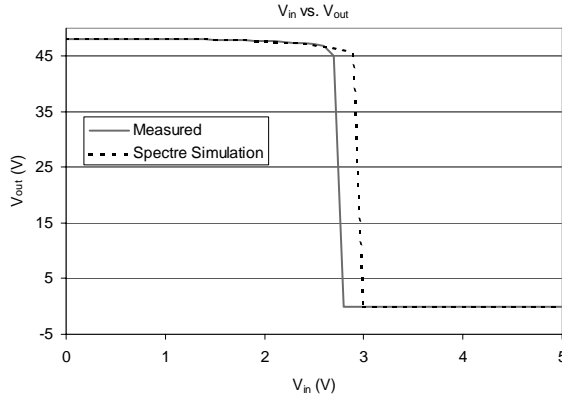


Fig. 70. Performance of voltage translator with a 48 V power supply. Simulated results were taken from Spectre using Level 1 models of the transistors.

Additionally, we both simulated and measured power consumption as a function of frequency for a single HV buffer connected to a robot's clutch actuator (Figure 71). The input voltage swing was 3 V and the output load was modeled with a 1.4 pF capacitance (1.0 pF parasitic capacitance and 0.4 pF load capacitance). Measured data show that 25 nJ of energy was required to charge and discharge the clutch actuator, yielding a charging efficiency for the system of 1.8%. The low efficiency of the buffer/actuator system can be attributed to a number of factors: parasitic capacitances of the actuator (67% loss), voltage control efficiency losses (50% loss), increased capacitance during actuation (67% loss), V_{dd} to ground path loss during voltage transitions (67% loss), etc.

On a further note, while black tape is used to block light from the transistors, some amount of light causes leakage in the circuit. About 40% of the power generated from the solar cells is dissipated through leakage current. Even after leakage, however, over 100 μW of power could be generated by the solar cells in full sunlight.

4.3 *Legs, Robot Motion, and Test Structures*

Evaluating the mechanical capabilities of the robot, we designed a number of test structures to examine the effects of hinge strength and silicon contact friction. Further-

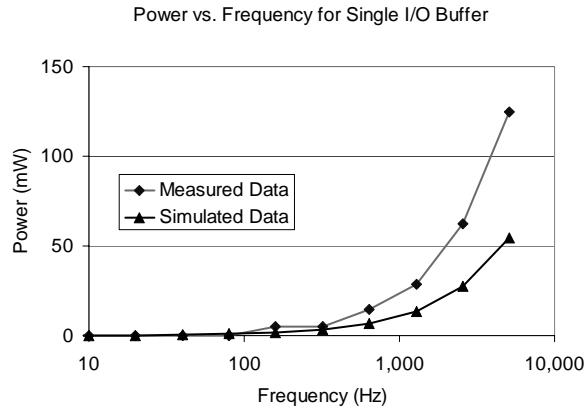


Fig. 71. Power consumption vs. frequency. A single high voltage buffer is loaded with a clutch actuator at 50 V. Measured data shows 25 nJ/cycle/actuator, simulated shows 11 nJ/cycle/actuator.

more, strength, speed, and endurance tests were performed on the legs before the final assembly of the robot. While most testing pertained to the robot, additional structures were designed to demonstrate the capabilities of the process. Among these structures were bidirectional motors and torsionally hinged legs.

4.3.1 Slider Friction and Hinge Strength Tests

By adding polysilicon flaps to constrain the motor shuttle, we introduced a possible source of adhesion and friction to the motor design. Yeh demonstrated in friction tests of polysilicon on nitride that the force required to slide a shuttle along the substrate and rotate an unloaded hinge was between 1 μN to 43 μN , which is much greater than the weight of the lever arm (3.2 nN) [58].

To test the amount of static friction an inchworm motor must overcome to move the shuttle, we designed simple SOI sliding test structures attached to polysilicon vernier springs (Figure 72). The test structures were designed both with and without substrate underneath. This allowed us to compare sliding polysilicon flaps along SOI to sliding an SOI beam along the silicon substrate.

A histogram of the force required to overcome static friction and adhesion in each

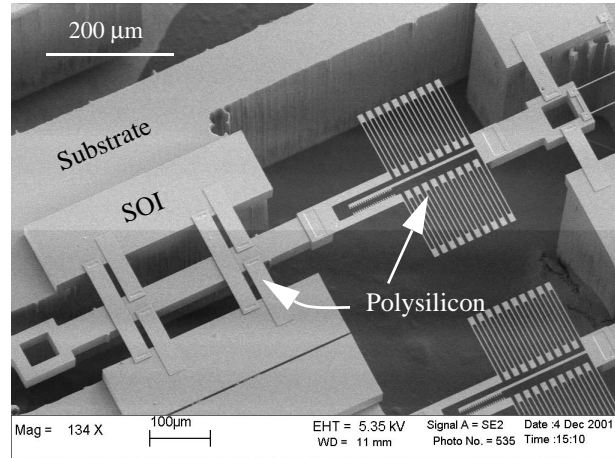


Fig. 72. SEM of the sliding test structure. A vernier spring was used to measure the force required to move polysilicon flaps over the SOI device layer.

of the test structures is shown in Figure 73. Force required to move the SOI beam ranged from 0.5-13 μN with substrate and 0.5-15 μN without substrate. Peak value recurrence for both sliding structures was between 1-3 μN .

It is important to note that there are several data points not included in this graph. After storage of the test structures in normal laboratory conditions for approximately one month, sliders with polysilicon flaps required forces much greater than the vernier springs could measure ($\gg 25 \mu\text{N}$). This was probably due to adhesive forces from ambient moisture and will likely need to be addressed in future robot design and testing. Future solutions could incorporate self-assembled-monolayers (SAM) to reduce the adhesive forces.

All of these frictional forces were considered in the overall robot design. In order to provide enough force to lift the robot, we designed the inchworm actuators to output over 200 μN of force. This force takes into account the approximate weight of the robot ($\sim 100 \mu\text{N}$), the mechanical advantage of the linkages (~ 1), and the frictional and adhesive forces of the flaps ($\sim 20 \mu\text{N}$).

Fracture strengths of the pin hinges (like those seen in Figures 50, 51, and 74) were also measured to verify their robustness. According to simple models, Sarah Bergbreiter

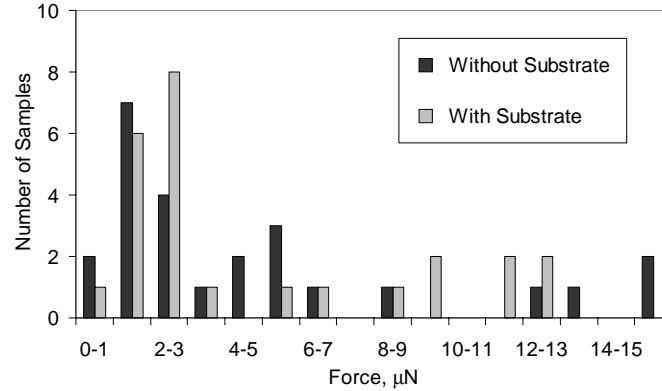


Fig. 73. Force measurements taken from the sliding friction test structures. A mean force of 4.6 μN and median of 2.5 μN were the same for sliders with and without a substrate.

determined that the polysilicon hinges could withstand over 1 mN of force. We used test structures like the one in Figure 75 to load the hinges with vernier springs. Probe tips were used to pull one end of the spring which, in turn, applied a load onto the hinge. Due to a layout error, we designed the vernier spring with a maximum force of 0.5 mN. All the hinges, therefore, were tested with loads up 0.5 mN, and none of them fractured.

On one- and two-DOF legs, we accidentally broke some hinges. This allowed us the chance to observe what part of the hinge broke. In these instances, the hinges would fracture in three basic ways. First, the pins of the hinges would stay intact and the staples (POLY2 layer) would pop off the SOI device layer. Secondly, in designing the hinges, the

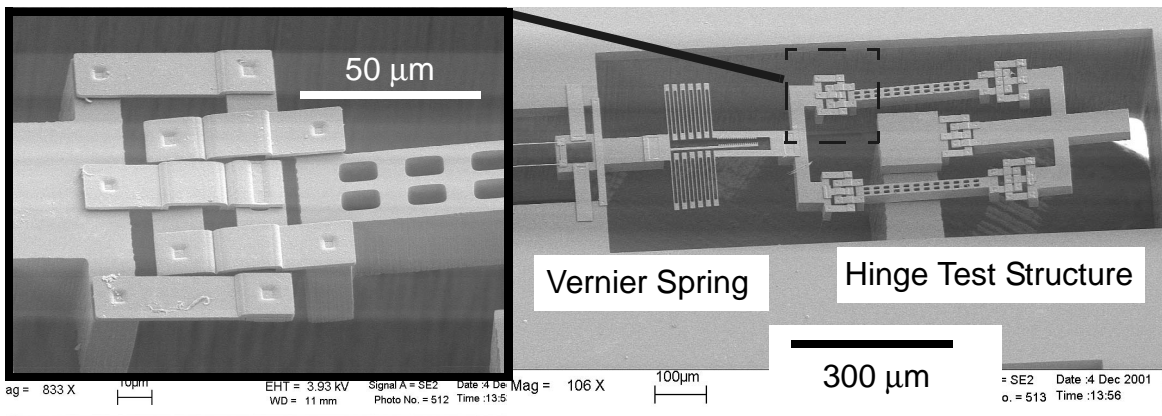


Fig. 74. SEM close-up of poly-Si scissor hinge on SOI beams.

Fig. 75. SEM hinge test structure. Probes are used to pull the vernier spring to test breaking strength of the hinge structure.

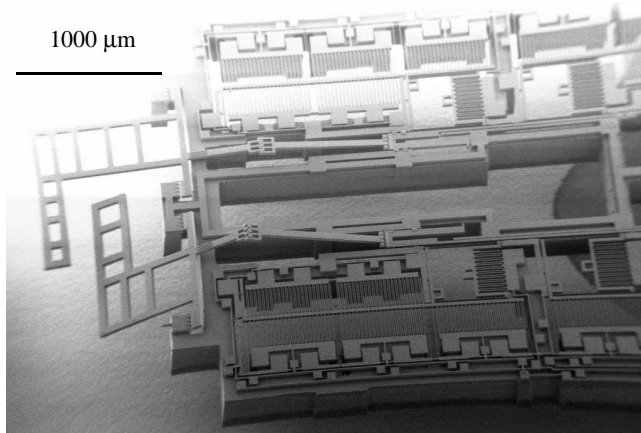


Fig. 76. SEM of released legs, motors, and robot frame. First legs design did not incorporate rollbars.

pins were made from the POLY1 layer and subsequently connected to the POLY2 layer via the CONT mask. The connection from the POLY1 layer to the POLY2 layer would also fracture. This was most common at the “hip” joint of the robot (Figure 50). Lastly, the pins (POLY1) underneath the staple would fracture.

4.3.2 One-DOF Leg Performance

Before assembling the full microrobot, we tested the Iolanthe chip, which consisted of the robot frame, motors, and legs. SEM images of the fabricated Iolanthe chip can be seen in Figures 76, 77, 78, and 79. Motors were actuated using a programmable Atmel AVR microcontroller whose I/O pins interfaced to an Analog Devices AD8600 16 Channel DAC. Amplifiers on the channels converted the 5 V maximum outputs of the DAC to a maximum possible 160 V output. The inchworms were limited to 65 V, however, because of electrostatic pull-in of the GCA fingers. The programmability of the test setup allowed us to troubleshoot the inchworm motors and characterize the speed of individual steps of the inchworms.

Each motor we tested measured 700 μm x 4 mm. The motor was calculated to maintain a force of at least 400 μN at 50 V. Before testing the shorter leg, we preset the

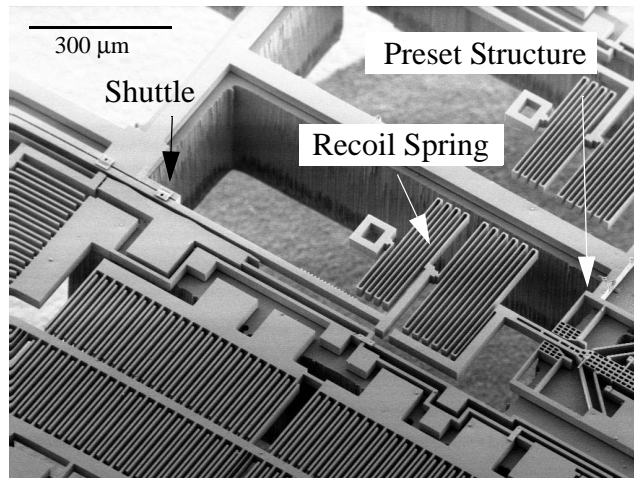


Fig. 77. SEM: Shuttle, recoil spring, and preset structures. These structures are located near the back of the inchworm motors.

shuttle by $150\ \mu\text{m}$ using the latch structure in Figure 77. This gave the leg an initial starting angle of 34° relative to the plane of the motor (Figure 78). In our original design of the legs, a complication arose because of a design flaw in the motors: the gap, g_f , of the clutch GCAs was drawn too small (Section 1.2). The resulting fabricated motors exhibited shorting of the gap fingers when the clutch was actuated. While some leg motion was demonstrated, we redesigned the legs for the next fabrication run. In this design, we determined adequate spacings of the fingers and backstops based on the lateral etch of the SOI device layer (see Section 3.3.1).

With the slightly modified fabricated legs, we demonstrated both legs working at shuttle speeds of $4\ \text{mm/sec}$, over 100 times, with no failure. Each leg swept through 30° of motion yielding an angular rotation rate of $480^\circ/\text{sec}$ (see Figure 80). Force measurements were also taken from a vernier spring gauge from MEMS Precision Instruments [30]. Based on the actuated displacement of the spring, we back-calculated the force exerted at the tip of the leg. Force measurements have shown that the long leg produced from $30\ \mu\text{N}$ to $60\ \mu\text{N}$ of force when the drive and clutch voltages of the inchworm motors were $32\ \text{V}$ and $50\ \text{V}$, respectively. The wide measurement range may be due to the low

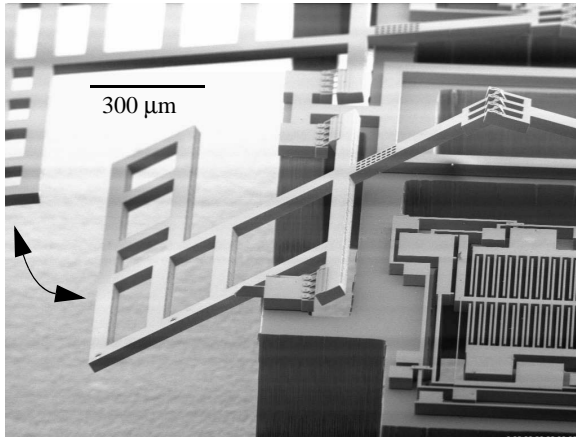


Fig. 78. SEM of robot leg in preset condition. Leg was actuated through almost 30° of angular deflection.

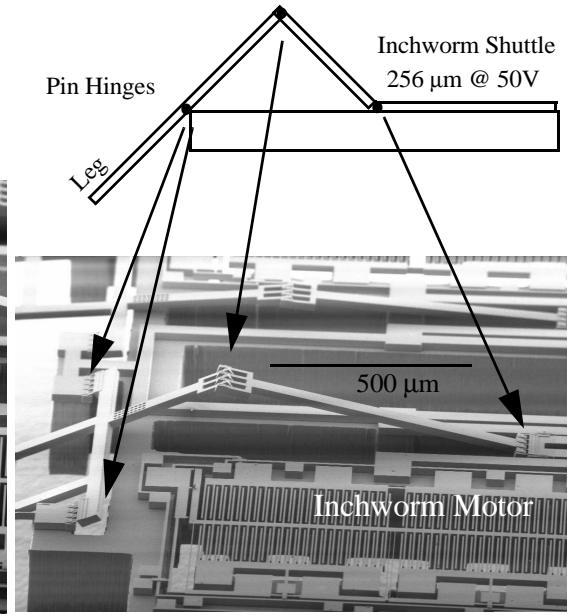


Fig. 79. Kinematic diagram of robot leg and SEM of linkage structure. Arrows are used to show the position of hinges relative to the diagram.

spring constant of the gauge ($0.15 \mu\text{N}/\mu\text{m}$) which caused the leg to jam on the vernier spring over wide sweeps.

Nevertheless, we were able to map out a relative force space of the long leg for given drive and clutch actuation voltages (Figure 81). The force increases for increasing drive voltages up to a point, and then decreases. As the clutch voltage increases, the peak of the force curve shifts to the right, indicating the peak force is at a larger drive voltage. This pattern indicates that the inchworm motor's clutch is slipping. For low drive volt-

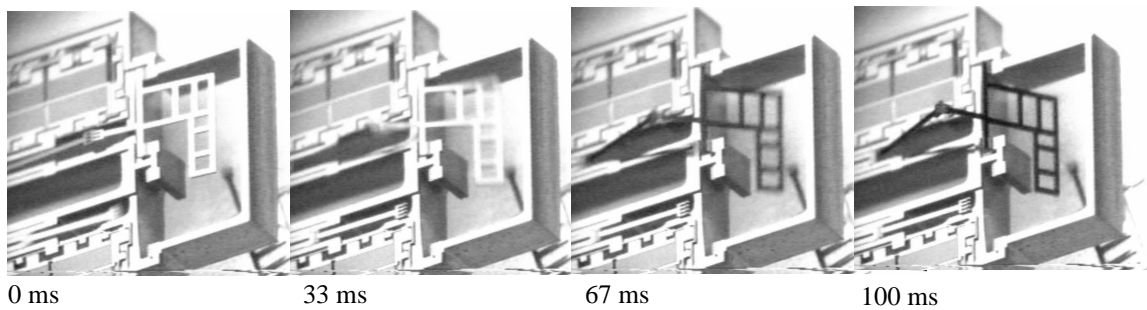


Fig. 80. Robot leg being driven by external controller. With 30 V drive and 42.5 V clutch signals, the shuttle is driven at 4 mm/s, sweeping the leg through 30° degrees in 100 ms.

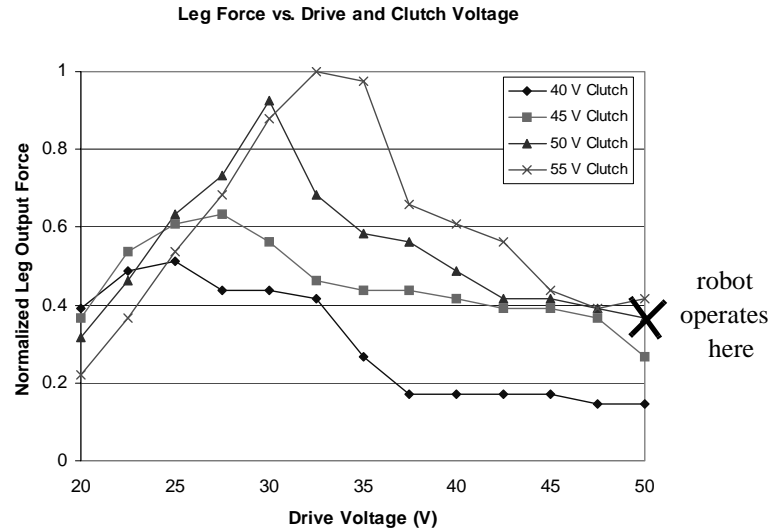


Fig. 81. Relative force vs. clutch and drive voltages for long leg.

ages, the force the leg can exert is limited by the force the drive actuators can produce. At very high drive voltages the degree of clutch-shuttle slipping increases and thus the leg's output force decreases. As the clutch actuation voltage increases however, the clutch engagement strength increases, increasing the peak force which the leg can exert.

Because of the design of the robot, however, the robot operates at a 50 V drive and 50 V clutch voltage placing it at the lower end of the force curve in Figure 81. Without clutch/shuttle slipping, the force output should be on the order of 400 μ N, a distant cry from the forces we have previously measured. We have not determined the cause of the clutch/shuttle slipping. We briefly discussed tooth shape in Section 3.3.2 and related it to the force at which the teeth engage. Furthermore, we have not applied a dynamic model to the engagement and subsequent drive actuation. One possibility is to model the interaction as an elastic collision where the clutch gains kinetic energy before the teeth engage. After the "collision" or engagement of the teeth, an immediate momentum could be imparted on the clutch pushing it away from the shuttle. Since the initial kinetic energy would depend on the drive voltage, one would expect higher drive voltages to increase the

Table 8: Robot Properties

	Mass (mg)	Dimensions (mm x mm x mm)	Power Consumed
Robot Frame (Iolanthe)	6.4	8.6 x 3.1 x 0.3	100 nW
Voltage Translators	(incorporated into solar cell chip)		2.5 μ W
Solar Cells (Icarus)	2.3	3.6 x 1.8 x 0.15	100 μ W *
CMOS Sequencer	0.5	0.56 x 2.05 x 0.2	22 nW
Robot	10.2	Same as Iolanthe chip	2.6 μ W

*estimated power generation in full sunlight

frequency of slipping.

Future fabrication runs could include design variations of both the teeth geometry and the clutch actuator. Tooth designs that had deeper insets and were slightly angled could change the contact angle of the shuttle and clutch. A contact angle perpendicular to the shuttle could reduce the force against the clutch and consequently the frequency of slipping.

4.3.3 Solar Powered Robot

The robot was assembled based on the protocol outlined in Section 2.4. Table 8 shows the measured properties of the robot as a whole. The largest component of the 10 mg robot's mass is the Iolanthe die, the robot frame. The total power consumption is less than one tenth of the available power from the solar cells in full sunlight. In terms of energy, the robot consumes 13 μ J per walking cycle.

After assembly of a robot, the tethers on the legs were broken (using probe tips or a laser), and the legs were positioned out-of-plane with the preset structures. Sometimes particles from the wax release would settle in the trenches of the inchworm motors and short out the actuators. By applying a high current from the actuator pad to ground, we

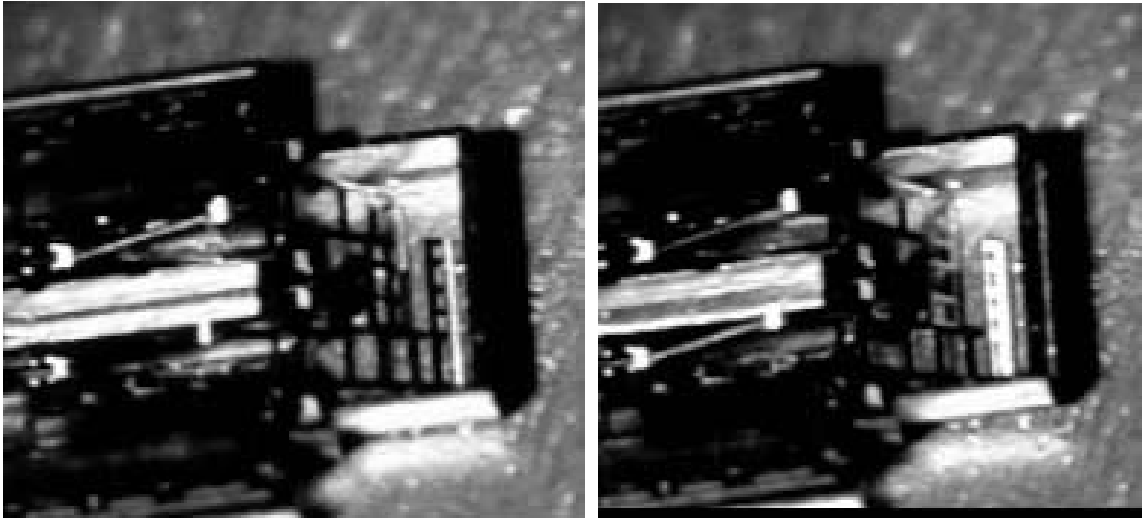


Fig. 82. Video of shuffling robot. a) Robot initially rests on surface before going through walking motions.

b) Robot lifts its front $300\ \mu\text{m}$ in the air. Legs slip on surface; so instead of going forward, the robot shuffles to the right a few millimeters.

could burn out these shorts. Generally, we would use the HP4145, setting it to 50 V with a current clamp of 20 mA. These settings generated enough power to burn out particles, yet not enough power to overheat the probe tips on the silicon. If particles were too large to be burnt out, they would heat up enough to emit visible light. By turning off the microscope light, we could see the particles glowing. Using a probe tip, we could maneuver the particle out of the way to prevent further shorting.

After removing any possible short circuits, we illuminated the robot with light to operate the motors. We used a fiber-optic gooseneck light to illuminate the solar cells beneath a stereo microscope. Suspended off the ground, all the robots demonstrated leg motion. When first actuated, sometimes a clutch would stick to the shuttle preventing the other clutch from pulling the shuttle forward. This problem seemed to alleviate itself after running the motors for half an hour. With a sticking clutch, the shuttle could only travel a fraction of its $256\ \mu\text{m}$ -travel length. Over the course of running it, though, the shuttle would travel farther and farther as the clutch became less “sticky.” Eventually, the shuttle

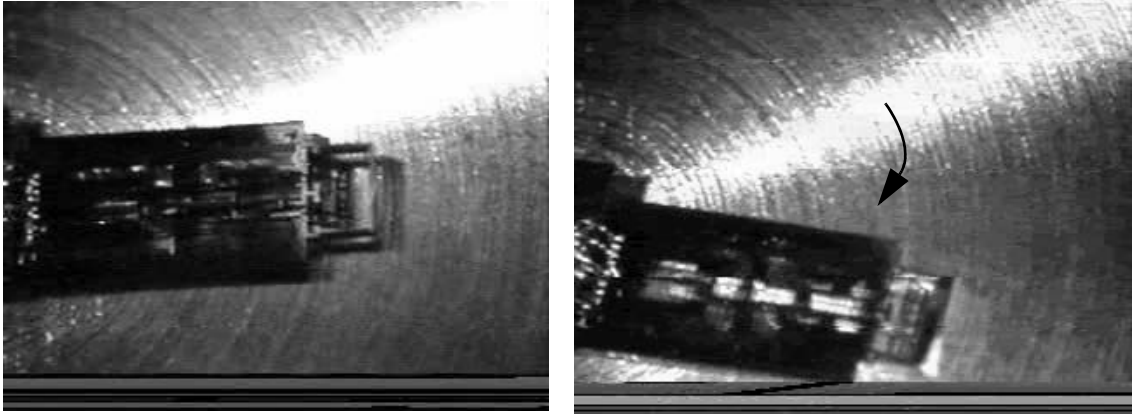


Fig. 83. Video of robot trajectory. In about 8 minutes the robot shuffles to the right about 3 mm.

would operate, going through the entire leg cycle without skipping any steps.

To date, seven fully assembled robots have demonstrated autonomous operation. With the robots suspended in the air, the legs operated as expected, according to the walking sequence described previously. When placed down on a surface, 4 of the 7 robots were able to lift their front ends under autonomous operation. Three robots we tested lifted themselves up repeatedly with just the short leg working. Without their second leg contributing, they performed “one-armed push-ups” to a height of over $300\ \mu\text{m}$ above the surface (Figure 82). The seventh robot lifted itself up with both the short and long legs, and went through walking motions dragging its back end for approximately 250 cycles. Instead of going forward, however, this robot would slowly veer to the right as its feet slipped on the surface. In one test, the robot shuffled to the right 3 mm over 30 minutes, and in another test, the robot shuffled to the right the same distance in 8 minutes (Figure 83). A $60\ \mu\text{m}$ step was observed in one instance while the robot was walking on aluminum. In all, the robots lifted themselves up on four different surfaces: 1) polished silicon, 2) teflon-coated polished silicon, 3) conductive plastic of a chip tray, and 4) polished aluminum.

However, the four self-lifting robots did not function indefinitely. After a few

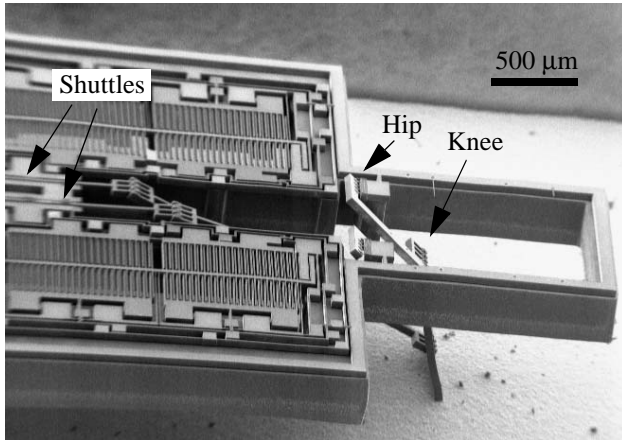


Fig. 84. SEM of two-DOF leg. Leg is folded down touching the bottom of the die package.

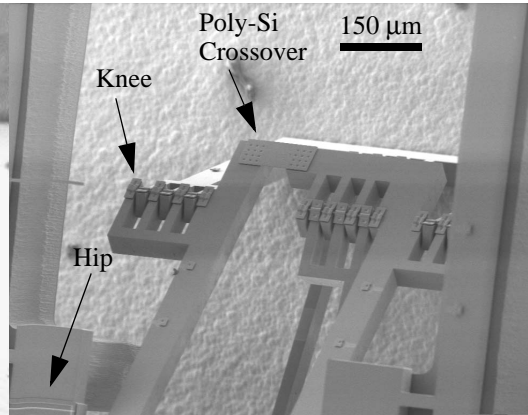


Fig. 85. SEM close-up of knee joint. Hinges comprise the joint connecting the legs and tendons together. Polysilicon cross-overs are used to bridge mechanical components.

hours of operation, they stopped lifting themselves up. They ultimately failed due to clutch/shuttle slipping. We were unable to determine whether surface chemistry was reducing clutch/shuttle adhesion or the teeth were physically wearing down. Attempts to dry the robot out through heat or in a desiccating chamber did not increase adhesion between the clutch and shuttle. Future work could include adding adhesive agents such as HMDS (Hexa Methyl Di Silazane) to promote engagement of the clutch and shuttle.

In summary, seven robots were assembled and demonstrated leg motion while suspended. Four were able to overcome their weight and push themselves off the ground. Lastly, the seventh robot demonstrated pseudo walking motion, shuffling to the right a few millimeters.

4.3.4 Two-DOF Leg Performance

While we have designed and built a robot with one-DOF legs, we also wanted to demonstrate that many other 3D structures could be fabricated using the Iolanthe process. As an example, we fabricated a two-DOF leg operated with the same external controller (Figure 84). The segmented leg is 1 mm long and driven by two electrostatic inchworm

Area Swept out by Two-DOF Leg

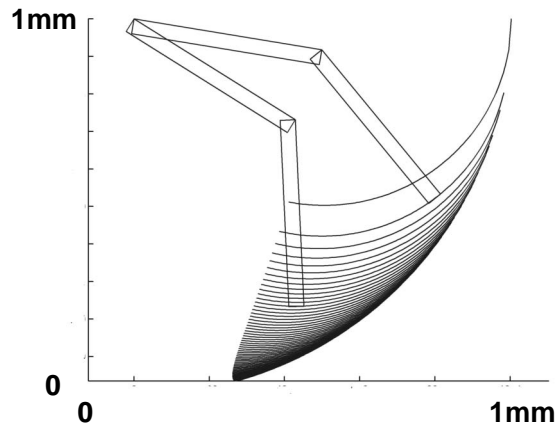


Fig. 86. Area swept out by two-DOF leg. Lines represent sweeps of lower leg at a fixed upper leg position

motors. The entire device measures $6 \times 3 \text{ mm}^2$. The leg is composed of a “hip” joint and “knee” joint (Figure 85). Each joint was exercised with at least 90° of static angular deflection. The area swept out by the foot of the leg is more than 0.1 mm^2 (see Figure 86). Each inchworm motor was designed for, and has demonstrated, a shuttle displacement of $400 \text{ }\mu\text{m}$ with speeds up to 6.8 mm/s - a 70% improvement over previously reported results [57]. At this shuttle speed, the leg experiences an angular velocity of $1530^\circ/\text{s}$. The inchworm motor was driven using a 40 V drive and 50 V clutch actuation voltage. Reversing the leg motion was accomplished using the scheme outlined in Section 3.3.3.1. Reverse operation tests yielded nearly identical speeds to forward operation. In forward operation, the foot of the leg has exerted from $6 \text{ }\mu\text{N}$ to $33 \text{ }\mu\text{N}$ of vertical force, depending on the angle of the joints. The leg exerted larger forces the more it was deflected out of the plane. Smaller leg angles saw correspondingly lower forces. In another test, the leg was visually undamaged after 60,000 full leg sweeps for 16.5 hours of operation (~ 10 million inchworm cycles).

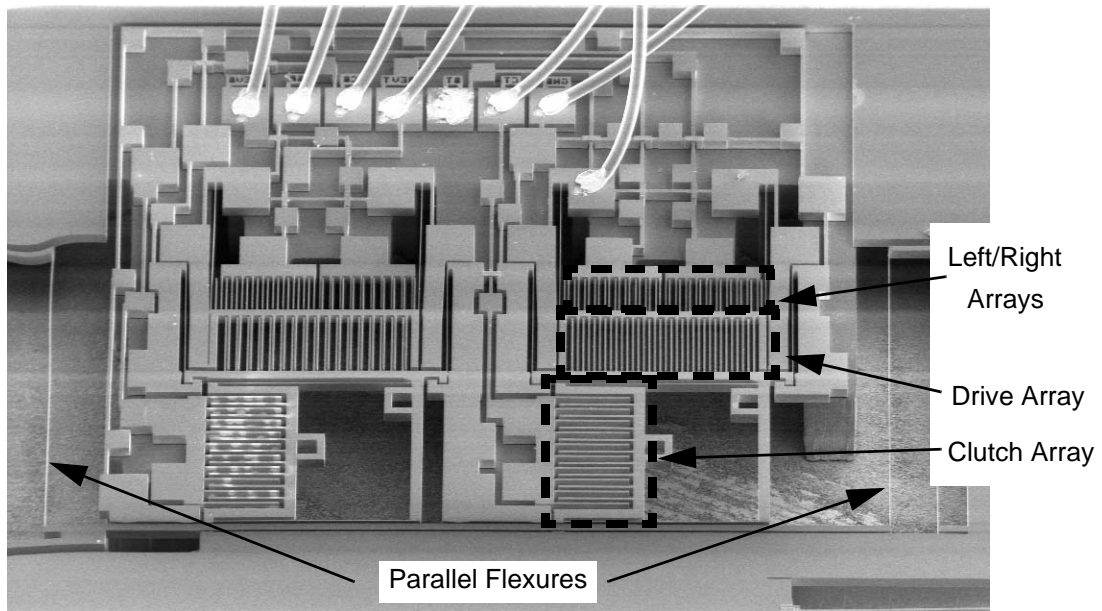


Fig. 87. Bidirectional motor. The left/right GCA arrays slightly bias the drive frame one way or the other to cause the drive actuator to go forward or backward.

4.4 Other Structures from the Iolante Process

In addition to demonstrating one- and two-DOF legs with pin hinges in the Iolante process, we have also fabricated other devices, including a bidirectional inchworm motor and a torsionally hinged leg.

4.4.1 Bidirectional Inchworm Motor

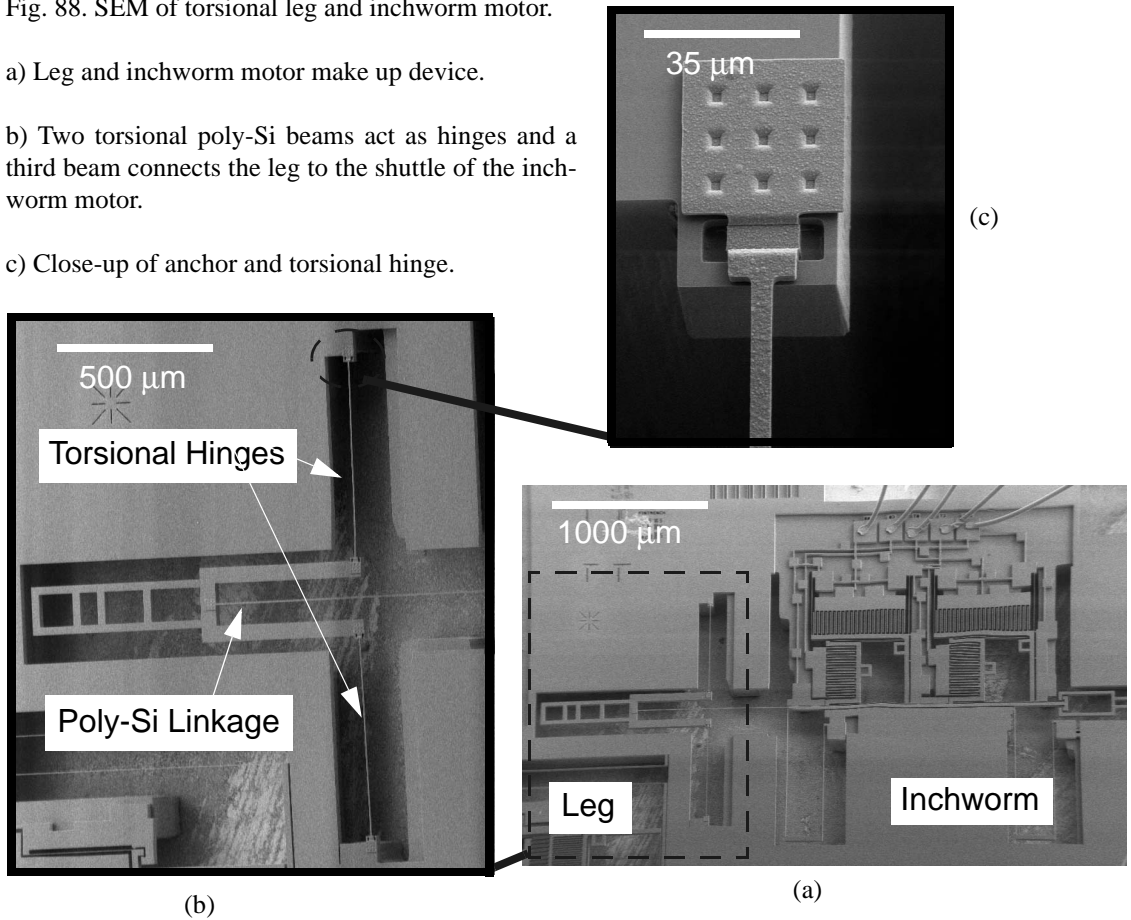
We have designed and tested a bidirectional inchworm motor (see Section 3.3.3.2). Because this design was a test structure, the shuttle is suspended by a set of parallel flexures rather than driving a leg (see Figure 87). The motor was fabricated in an area $1.9 \times 1.6 \text{ mm}^2$ and demonstrated both right and left motions at speeds up to 5.5 mm/s with a total travel of $224 \text{ }\mu\text{m}$ in each direction. The motor was controlled by an external controller with positive voltages and 8 steps per cycle. The inchworm motor was driven with a 40 V drive and clutch actuation voltage, and 20 V right/left actuation voltage. With a shuttle spring constant of $0.07 \text{ }\mu\text{N}/\mu\text{m}$, the maximum load on the motor was no more than

Fig. 88. SEM of torsional leg and inchworm motor.

a) Leg and inchworm motor make up device.

b) Two torsional poly-Si beams act as hinges and a third beam connects the leg to the shuttle of the inchworm motor.

c) Close-up of anchor and torsional hinge.



8 μN.

4.4.2 Torsionally Hinged Devices

Even though torsional devices were not mentioned in Chapter 3, we fabricated and tested a one-DOF leg. The leg was designed using polysilicon torsional hinges. The fabricated results are shown in Figures 88a, 88b, and 88c. A $2 \times 1 \text{ mm}^2$ inchworm motor was used to drive the leg. Polysilicon was used as the link connecting the shuttle to the leg. A special double layer of POLY1 and POLY2 was stacked during fabrication to yield a thickness of 4.5 μm for the torsional hinges.

The leg was tested without presetting the shuttle. Because the chip was bonded to a die package, the leg physically stopped on the surface below it, actuating 14° for a total vertical distance of 260 μm . During that actuation, the inchworm went through 8 cycles,

translating the shuttle 32 μm . The maximum shuttle speed was 1 mm/s, yielding a leg rotation rate on the order of 470 $^\circ/\text{s}$.

Chapter 5. Conclusion and Future Work

Combining commercial CMOS and two in-house processes, we have established a framework for making milligram-sized mobile robots. To demonstrate the capabilities of this framework, a solar-powered, milligram prototype robot was designed. A set of seven microrobots was successfully fabricated and assembled. Although all seven were functional, only four could lift one side of their frames. One microrobot achieved a shuffling action, dragging itself to the side a few millimeters. While this shows that microrobots are feasible, additional work is required for the development of more actuation force in the robot legs. This, coupled with the potential of putting four two-DOF legs on a robot, may lead to walking microrobots that can demonstrate a number of gaits from scuttling to running. Furthermore, newer process developments could enable the robots to be fabricated with higher yield in a more integrated process.

5.1 *Four-Legged Robot Concept*

Biological evolution has experimented with most locomotion designs, and we can learn from these systems in the creation of more robust, efficient robot body plans. With intelligent use of available microrobot technology, important features from biology can be incorporated into microrobots. Both Raibert [41] and Quin *et al.* [40] reported on a number of large robots with various gaits for self-locomotion, some of them derived from animal locomotion. Perhaps, the most statically stable and easiest to control among the walking robot designs is a six-legged robot. Two interpenetrated tripod gaits allows for a very stable crab-like walk. Like large robots, our fabrication process favors some designs over others due to the inherent limitations of the process. In our case, the inchworm motors are responsible for the majority of the robot's weight. Therefore, it is desirable to reduce the total number of actuators at the expense of some stability.

One robot design that can demonstrate a number of gaits but does not have an excessive number of joints is a four-legged robot with two-DOF on each leg. The simplest stable motion would be a static walking gait in which three legs are on the ground at any one time. By maintaining a strictly horizontal motion while walking, the inchworm motors can be decoupled from the weight of the robot. For a flexible robot design, however, one would also want the robot to lift itself from the ground. This could be done by actuating all four legs at once, reducing the load on each leg to just a quarter of the weight of the robot.

We outline the basic parameters to design this robot while employing the same fabrication steps as was used for the two-legged, prototype robot. Depending on the application of the robot, one could optimize any number of parameters, ranging from power to size. In this case, our four-legged example is optimized for low mass while maintaining a speed of 4 mm/s. Two inchworm motors would be required to operate each two-DOF leg. The motors could also be asymmetrically sized so that only one motor was used to drive the leg while contacting the ground. In this case, one motor outputs only enough force to move the leg while it is in the air, and the other motor is sized to handle only one quarter of the weight of the robot while the leg is on the ground. Using the results from the Chapter 4, we modified the model in Section 3.2 to estimate the size, power, and layout area of the robot. In addition to force calculations, the modified model uses results from Chapter 4 to assess more accurately the properties of the four-legged robot. Among the additional factors for modeling the robot, we took into account leakage current from solar illumination, 1.8% efficient buffer/actuator pairs, and varying solar cell areas for increased power demand. The resulting four-legged robot properties can be found in Table 9 along with an optimized two-legged robot for comparison. In this case, the layout area of the 4-legged design would be approximately 47 mm^2 . It turns out that the minimum practical size of

Table 9: Estimated Properties for Multi-Legged Robots

Robot Type	Mass (mg)	Total DOF	Power Consumption at 4 mm/s (nW)	Iolanthe Die Area (mm ²)	Icarus Die Area (mm ²)	Jupiter Die Area (mm ²)
2, 1-DOF Legs	5.3	2	72	11	4.0	1.0
4, 2-DOF Legs	23	8	340	47	21	1.7

the inchworm motors ($1.6 \times 1.3 \text{ mm}^2$) provides just enough force to generate locomotion (motor energy density of 133 pJ/mm^2). The maximum speed of the robot is affected by two factors. The first factor is the speed/force trade-off within the inchworm motors. We estimate, however, that the inchworm's relative low impedance allows it to operate at near high speeds with and without loads. The other limiting factor is the availability of power. For an optimal design, the solar cells would be just large enough to generate enough power at the maximum speed. In full sunlight, the solar cell chip area would be 21 mm^2 . The digital controller contributes a small fraction of the whole robot's mass - only 3%.

In fabricating and assembling such a robot, we would need at least 33 bond pads on the Iolanthe die, 68 bond pads on the Icarus die, and 35 bond pads on the CMOS controller for a total of 68 wires. This could be reduced almost by half if we installed a three-wire communication protocol between the Icarus chip and the CMOS chip. The transistors on the Icarus die, however, are relatively large ($5 \text{ }\mu\text{m}$ gates) and will increase the area of the active circuits.

From a research standpoint, the very problem of such a design is yield. Only a small percentage of the prototype robots survived fabrication and final assembly without damage. Increasing the complexity and size of the design can only detrimentally affect the yield. We have observed, however, that a stabilized process protocol and improved quality control resulted in a corresponding increase in the yield of the microrobots.

5.2 *Integrated Robot Process*

Another way to optimize robot design is to change the fabrication process. This is especially important in improving yield and reducing cost. In this dissertation, we have described a hybridized robot. Final assembly was accomplished by gluing the robot chips together and wirebonding 20 wires. While we assembled the chips manually, one could use automated pick-and-place tools to assemble the robots or even fluidic self assembly both to assemble and to provide interconnect [43]. As in the case of the four-legged robot concept, more interconnects are needed to interface between the chips. An automated wirebonder can accomplish this task, but the sheer number of the pads may substantially affect the cost, yield, and the available silicon real estate used for the robot itself.

In a monolithic approach, all the robot subsystems (i.e., legs, motors, CMOS, solar cells) would be fabricated in a single process. This would bypass the assembly step and remove the need for wirebonding chips together. A major obstacle is the establishment of a standard process with enough design flexibility. It has taken nearly 25 years for the semiconductor industry to develop standard processes for digital circuits: how long would it take to establish a standard microrobotic process?

Still, technologically, fabrication of microrobots in a single process is perfectly feasible. As an example, let us consider a hypothetical process in which we merge the Iolanthe process and the Icarus process into one. Bellew has already demonstrated that trench isolation could be performed as the first step in the process [6]. For CMOS devices, the high-temperature drive-in steps, ion implant steps, and gate deposition and patterning could be performed next. Then, a structural etch could form the inchworm motors in the same SOI device layer as the transistors. The planarization step is more complicated. If the wafers were polished to the glass/SOI interface using CMP, the polysilicon gates and implanted junctions would be destroyed. Therefore, CMP of the glass

would have to be controlled to stop within a few microns of the surface. This has been achieved in today's commercial semiconductor industry. Furthermore, with enhanced lithography (smaller linewidths), the optimized thickness of the SOI device layer would also decrease (see Section 3.3.1). The thinner SOI device layer could be planarized using methods similar to the interconnect industry's planarization of multiple metal layers. Further reduction of the lithography both lightens the robot and reduces the force demand. The robot, however, cannot be designed arbitrarily small. At some point in the micron to millimeter range, capillary and van der Waals forces dominate over the electrostatic forces of the inchworm motors, limiting the minimum size of the robot [14].

Once planarized, the process of depositing layers of polysilicon and metal are relatively simple. Before a release of the mechanical structures, the circuits would need to be protected from HF. Bellew used germanium as an HF resistant barrier. Other possibilities include chemically resistant polymers such as CYTOP™.

This hypothetical monolithic process does not present any major technological hurdles. Establishing a detailed and robust process flow is likely tedious and will take some time. As Benjamin Franklin once said, however, good ideas are "10% inspiration and 90% perspiration." The practicality of developing microrobots is truly dependent on the vision of their creators and sponsors. The level of interest, development of real-world applications, and financial support will ultimately decide the time frame for when microrobots enter the world as an accepted technology.

Using a hybridized approach, we have demonstrated mobility, power, and computation in a prototype microrobot. Additional work is needed to create multi-legged walking microrobots. With the establishment of a flexible foundation for creating robots either in our fabrication process or in newly adapted processes, the future of multi-legged

microrobots with microprocessor-based intelligence, sensors, and communication will fast become a reality. While the semiconductor industry looks upon each of their wafers as thousands of small integrated chips, we look upon each of ours as a colony of microrobots. We look forward to these colonies of robotic insects scurrying about looking for something to do.

Bibliography

- [1] D. Adkins, E. Heller, <http://www.sandia.gov/media/NewsRel/NR2001/minirobot.htm>, Sandia National Laboratories, accessed May 2002.
- [2] A. Annema, G. Geelen, and P.C. de Jong, "5.5-V I/O in a 2.5-V 0.25 μ m CMOS technology," *IEEE Journal of Solid-State Circuits*, vol.36, no.3, March 2001.
- [3] M. Ataka, A. Omodaka, N. Takeshima, and H. Fujita, "Fabrication and operation of polyimide bimorph actuators for a ciliary motion system," *Journal of Microelectromechanical Systems*, vol.2, no.4, pp.146-50, Dec. 1993.
- [4] H. Ballan and M. Declereq, *High voltage devices and circuits in standard cmos technologies*, Kluwer Academic Publishers, 1999.
- [5] G.H. Ballantyne, "Robotic surgery, telerobotic surgery, telepresence, and telementoring," *Surgical Endoscopy*, vol.6, no.10, pp.1389-1402, 2002.
- [6] C. Bellew, *An SOI process for integrated solar power, circuitry and actuators for autonomous MEMS*, Doctoral Dissertation, UC Berkeley, June 2002.
- [7] T.J. Brosnihan, J.M. Bustillo, A.P. Pisano, and R.T. Howe, "Embedded interconnect and electrical isolation for high-aspect-ratio SOI inertial instruments," 1997 International Conference on Solid-State Sensors and Actuators, Chicago, IL, USA, pp.637-40, June 1997.
- [8] M. Calin, N. Chaillet, J. Agnus, A. Bourjault, A. Bertsch, and S. Zissi, L. Thiery, (Edited by: G. Morel and F.B. Vernadat), "Shape memory alloy compliant microrobots," Proceedings volume from the 9th Information Control in Manufacturing Symposium, Nancy-Metz, France, vol.1, pp.241-8, June 1998.
- [9] G. Caprari, <http://www.k-team.com/robots/kalice/index.html>, K-TEAM SA, accessed May 2002.
- [10] P. Dario *et al.*, "Review microactuators for microrobots: a critical survey," *Journal Micromech. and Microeng.*, 2, pp.141-157, 1992.
- [11] L. Doherty, B.A. Warneke, B.E. Boser, and K.S.J. Pister, "Energy and performance considerations for smart dust," *International Journal of Parallel and Distributed Systems and Networks*, vol.4, no.3, pp.121-133, 2001.
- [12] T. Ebefors, J. U. Mattsson, E. Kalvesten, and G. Stemme, "A walking silicon micro-robot," *Proc. of the Tenth International Conference on Sensors and Actuators (Transducers '99)*, Sendai, Japan, pp.1202-1205, June 7-10, 1999.
- [13] R.S. Fearing, "Powering 3 dimensional microrobots: power density limitations," *Tutorial on Micro Mechatronics and Micro Robotics*, ICRA, 1998.
- [14] R.S. Fearing, "Survey of sticking effects for micro-parts," *IEEE Int. Conf. Robotics and Intelligent Systems IROS '95*, Pittsburgh, PA, 7-9 August 1995.
- [15] R. Feynman, "There's plenty of room at the bottom," talk given at the 1959 Meeting of the American Physical Society reprinted in the *Journal of Microelectromechanical Systems*, vol.1, no.1, pp. 60-66, March 1992.
- [16] A.M. Flynn, R.A. Brooks, and L.S. Tavrow, "Twilight zones and cornerstones: A gnat robot double feature," MIT Artificial Intelligence Lab Internal Memo, <ftp://publications.ai.mit.edu/ai-publications/pdf/AIM-1126.pdf>, July 1989.
- [17] J.E. Franca, Y. Tsividis, *Design of Analog-Digital VLSI Circuits for Telecommunications and Signal Processing*, Prentice Hall Inc., Englewood, , p.77-8, New Jersey, 1994.
- [18] T. Fukuda, A. Kawamoto, F. Arai, and H. Matsuura, "Steering mechanism and swimming experiment of micro mobile robot in water," in *Proc. IEEE Workshop on Micro Electro Mechanical Systems (MEMS '95)*, Amsterdam, The Netherlands, pp. 300-305, Jan. 29-Feb. 2, 1995.
- [19] M. Gebhard and W. Benecke, "Microtechnologies for microscaled robots and components," *Proceedings 1995 INRIA/IEEE Symposium on Emerging Technologies and Factory Automation. ETFA'95*, vol.3, Paris, France, pp.9-20, Oct. 1995.
- [20] A. Goetzberger and C. Hebling, "Photovoltaic materials, past, present, future," *Solar Energy Materials & Solar Cells*, 62, p. 1-19, 2000.
- [21] M.A. Green, *Solar Cells: Operating Principles, Technology, and System Applications*, Prentice-

- Hall, 1982.
- [22] Guinness World Records, <http://www.guinnessworldrecords.com>, accessed May 2002.
- [23] C. Hebling, S.W. Glunz, C. Schetter, J. Knoblock, and A. Rauber, "Silicon thin-film solar cells on insulating intermediate layers," *Solar Energy Materials and Solar Cells*, 48, pp.335-342, 1997.
- [24] S. Hollar, A. Flynn, S. Bergbreiter, and K.S.J. Pister, "Robot leg motion in a planarized SOI/2 poly process," Hilton Head 2002, June 2-6, 2002.
- [25] C. Hu and R.M. White, *Solar Cells From Basic to Advanced Systems*, McGraw-Hill Book Company, 1983.
- [26] L. Hui, A. Lal, J. Blanchard, D. Henderson, "Self-reciprocating radioisotope-powered cantilever," *Journal of Applied Physics*, vol.92, no.2, pp.1122-7, 15 July 2002.
- [27] Intuitive Surgical, <http://www.intuitivesurgical.com/>, accessed March 2003.
- [28] R.C. Jaeger, *Introduction to Microelectronic Fabrication: Volume 5 of Modular Series on Solid*, Prentice Hall, 2 ed., 17 Oct. 2001.
- [29] C.G. Keller and R.T. Howe, "HEXSIL tweezers for teleoperated micro-assembly," *Proceedings of the Tenth Annual Workshop of Micro Electro Mechanical Systems*, Nagoya, Japan, pp. 72-77, Jan. 26-30, 1997.
- [30] C.G. Keller, <http://www.memspi.com>, MEMS Precision Instruments, accessed Feb. 2003.
- [31] P.E. Kladitis, V.M. Bright, "Prototype microrobots for micro-positioning and micro-unmanned vehicles", *Sensors and Actuators A: Physical*, 80, pp.132-7, 2000.
- [32] P.B. Koeneman, I.J. Busch-Vishniac, and K.L. Wood, "Feasibility of micro power supplies for MEMS," *Journal of Microelectromechanical Systems*, vol.6, no.4, Dec. 1997.
- [33] M. Last and K.S.J. Pister, "2-DOF Actuated Micromirror Designed for Large DC Deflection," *MOEMS '99*, Mainz, Germany, Aug.29-Sept.1, 1999.
- [34] J.B. Lee, Z. Chen, M.G. Allen, A. Rohatgi, R. Arya, "A miniaturized high-voltage solar cell array as an electrostatic MEMS power supply," *Journal of Microelectromechanical Systems*, vol.4, no.3, pp.102-8, Sept. 1995.
- [35] B. Leibowitz, B. E. Boser, and K. S. J. Pister, "CMOS 'smart pixel' for free-space optical communication," *Proceedings of the SPIE - The International Society for Optical Engineering*, vol.4306A (Electronic Imaging '01), San Jose, CA, 21-26 January 2001.
- [36] N. Miki and I. Shimoyama, "Dynamics of a microflight mechanism with magnetic rotational wings in an alternating magnetic field," *Journal of Microelectromechanical Systems*, vol.11, no.5, pp.584-91, Oct. 2002.
- [37] J. Ohsawa, M. Kawasaki, T. Tanaka, N. Tsuchida, S. Hayakawa, M. Yshida, "A GaAs micro solar cell with output voltage over 20 V," *Japanese Journal of Applied Physics*, vol.38, pp.6947-51, 1999.
- [38] Larry D. Partain, *Solar Cells and Their Applications*, John Wiley & Sons, Inc., 1995.
- [39] K.S.J. Pister, M.W. Judy, S.R. Burgett, and R.S. Fearing, "Microfabricated hinges," *Sensors and Actuators A (Physical)*, vol.A33, no.3, pp.249-56, June 1992.
- [40] R.D. Quinn, G.M. Nelson, R.J. Bachmann, D.A. Kingsley, J. Offi, and R.E. Ritzmann, "Insect designs for improved robot mobility," *Proc. 4th Int. Conf. On Climbing and Walking Robots*, Berns and Dillmann eds., Prof. Eng. Pub., pp.69-76, 2001.
- [41] M. H. Raibert. *Legged Robots That Balance*, Cambridge: MIT Press, 1986.
- [42] S. Roundy, P.K. Wright, J. Rabaey, "A study of low level vibrations as a power source for wireless sensor nodes," To be published in *Computer Communications*, 2003.
- [43] U. Srinivasan, D. Liepmann, and R.T. Howe, "Microstructure to substrate self-assembly using capillary forces," *Journal of Microelectromechanical Systems*, vol.10, no.1, pp.17-24, March 2001.
- [44] A. Sullivan, *Iolanthe, or the Peer and the Peri*, Hal Leonard Publishing Corporation, Nov. 1996.
- [45] K. Suzuki, I. Shimoyama, H. Miura, and Y. Ezura, "Creation of an insect-based microrobot with an external skeleton and elastic joints," in *Proc. IEEE Workshop on Micro Electro Mechanical Systems (MEMS '92)*, Travemunde, Germany, pp.190-195, 4-7 Feb. 1992.
- [46] A. Teshigahara, M. Watanabe, N. Kawahara, Y. Ohhtsuka and T. Hattori, "Performance of a 7-mm microfabricated car," *Journal of Microelectromechanical Systems*, vol.4, pp.76-80, 1995.
- [47] Varta Microbattery, GmbH, <http://microbatteries.varta.com/en/index.html>, accessed March 2003.

- [48] B. Warneke, M. Scott, B. Leibowitz, L. Zhou, C. Bellew, A. Chediak, J. Kah, B. Boser, and K.S.J. Pister, "Autonomous 16 mm³ solar-powered node for distributed wireless sensor networks", IEEE International Conference on Sensors, 12-14 June 2002.
- [49] B. Warneke, personal communication, June 2001.
- [50] S. Wolf and R.N Tauber, *Silicon Processing for the VLSI Era Volume 1 - Process Technology*, Lattice Press Sunset Beach, CA, 1986.
- [51] D. Wood, J.S. Burdess, and A.J. Harris, "Actuators and their mechanisms in microengineering," Engineering Science and Education Journal, vol.7, no.1, pp.19-27, Feb. 1998.
- [52] J. Yan, R.J. Wood, S. Avadhanula, M. Sitti, R.S. Fearing, "Development of PZT and PZN-PT based unimorph actuators for micromechanical flapping mechanisms," IEEE Int. Conf. Robotics and Automation, Seoul Korea, pp.3839-46, 21-26 May 2001.
- [53] A.A. Yasseen, J. D. Cawley, M. Mehregany, "Thick glass film technology for polysilicon surface micromachining," Journal of Microelectromechanical Systems, vol.8, no.2 , pp. 172 -179, June 1999.
- [54] T. Yasuda, I Shimoyama, and H. Miura, "Microrobot locomotion in a mechanical vibration field," Advanced Robotics, 9, 2, 1995.
- [55] R. Yeh, E.J.J. Kruglick, and K.S.J. Pister, "Surface-micromachined components for articulated microrobots," Journal of Microelectromechanical Systems, vol.5, no.1, pp.10-17, March 1996.
- [56] R. Yeh, S. Hollar, and K.S.J. Pister, "Design of low-power silicon articulated microrobots," Journal of Micromechatronics, vol.1, no.3, pp.191-203, 2001.
- [57] R. Yeh, S. Hollar, and K.S.J Pister, "Single mask, large force, and large displacement electrostatic linear inchworm motors," Journal of Microelectromechanical Systems, vol.11, no.4, pp.330-6, August 2002.
- [58] R. Yeh, *Articulated Mechanisms and Electrostatic Actuators for Autonomous Microrobots*, Doctoral Dissertation, UC Berkeley, June 2001.
- [59] L. Zhou, K. S. J. Pister, J. M. Kahn, "Assembled corner-cube retroreflector quadruplet," Proc. 2002 IEEE MEMS Conf., Las Vegas, Nevada, pp.556-9, 20-24 Jan. 2002.